Identifying Dynamic Nonlinearities due to Damage Precursors in Flexible Structures

By

Thiago C. Dragman
S1849697

UNIVERSITY OF TWENTE.

Dynamics Based Maintenance (DBM) Research Group
Faculty of Engineering Technology
University of Twente

A thesis submitted to the University of Twente in accordance with the requirements of the degree of Master of Science in Mechanical Engineering.

April 2019

Thesis supervisor:
Ed Habtour, Ph.D., P.E.

Examination committee:
Prof. dr. ir. Tiedo Tinga
Dr. ir. Richard Loendersloot
Dr. ir. Jurnan Schilder

Abstract

Vibration-based Structural Health Monitoring (SHM) techniques are effective for detecting fatigue damage in structures by assessing changes in the dynamic behavior. When it comes to structures that exhibit significant nonlinear dynamic behavior, general SHM methods are not able to adequately describe the occurring dynamical phenomena. Furthermore, previous studies have shown that for flexible structures, changes in nonlinear system parameters were more sensitive to damage precursors than changes in linear system parameters. These facts suggest that a proper understanding of nonlinear dynamic properties is of high importance within SHM.

This work identifies changes in the nonlinear dynamic behavior of cantilever beams over various stages of fatigue cycles by employing an experimental and analytical approach. The main aim was to investigate to what extent the monitoring of nonlinear dynamic system parameters can result in improved detection of damage precursors. A multidisciplinary literature review was conducted to gain broad insights into the latest advancements in SHM. Experiments were carried out to characterize linear and nonlinear system parameters of Al7075-T6 cantilever beams. The dynamic characterizations included sine-sweep excitation (forced) and free vibration (transient). For each characterization, tests for the nonlinear and linear region were conducted. A signal processing approach was applied to convert the experimental data into useful results, such as backbone curves and damping skeletons. By employing fatigue testing, the results were correlated to different levels of component health. An analytical approach was carried out to develop the equation of motion (EoM) and to model the dynamic response. Techniques applied to derive the EoM include Nonlinear Euler-Bernouilli and the Assumed Modes method. The dynamic response was modeled using the Harmonic Balance method, the Method of Averaging and numerical methods (Runge-Kutta). The research uncovers interesting changes in various nonlinear properties due to the increasing presence of damage, and shows that the inclusion of nonlinear analysis can lead to improved techniques in the field of SHM.

Acknowledgements

This thesis was written as the concluding part of the Masters Degree in Mechanical Engineering at the University of Twente within the Dynamics Based Maintenance (DBM) research chair. This work would not have been possible without the help of several magnificent human beings. Words cannot express how thankful I am to these people, but that is exactly what I will attempt to do in the following.

Ed Habtour was my main supervisor. This guy is something else. The amount of things I have learned under his wing is incredible. I am extremely grateful for his guidance and time. I thank Tiedo Tinga for introducing me to the topic and making this thesis possible at the DBM chair. He also offered very valuable advice, feedback and support. Next up, I would like to show some appreciation to the members of my examination committee. I wish to thank Richard Loendersloot, whose course in Structural Health Monitoring peaked my interest and motivated me to pursue a related topic for my thesis. I thank Jurnan Schilder, who I view as a very inspiring person and a genius in Dynamics. I very much look up to all these people, and if I ever reach their intellectual level, I would say life well-lived.

I express my gratitude to Thijs Masmeijer for his significant contributions to the experimental approach and to several analyses. I am also grateful to Laura Cordova and Dennis Lek who collaborated during the starting phase of the project. I thank Axel Lok for his assistance in the experimental setup. I also greatly appreciate all the tips and feedback from the DBM group during the monthly meetings.

Most importantly, I would like to thank my parents, Ingrid Brohim and Robby Dragman, for their unconditional love and support. Without them, I simply would not exist and studying abroad would not be possible. Last but not least, I thank all my friends and fellow students for their support and for all the good times during my studies in Enschede.

Enschede, April 2019
Thiago C. Dragman

Table of Contents

Acronyms

AFM Atomic Force Microscopy

BPA Bending Point Amplitude

BPS Bending Point Slope

DP Damage Precursor

EBM Energy Balance Method

EBSD Electron Backscatter Diffraction

EoM Equation of Motion

FEM Finite Element Method

FFT Fast Fourier Transform

FRF Frequency Response Function

HBM Harmonic Balance Method

IHB Incremental Harmonic Balance

MMS Method of Multiple Scales

MoA Method of Averaging

NFT Normal Form Theory

NNM Nonlinear Normal Modes

ODE Ordinary Differential Equation

PDE Partial Differential Equation

SDF Symbolic Dynamic Filtering

SHM Structural Health Monitoring

SI System Identification

XRD X-Ray Diffraction

List of Symbols

Roman Symbols

$\hat{F}$	Force	N
c_1	Viscous damping coefficient	Ns/m
c_2	Quadratic damping coefficient	Ns^2/m^2
E	Young's modulus	N/m^2
I	Second moment of inertia	m^4
I_r	Rotational inertia	$kg \cdot m^2$
k_1	Linear stiffness coefficient	N/m
k_3	Cubic stiffness coefficient	N/m^3
L	Beam length	m
m_1	Linear inertial coefficient	kg
m_3	Nonlinear inertial coefficient	kg
m_s	Distributed mass	kg/m
t	Time	s
v	Vertical tip displacement	m
Y	Base displacement	m

Greek Symbols

α	Displacement Amplitude	m
ΔF_{jump}	Difference between jump-down and jump-up frequency	Hz
Ω	Normalized Frequency (Normalized by natural frequency of the pristine structure)	
ω	Frequency (Angular)	rad/s
ω_n	Natural frequency (Angular)	rad/s
ρ	Bending curvature	
ϱ	Volumetric density	kg/m^3
ζ_1	Viscous damping ratio	
ζ_2	Quadratic damping ratio	

CHAPTER 1

INTRODUCTION

The opening chapter begins by discussing the motivation behind the research performed for this Master's thesis in section 1.1. This is followed by a literature review in section 1.2, which provides context and background for the current work, and current scientific gaps. Thereafter, in section 1.3, the research goals, objectives, and research questions are stated. Finally, in section 1.4 the research methodology is detailed.

1.1 Motivation

In aerospace applications, effective Structural Health Monitoring (SHM) systems are essential for ensuring the reliability and safety of aircraft. The main goal of SHM is to detect structural anomalies before reaching a critical damage level [1]. SHM is important for identifying the severity of damage due to various failure mechanisms, such as shock, vibration fatigue, or thermal stresses [2] [3]. Because SHM has significant potential for life-safety and economic benefits, there has been a rapid increase in multidisciplinary research efforts, and technological improvements for advancements concerning the reliability and sensitivity of SHM [4]. One of the earlier techniques applied in SHM is modal analysis, which is established as a fundamental strategy in identifying fatigue damage within SHM. However, modal analysis is a linear theory, and cannot be applied to significantly nonlinear systems [5–7]. In reality, numerous engineering structures do not comply with the assumption of linear behavior and these structures exhibit various nonlinear behaviors [7–9]. Engineers are often confronted with nonlinearities in: the aerospace industry [8, 10], the military [11], robotics [12, 13] and MEMS devices [12, 14, 15].

The effect of nonlinearities on modal analysis is quite detrimental, because all the invariant system parameters, which are generally taken for granted for a linear system, including resonant frequencies, damping ratios, frequency response functions (FRFs) and modeshapes, now become dependent on the magnitude of applied excitation [16]. When nonlinear effects in structures are no longer negligible, then linear modal analysis cannot accurately describe the occurring dynamical phenomena [17, 18]. The study of nonlinearities in the monitoring of structures is highly essential for the development of SHM techniques, since these effects can be incorrectly viewed as structural changes [19]. According to Worden et al. [20] damage detection can be notably improved by incorporating nonlinear effects during the extraction of damage features. Various techniques have been proposed to deal with nonlinear systems, but a generally accepted technique remains undefined [19, 21].

Flexible beam structures are important elements, with widespread usage in airplane wings, helicopter

blades, robot arms, MEMS devices and flexible satellites [13]. Usually beam elements are used as simplified models for more complex structures or as precision mechanisms. If the amplitude of vibration increases, beam structures are also subjected to significant nonlinear vibrations [13, 22]. The nonlinear mechanics of these structures are a popular research interest [22–24].

A promising concept within fatigue damage identification is the detection of Damage Precursor (DP)s, which are defined as observable early degradation in the material properties of a structure, that precede the initiation of fatigue cracks [25]. To this end, researchers [11, 25, 26] have conducted various microstructural experiments to investigate fatigue DPs in metal cantilever beams, including: nanoindentation, Electron Backscatter Diffraction (EBSD), X-Ray Diffraction (XRD) and Atomic Force Microscopy (AFM). The researchers were thereby able to observe changes in the material properties due to increases in fatigue cycles, such as elastic modulus, residual stresses, crystal orientation, and grain size. All these changes were detectable before large scale damage were present and can be considered as evidence of potential DPs. These microstructural changes, as expected, lead to changes in the macro-structural properties. Studies have shown that nonlinear system parameters for steel cantilever beams exposed to transverse [26] and [27] vibration fatigue, specifically the nonlinear stiffness terms in the equation of motion (EoM), was found to be more sensitive to fatigue damage precursors than linear stiffness terms. Haynes et al. [11] reported similar nonlinear structural dynamic results for aluminum cantilever beams exposed to random base excitation. In this study forward and backward sine-sweeps were applied frequently to monitor the FRF response, which appeared to increase with damage accumulation. The performed research related to DPs, suggests that proper understanding of nonlinear dynamic properties is of high importance within SHM. There is significant room for improvement in our understanding of how these parameters change over various stages of component health for different materials.

This research work aims to investigate changes in the nonlinear dynamic response of flexible beams over various stages of fatigue cycles. The fundamental goal is provide experimental and theoretical tools to improve detection of DPs based on changes in nonlinear parameters in the equation of motion. The tools are vibration-based detection, which include sine-sweep, step-sine, and free-vibration. Trends can be extracted from each technique to detect and assess the severity of DPs. The experimental tools were applied for flexible aluminum cantilever beams fatigued in a similar manor to [11, 26]. In this study, nonlinear free-vibration appears to be the most time efficient with reasonable accuracy compared to traditional methods. To this end, a multidisciplinary literature review was necessary to gain broad insights into the latest advancements within SHM. It is important to point out that due to the substantial breadth of SHM, it is difficult to survey all major advancements generated in the last ten years. Thus, the majority of the survey includes studies focused on nonlinear phenomena.

1.2 Literature Review

Due to the substantial breadth of SHM, the primarily objective of literature review is to identify relevant research related to the analysis of nonlinear dynamical systems, nonlinear structural dynamics, damage detection methods, and damage precursors. Hereby the focus is primarily on, but not restricted to, flexible structures. Several other topics deemed potentially useful for the research are also included.

The literature review is divided into the following categories:

1. System Identification and Data-Driven Methods (subsection 1.2.1)
2. Physics-Based Methods (subsection 1.2.2)
3. Hybrid Methods (subsection 1.2.3)
4. Damage Precursors (subsection 1.2.4)
5. Scientific Gaps and Paths for Improvement (subsection 1.2.5)

The review is not intended as a comprehensive review of all existing methods related to the mentioned fields, but rather to provide numerous illustrations of approaches common in current literature. Figure 1.1 depicts a visual representation of the review structure, which also emphasizes the connections among the sections of the review and and aims to enhance the reader's understanding. This figure is further explained in subsection 1.2.5. The review is also helpful in the selection of the most appropriate techniques in order to accomplish the research goal.

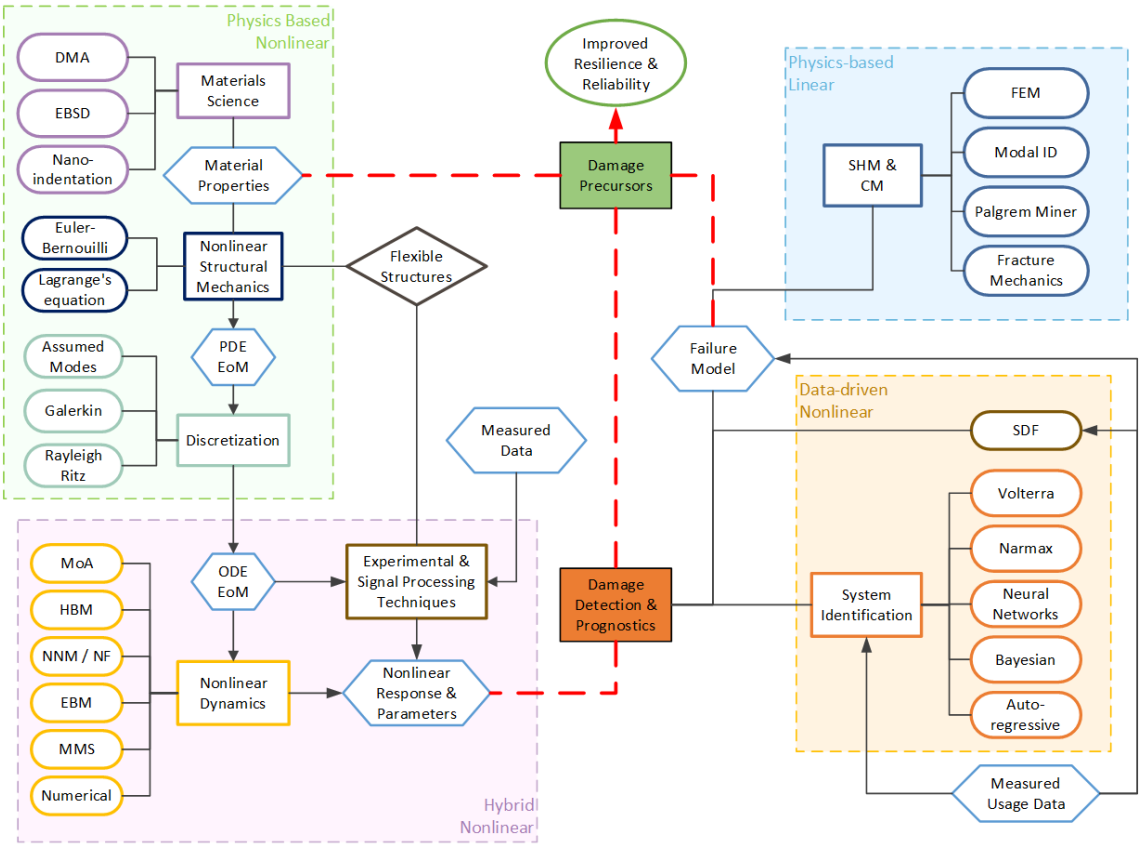

Figure 1.1: Visual representation of methods used in the literature and areas for impovement.

1.2.1 System Identification and Data-Driven Methods

The field of System Identification (SI) focuses on creating models of dynamic systems from measured input and output data [28]. The field is very broad with various techniques applicable to different type of systems, e.g., linear, nonlinear, hybrid, nonparametric, etc. [28]. Within SI three types of

model classifications are defined: white-box, black-box, and grey-box models [29]. White-box models (bottom-up approach) are purely theoretical and based on first principles. Such models are synonymous with the physics-based approach within SHM and Predictive Maintenance (PdM). In many cases, white-box models are complicated to obtain due to the inherently complex nature of many systems. Therefore, the model types that are dominant in the domain of SI are black-box and grey-box models. In black-box modeling (top-down approach) no model form is assumed and it can be considered purely data-driven and statistical. It can be viewed only in terms of the input and output data without actual knowledge of the internal workings of the system. The third type is grey-box modeling, which combines a model structure with data-driven techniques to complete the model. The model structure is thereby assumed beforehand, and subsequently, the model parameters are estimated [30]. Data-driven techniques can often be combined with machine learning to increase the accuracy and effectiveness of anomaly detection. Models broadly used within nonlinear system identification include: Volterra series [19, 31, 32], NARMAX [31–33] and artificial neural networks [19, 33].

Cheng et al. [33], who reviewed Volterra-Series-based nonlinear system modeling and its engineering applications, stated that although many researchers have made progress in the past decades, the method still presents many challenges. Brewick and Masri [21] explored a variety of data-driven identification techniques for complex nonlinear dynamic systems. The Volterra/Wiener neural network (VWNN) was hereby compared against several existing methods, including polynomial-based nonlinear estimators and artificial neural network systems. The authors found that VWNN provided superior accuracy in its estimates. The application of SI techniques for damage detection has also been explored by several researchers. Shiki and Silva [19] proposed damage indicators based on Volterra series by considering nonlinear contributions of the response of an aluminum beam test rig. The identified metric was sensitive to structural changes even under the nonlinear range of motion. A Volterra model was also proposed by Chatterjee [34] for a cantilever beam with a breathing crack. The model was based on the harmonic probing method and the authors managed to correlate variations in the system response to the opening of the crack. A new SHM framework was presented by Rabiei et al. [35] based on the evolution of DPs using dynamic Bayesian networks. The method was suitable when a conventional damage indicator, such as a crack, is difficult to measure. The method was successfully applied to estimate damage and predict crack initiation in 7075-T6 aluminum samples subject to fatigue.

A data-driven technique with potential in damage identification is Symbolic Dynamic Filtering (SDF). Several researchers have studied the theory of SDF and its various applications for anomaly detection and pattern recognition. According to Gupta and Ray [36], the core concept of SDF is based on the phase-space partitioning of a dynamical system to yield a symbolic alphabet and to obtain symbol sequences from time series data. The time series data of sensors are processed and converted from real numbers into discrete symbols. This process results in a so-called symbolic dynamical system that can aid to understand the dynamical behavior of the original system. The key idea of SDF is then to quantify deviations of the current pattern from the baseline pattern, which can indicate the occurrence of anomalies. Rao et al. [37] presented a review of SDF and evaluated its performance for anomaly detection compared to other types of pattern recognition techniques, such as Bayesian Filters and Artificial Neural Networks. They concluded that SDF is well suited for health monitoring applications. Patankar et al. [38] developed a data-driven signal processing method using SDF to identify anomalies

and monitor failure precursors. They stated the technique to be superior to conventional techniques such as neural networks and principal component analysis.

The covered topics are only a fraction of all the existing SI methods. If the reader is interested in more, a literature review of SI articles related to SHM was conducted by Sirca and Adeli [39], which also includes approaches such as chaos theory and biologically-inspired approaches. The authors [39] also stated that SI of real-life structures with nonlinear behavior subjected to unknown dynamic loading is challenging and they believe a multi-paradigm approach might be the best strategy for this issue.

Based on the research related to data-driven SI and damage identification techniques, it can be stated that these methods are promising for damage detection in nonlinear dynamical systems, however, data-driven approaches go paired with a lack of thorough understanding of the system physics.

1.2.2 Physics-Based Methods

Physics-based methods are essentially bottom-up approaches. These methods require a proper understanding of the system physics and aim to provide accurate representations of reality. The main advantage of these methods is that they can be linked to the physical properties of a system such as changes in material properties. Of interest in this section are the fields of nonlinear dynamics, and nonlinear solid mechanics. According to Lacarbonara [40], there is a need for a multidisciplinary approach to the analysis of structural systems. Nonlinear dynamics has overlaps with the fields of analytical dynamics, and applied mathematics and physics. The current section outlines various techniques related to nonlinear dynamic systems, nonlinear structural mechanics, and also treats general physics-based damage identification methods.

The Method of Multiple Scales (MMS), which is a perturbation method, is widely used to provide approximate solutions for systems with weakly nonlinear functions [41]. Several researchers have used MMS to perform nonlinear system analyses on flexible beam structures. Usually, to perform the analysis, the governing EoM is first derived using the Euler-Bernouilli beam theory and the extended Hamilton's principle. Hereafter the Galerkin approach is applied to discretize the equation and MMS is then used for solving the nonlinear equation to obtain the response. This procedure was applied by Yan et al. [42], and Singh et al. [15], who investigated the influence of nonuniform cantilever beams on the nonlinear response. MMS was also used by Chakrapani and Barnard [43], who determined nonlinear system parameters of aluminum and Pyrex beams.

Another technique applicable for identifying nonlinearities is Nonlinear Normal Modes (NNM). The method is useful for interpreting a wide range of nonlinear dynamical phenomena, yet it also has a clear relation to the common linear normal mode, which structural engineers are familiar with [44] [45]. Based on NNM, Peters et al. [46] proposed a methodology that was demonstrated using a cantilever beam with a spring at its free end. By employing NNM, Lacarbonara et al. [47] proposed a damage identification strategy, where they applied numerical methods to simulate damage on a flexible beam. A schematic of their method is shown in Figure 1.2. They found that the nonlinear coefficients describing the behavior of the beam were more sensitive to damage than the linear frequencies. This supports the notion that the experimental identification of the nonlinear coefficients can be a viable strategy for damage detection. NNM, however, is argued to be inaccurate when significant damping is present [48].

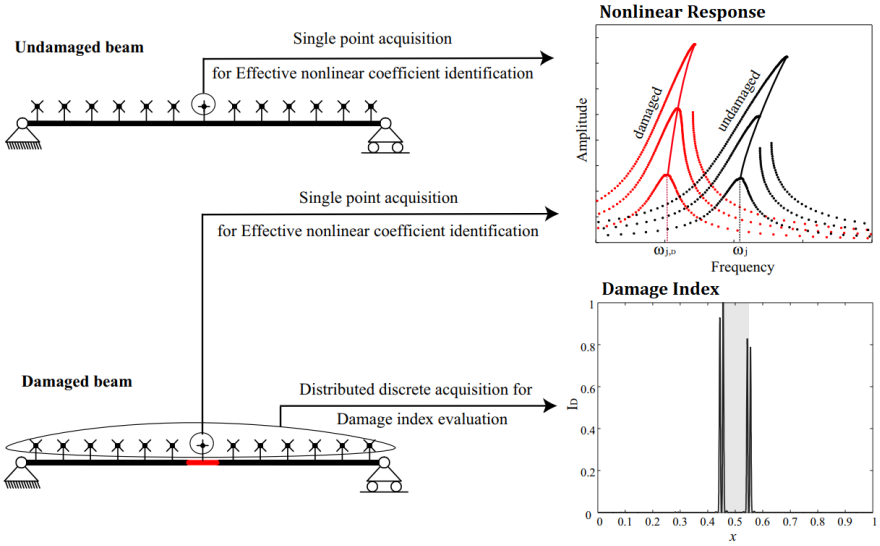

Figure 1.2: Proposed damage identification strategy by Lacarbonara et al. [47].

A related approach is to search for a simplifying transformation of the nonlinear EoM using Normal Form Theory (NFT) [49]. The theory has been used to treat various dynamics problems. In 2011, Neild and Wagg [49] demonstrated that Normal Form analysis can be carried out on nonlinear vibration problems. Four years later, the use of NFT was proposed by Neild et al. [48] as a superior method compared to NNM. The authors showed how the method was able to predict nonlinear mode shapes, and bifurcations accurately. Cammarano et al. [50] presented a method that exploited NFT to identify the nonlinear system coefficients. NFT was also successfully applied by Shaw et al. [51], combined with experiments on cantilever beams. They also showed how a local nonlinearity can introduce rich dynamics into a structure that would otherwise be a typical case of linear modal dynamics.

Other methods were applied in recent research to model nonlinear behavior of flexible beam structures. Belinchon et al. [52] obtained an approximate solution of the strongly nonlinear differential equation describing the free vibrations of a cantilever beam by using a method based on the Laplace transform and the convolution theorem. Wang et al. [53] proposed a strategy which was successful for characterizing beam structures with a localised nonlinearity using a Finite Element Method (FEM) model and experimental response data. Jamal-Omidi et al. [54] examined the nonlinear behavior of a cantilever beam under free vibration analytically and experimentally. The PDE EoM was first derived using Crespo da Silva and Glynn beam theory. The EoM was then discretized using Gallerkin method. Subsequently, an exact solution was developed, which showed good agreement with the experiments.

Many researchers have studied the modeling and identification of fatigue damage by considering changes in the dynamic response of structures. Ostachowicz and Krawczuk [55] investigated the effect of cracks on the natural frequencies in a cantilever beam by employing fracture mechanics and a numerical method. Mia et al. [56] extracted the natural frequencies, and mode shapes of the transverse vibration for a cracked cantilever beam using FEM modeling to perform the analyses. Changes in the natural frequency were correlated to crack location, depth and size. Tinga and Loendersloot [57] conducted a comparison study of structural health monitoring (SHM), condition based maintenance (CBM), and prognostics and health management (PHM), and proposed a methodology for integrating them. Various

damage identification techniques were thereby discussed, including the effective Modal Strain Energy – Damage Identifier (MSE-DI) algorithm [58], which is based on the comparison between the curvatures of the mode shapes of pristine and damaged structures. To investigate fatigue damage, Kos et al. [59] performed sweep-sine and random excitation experiments, and the Palmgren-Miner rule was applied to calculate the fatigue life. Mrsnik et al. [60] used modal decomposition to link the fatigue damage with various dynamic parameters.

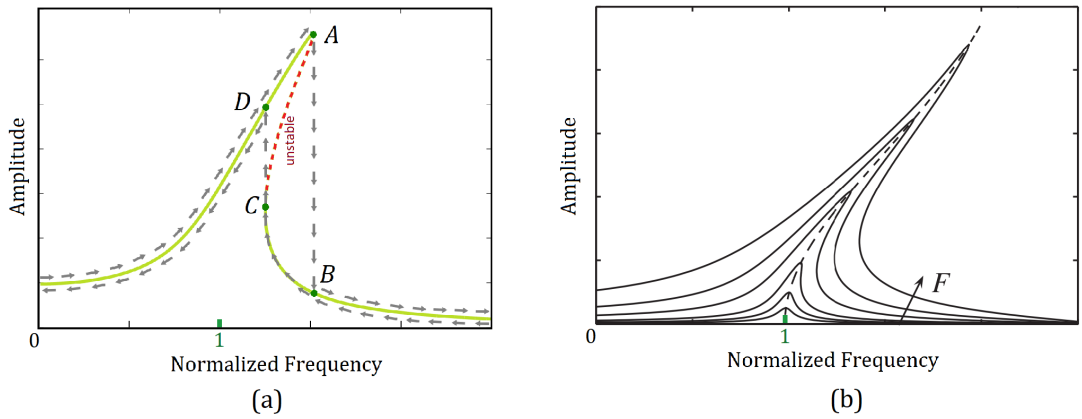

Figure 1.3: Clarification of nonlinear FRFs, jump phenomena and backbone curves [61] [46].

1.2.3 Hybrid Methods

The hybrid methods draw on physics-based approaches, but combine system identification and signal processing as a means for efficient analysis of nonlinear dynamic systems. Although not completely belonging to bottom-up approaches, the techniques have a solid foundation based on the system's physics. A common ground within these methods is to conduct experiments and to apply processing techniques to obtain useful metrics of nonlinear systems.

The Harmonic Balance Method (HBM) is a frequency domain method used to calculate the steady-state response of nonlinear systems. This method can only be applied once the system EoM is known, and this is usually assumed beforehand. According to Hosen and Chowdhury [62], who applied HBM to approximate periods of a strongly nonlinear Duffing oscillator, the procedure is simple and takes little computational effort, while also showing a good agreement compared with exact methods. A strategy based on HBM was employed by Liao [63] to study the nonlinear oscillations of an airfoil. HBM was also used by Motallebi and Sazesh [24] to investigate jump (Figure 1.3a) and bifurcation phenomena for a geometrical nonlinear cantilever beam. Considering HBM, Lu et al. [64] introduced jump amplitudes as a supplement condition in the estimation of various nonlinearities. Their method appeared to be effective for systems exhibiting strong nonlinearities. Doughty et al. [65] applied HBM and MMS to identify nonlinear modal behavior of cantilever beams. The research showed that the performance of each method actually improved as the nonlinearities increased in magnitude. A comparison of NFT, HBM, and MMS was performed by Hill et al. [41], where all methods gave good accuracy at low response amplitudes, but NFT and HBM also give good accuracy as the response amplitude increases.

Elliot et al. [66] investigated the accuracy of HBM, MMS and NFT for a MDOF oscillators. All three methods produced accurate results, with errors less than 0.2% for NFT and HBM, and 1% for MMS.

A related technique for approximating nonlinear system behavior is the Incremental Harmonic Balance (IHB) method, which is a combination of the Incremental method (Newton-Raphson procedure) and the HBM method. IHB was applied by Dou and Jensen [67], where it showed good agreement with a FEM method for modeling geometrically nonlinear beam structures. By applying IHB, Liu et al. [68] investigated the aeroelastic response of an airfoil with a hysteresis nonlinearity. Various bifurcations were detected as the flow speed was varied.

The Energy Balance Method (EBM) is a technique for solving strong nonlinear oscillators, which has been stated to provide a more accurate result than HBM [69]. Using EBM, Akbarzade et al. [13] studied the frequency-amplitude relationship for transversely vibrating beams, whereby it led to excellent results. Hosen et al. [70] proposed an analytical technique based on EBM to obtain approximate periodic solutions for three types of highly nonlinear oscillators.

First introduced several centuries ago in celestial mechanics, the Method of Averaging (MoA) has had a profound influence in physics and engineering [71]. The technique can predict solutions of strongly nonlinear oscillators. Through employing MoA, Zaghari et al. [18] researched the nonlinear dynamic response of a cantilever beam under base excitation. Hereby the response amplitude was explained analytically for various system parameters and it was in agreement with numerical results. Kumar et al. [72] investigated the nonlinear behavior of a base-excited, flexible cantilever beam. Response parameters were analyzed through the use of MoA and experiments were performed to validate the analytically predicted behaviors. MoA was also used by Zhu [73] to study the dynamics of a 2DOF vibration system with nonlinear damping and nonlinear stiffness.

Several researchers have investigated nonlinear phenomena occurring during aircraft flights. According to Dowell [74], who reviewed recent advances in the field of nonlinear aeroelasticity, many physical mechanisms can lead to nonlinear aeroelastic response during flights. Fuellekrug and Goege [75] described an experimental strategy for nonlinear modal identification of nonlinear effects within complex aerospace structures. A method called Modal force appropriation was thereby used to identify the nonlinear restoring forces. Piraccini et al. [76] presented a novel approach for testing structural components to nonlinear vibrations. Instead of using common electromagnetic shakers they employed an air-jet excitation method, which drives the test specimens with a contactless pulsed air-jet force. The authors measured the nonlinear vibration response in aerospace composite blades. Through a signal processing approach, nonlinear FRFs, nonlinear damping ratios and backbone curves, were obtained.

The Backbone Curve is an invaluable tool capable of offering a better understanding of the nonlinear system behavior (as shown by the dashed line in Figure 1.3b). In backbone curves, the natural frequency is plotted as a function of the system response amplitude [10]. Backbone curves can be obtained by performing a series of sine-sweeps at different amplitudes or by processing the free decay signal. Several techniques exist for the extraction of backbone curves from free decay data, including the Hilbert transform, Wigner–Ville distribution and the Wavelet transform [77]. However, these methods can be sensitive to noise, which is detrimental to their estimation capabilities. Londono et al. [10] presented a technique for the extraction of backbone curves of damped nonlinear systems from resonance decay responses. This experimental approach, which is based on the Resonance Decay Method (RDM), was

proved well suited of structures exhibiting nonlinear behavior. Two years later, Londono et al. [78] presented a similar identification method for structures containing nonlinear stiffness, again using backbone curves. The results between the decay response and stepped sine seemed to agree well with each other. Another way of experimentally obtaining backbone curves, is Control-Based Continuation (CBC). This technique entails testing nonlinear dynamic systems in a controlled manner and thereby assessing the dynamic features. According to Renson et al. [77], who compared the use of CBC and RDM, the repeatability and results of both methods were excellent. Pickard [79] used backbone curves to assess changes in nonlinear response of composite plates over different stages of high-cycle fatigue. The backbones were obtained through sine-sweep experiments with various excitation amplitudes. The results showed not just the reductions in frequency, but also indicated variations in the gradient of the softening and stiffening regions of the response. His obtained results are shown in Figure 1.4. The author concluded that there is a clear potential of using changes in nonlinear behaviour as an indicator of damage development.

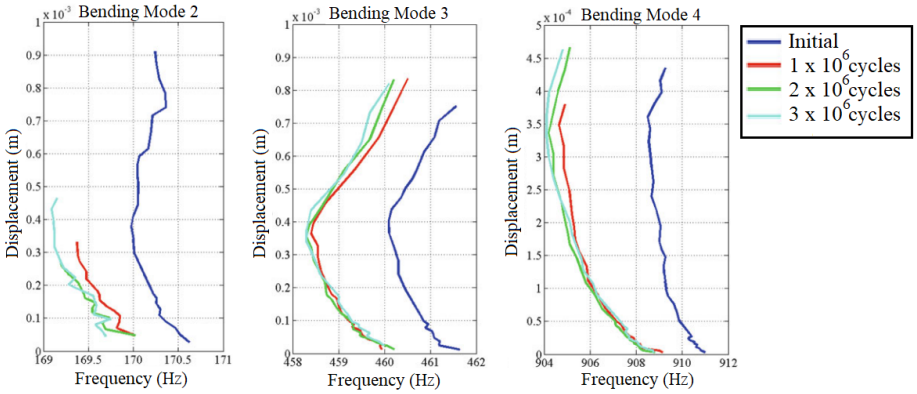

Figure 1.4: Backbone curves obtained by Pickard [79] for bending mode 2-4.

1.2.4 Damage Precursors (DPs)

As introduced in section 1.1, damage precursors are an interesting research area. Examples of measurable DPs to fatigue crack development include changes in the microstructure, electrical signal, acoustic response or mechanical response of a structure [27]. In addition to the findings stated in section 1.1, several DP-related studies are discussed in the following.

Vantadori et al. [80] proposed a methodology to assess the development of embryonic cracks in structures under high-cycle multiaxial random vibrations. Hereby the frequency-domain critical plane criterion was outlined and evaluated using experimental results of steel cantilever beams under nonlinear base vibration. Cole et al. [25] provided insight into fatigue DPs and provided a framework for connecting the materials evolution (micro-scale) to nonlinear structural dynamics (macro-scale) by considering microstructural transformations of steel cantilevers prior to conventional damage formation. By performing nanoindentation, they showed that the indentation modulus of the materials decreased by up to 50% in high-stress areas. Through employing Electron Backscatter Diffraction (EBSD) (Figure 1.5), X-Ray Diffraction (XRD) and Atomic Force Microscopy (AFM), the researchers were able to observe additional microstructural changes related to residual stresses, crystal orientation, and grain size. A

damage precursor indicator was proposed by Haynes et al. [11] based on the nonlinear dynamic behavior of aluminum cantilever beams. Macro- and micro-testing was performed. The observed changes in the material microstructure and dynamic response were detectable before the onset of large scale damage and can be considered as evidence of DPs. Habtour et al. [5] proposed an integrated materials-structures-dynamics approach to improve the overall structural state awareness. The main idea was to track changes in the energetics of the materials-structures-dynamics states and connect these traditionally detached fields to enable improved damage precursor detection within SHM. Various methods were discussed, including the restoring force surface method for the global states, and EBSD characterizations for the local material state, as shown in Figure 1.5.

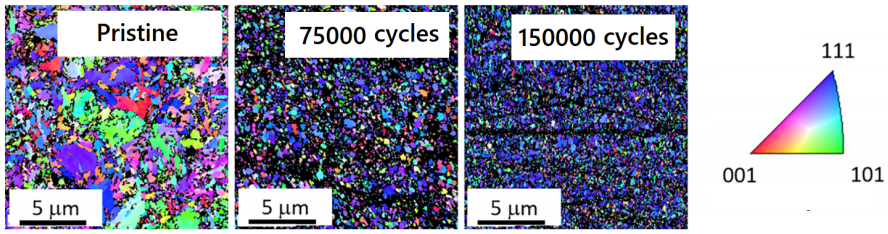

Figure 1.5: EBSD results for 1095 steel cantilevers exposed to nonlinear harmonic oscillation. The results show clear changes in grain size and grain orientation prior to crack initiation (Obtained from Habtour et al. [5]).

The findings related to damage precursors suggest that harnessing and exploiting damage precursor detection holds promise in improving the reliability and resilience of assets by assessing oncoming damage in a very early stage. There is much that still needs to be learned about fatigue DPs. Research into the microstructural evolution and resulting changes in the nonlinear dynamic responses of fatigue structures are expected to be highly advantageous for future SHM applications.

1.2.5 Scientific Gaps and Paths for Improvement

Referring back to Figure 1.1, possible paths for improvement are visualized by the red dashed lines. The interpreted gaps and improvement opportunities are detailed in the following.

Currently, there is still a lack in understanding of how DP-related microstructural properties change over usage cycles. It is unknown how these microstructural changes affect the global dynamic behavior compared to fatigue cracks. There is much room for improvement within this domain.

Additionally, most techniques in experimental nonlinear dynamics and signal processing assume an ODE EoM a priori. For flexible structures subject to fatigue loading, this assumption can be highly inaccurate and incorporation of nonlinear structural mechanics (solid mechanics) becomes necessary. This incorporation would also enable to establish the link to microstructural DP-related changes.

Much research has been performed for experimental techniques in identifying nonlinear dynamic behavior, but these techniques are not incorporated into current SHM methods. There has been minimal overlap between nonlinear dynamics and SHM. Most SHM methods appear to use linear methods to analyze structures, which are inaccurate for numerous systems that show nonlinear behaviour. There is still a lack of knowledge regarding how nonlinear parameters change over fatigue cycles compared to general (linear) parameters for different types of structures. It is possible that nonlinear dynamics can be exploited to improve current SHM techniques.

1.3 Research Goal, Objectives and Research Questions

The goal of this work is to investigate changes in nonlinear system properties of cantilever beams over various stages of component health. The focus is on changes in the global dynamic behavior, but with further research into the microstructural phenomena in mind, which could bridge the two areas in the future. Hence, nonlinear structural mechanics and nonlinear dynamics are the scope of this work (Figure 1.6). The research is geared towards finding improved precursors to damage (Figure 1.7a).

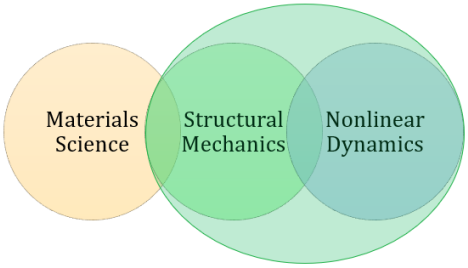

Figure 1.6: Scope of this work

To realize the aim of this work, the following objectives are defined:

- Develop an analytical method to model nonlinear dynamic behavior based on the system physics
- Develop an experimental and signal processing approach to characterize nonlinear system parameters over different stages of fatigue cycles
- Analyze and compare the results of the analytical model and experiments
- Elaborate on the value and potential applications of monitoring nonlinear dynamic parameters

Drawing on the previous sections, the following main research question is postulated:

■ **Can nonlinear dynamic analysis lead to improved damage precursor detection and why?**

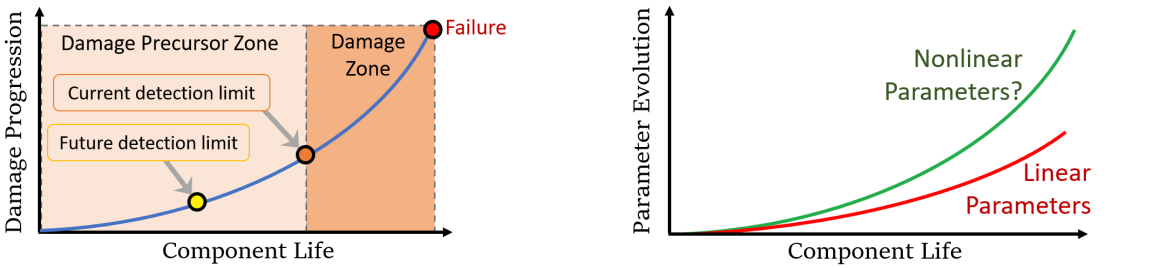

(a) The way forward for damage detection

(b) Potential increased sensitivity of nonlinear parameters

Figure 1.7: Main research ideas

The main question is broken down into several sub-questions, which are:

1. Which nonlinear effects (e.g. stiffness, damping, inertial) significantly contribute to the system dynamics and are therefore important to include in the analysis?
2. Can the applied analytical model accurately describe the experimental results?

3. How sensitive are the changes in nonlinear parameters over fatigue cycles compared to changes in the standard linear parameters? (visualized in Figure 1.7b)
4. What is the potential value of including nonlinear analysis in SHM applications?

1.4 Methodology

To accomplish the stated research goal and objectives, a strategic research method has been developed, which is visualized in Figure 1.8. An analytical approach and an experimental approach are followed. Based on the review, suitable analytical and experimental methods are chosen. As these methods are thoroughly detailed in further chapters, they are discussed briefly here.

The **analytical approach** was followed to develop the Equation of Motion (EoM) for the system and to model its response, which were detailed in Chapter 2. Techniques applied to derive the EoM include the Nonlinear 2D Euler-Bernouilli beam theory and the Assumed Modes method. To model the system response, HBM, MoA and numerical methods (Runge-Kutta) were employed. **Experiments** were set up and carried out to characterize linear and nonlinear system parameters over different levels of fatigue. A cantilever beam made of aluminum (Al 7075-T6) was used as the system of focus. The dynamic characterizations included sine-sweep excitation (forced), and free vibration (transient). For each characterization, tests for the nonlinear and linear region were conducted. A signal processing approach was subsequently applied to convert the collected experimental data into useful results. By employing fatigue testing, the results were correlated to different levels of component health. The experimental method and the data processing approach were detailed in Chapter 3. The experimental and analytical results were compared and discussed in Chapter 4. Finally, Chapter 5 contains the conclusions and recommendations for future work.

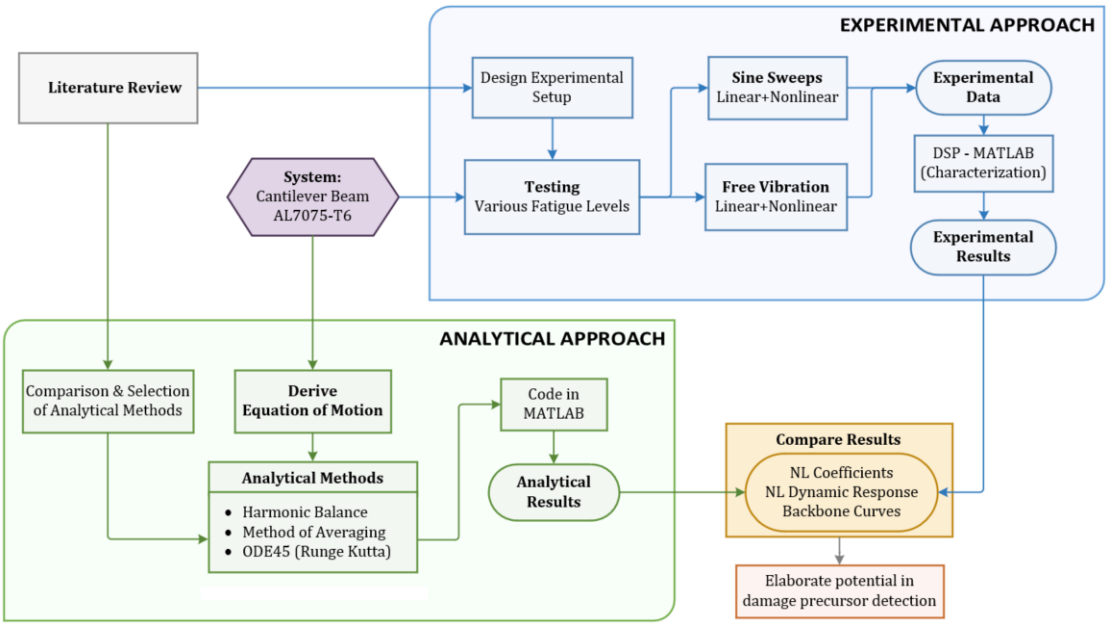

Figure 1.8: Research Methodology

CHAPTER 2

Analytical Approach

This chapter details the analytical methods applied for modeling the dynamic response of cantilever beams. Firstly, in section 2.1, the kinematics are derived for the dynamic system, and the equation of motion is developed. Hereafter various analytical methods are explored to model the nonlinear vibration response of the cantilever beam system. These methods include Harmonic Balance (section 2.2), the Method of Averaging (section 2.3), and Runge-Kutta (section 2.4).

2.1 Equation of Motion Development

A cantilever beam is considered having a uniform cross-section with a length L, width b, and thickness h. The beam has a uniform volumetric density ϱ, and cross-sectional area A. The distributive mass is denoted by m_s, and the rotary inertia is denoted by I_r. The beam is clamped rigidly to a support base boundary, which is able to move vertically described by the base displacement Y, as shown in Figure 2.1. The support boundary is excited harmonically in the transverse direction. The selected reference configuration of the beam is a straight stress-free state.

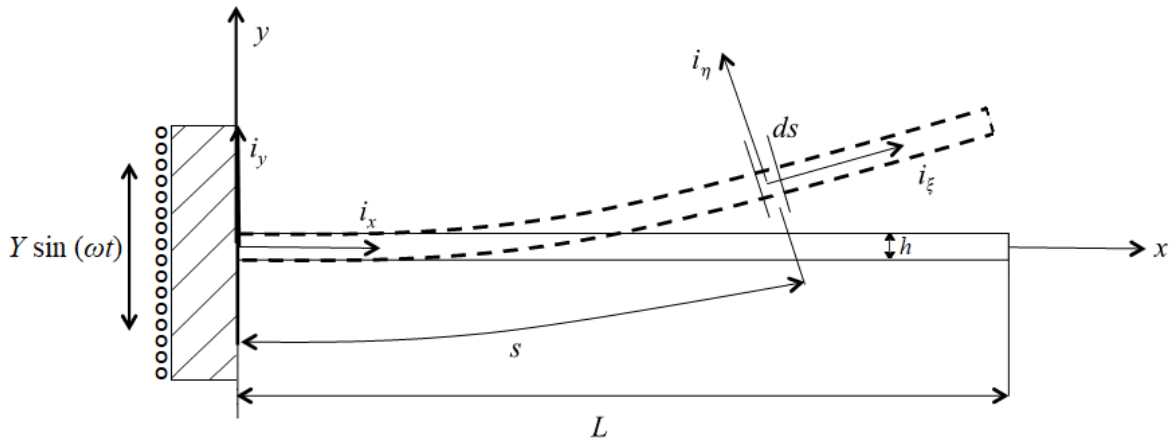

Figure 2.1: The nonlinear 2D Euler-Bernoulli beam theory with the undeformed coordinate system xy and the deformed coordinate system $\xi\eta$.

If the length to thickness ratios of structures are ≥ 10, they can be represented using an Euler-Bernoulli beam model [23]. Since the beam length to width ratio is kept short (<30), the assumption can be made that the beam undergoes purely planar flexural vibrations, as long as the cross-section

geometry remains symmetric with respect to the beam's centerline [25]. The beam is assumed to be inextensible, which means that the stretching of the beam's neutral axis can be neglected. The effects of torsion and shear deformation are also ignored in the analysis [25]. To account for the various nonlinearities, the Nonlinear 2D Euler-Bernoulli beam theory is followed as described in [81].

Two coordinate systems are hereby used to describe the undeformed and deformed geometries of an initially straight beam. The xy system is a Cartesian system describing the undeformed geometry and the $\xi\eta$ system is a local, orthogonal curvilinear coordinate system describing the deformed geometry, as shown in Figure 2.1. Each differential beam element has infinitesimal thickness ds and a fixed finite area. The base motion causes each point on the undeformed cross-section of the beam to experience an elastic displacement. The deformation with respect to the x, and y axes along the beam's undeformed arclength from the fixed-end to a reference point, s, and time, t, are expressed in terms of two displacements and one rotation: axial displacement, $u(s,t)$, transverse displacement, $v(s,t)$ and rotational angle, $\theta(s,t)$. These displacements are visualized in Figure 2.2. Throughout the analysis the overdots ($\dot{}$) denote the temporal partial derivatives with respect to time, t, and the primes ($'$) indicate the spatial partial derivatives with respect to position, s.

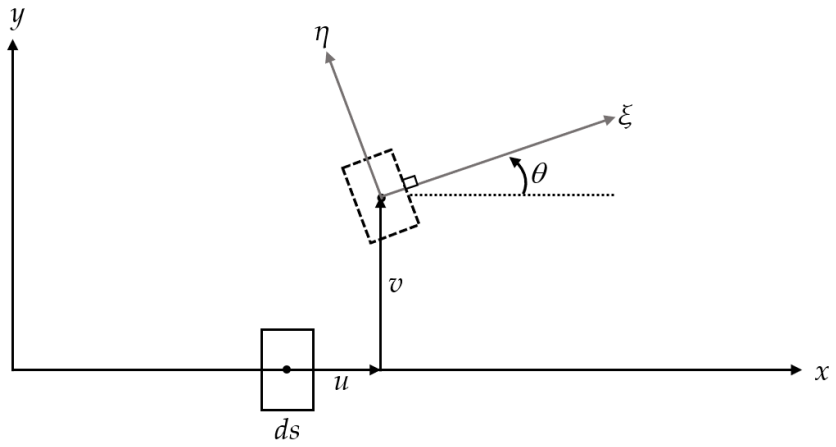

Figure 2.2: The displacements u and v and rotation angle θ [81].

The displacement vector can be expressed as follows:

$$\mathbf{R} = (s+u)\mathbf{i_x} + v\mathbf{i_y} + \eta\mathbf{i}_\eta \tag{2.1}$$

By substituting $\mathbf{i}_\eta = -\sin\theta\mathbf{i_x} + \cos\theta\mathbf{i_y}$, this reduces to:

$$\mathbf{R} = (s+u-\eta\sin\theta)\mathbf{i_x} + (v+\eta\cos\theta)\mathbf{i_y} \tag{2.2}$$

The time derivative of the displacement vector, with $\dot{Y}$ included to account for the base fixture velocity in the transverse direction, becomes:

$$\dot{\mathbf{R}} = (\dot{u}-\eta\dot{\theta}\cos\theta)\mathbf{i_x} + (\dot{Y}+\dot{v}-\eta\dot{\theta}\sin\theta)\mathbf{i_y} \tag{2.3}$$

The kinetic energy of the cantilever beam system can be expressed as [27]:

$$T = \frac{1}{2}\int_0^L \int_A \rho\dot{\mathbf{R}}\cdot\dot{\mathbf{R}}\,\mathrm{d}A\,\mathrm{d}s \tag{2.4}$$

Substituting Equation 2.3 in Equation 2.4 then results in:

$$T = \frac{\varrho}{2}\int_0^L \int_A \left[(\dot{u} - \eta\dot{\theta}\cos\theta)\mathbf{i_x} + (\dot{Y} + \dot{v} - \eta\dot{\theta}\sin\theta)\mathbf{i_y}\right]^2 \mathrm{d}A\,\mathrm{d}s \tag{2.5}$$

$$T = \frac{\varrho}{2}\int_0^L \int_A \left[(\dot{u}^2 + \dot{v}^2 + \dot{Y}^2 + 2\dot{v}\dot{Y} + \eta^2\dot{\theta}^2 - 2\eta\dot{u}\dot{\theta}\cos\theta - 2\eta\dot{v}\dot{\theta}\sin\theta - 2\eta\dot{Y}\dot{\theta}\sin\theta\right] \mathrm{d}A\,\mathrm{d}s \tag{2.6}$$

The following parameters are set:

$$m_s = \int_A \varrho\,\mathrm{d}A \qquad I_r = \int_A \varrho\eta^2\,\mathrm{d}A \tag{2.7}$$

$$I_r = \frac{\varrho}{3}\int_{-\frac{b}{2}}^{+\frac{b}{2}} \frac{h^3}{4}\,\mathrm{d}\zeta = \varrho h b\left(\frac{h^2}{12}\right) = \frac{m_s h^2}{12} \tag{2.8}$$

The product of inertia is set to zero because the reference axis coincides with the mass centroid and the associated terms can thus be omitted from analysis.

Upon substitution and elimination of irrelevant terms in Equation 2.6, the following is obtained:

$$T = \frac{1}{2}\int_0^L \left[m_s\left[\dot{u}^2 + \left(\dot{v} + \dot{Y}\right)^2\right] + I_r\dot{\theta}^2\right] \mathrm{d}s \tag{2.9}$$

The strain energy is considered to be a function of the bending strain only, because of the inextensionality assumption, which renders the axial strain to be zero. The potential energy due to the gravitational force is considered negligible as the beam is considered straight in equilibrium position. Therefore the expression for the total potential energy of the system becomes:

$$\Pi = \frac{1}{2}\int_0^L EI\rho^2\,\mathrm{d}s \tag{2.10}$$

where: E is the material elastic constant (Young's modulus),
I is the second moment of inertia,
ρ is the normalized bending curvature (associated with pure bending).

It follows from Figure 2.2 that the axial strain is given by:

$$e = \sqrt{(1+u')^2 + v'^2} - 1 \tag{2.11}$$

By applying the inextensionality constraint ($e = 0$) this reduces to:

$$(1+u')^2 + v'^2 = 1 \tag{2.12}$$

To express the nonlinear displacement and its partial derivatives in convenient forms, Taylor Series expansions are performed and terms up to the cubic order are kept. It is assumed that u and v are small

but finite and the influence of higher order terms is insignificant. The simplification process begins by obtaining up to the order three Taylor series expansions of u' and θ as follows [81]:

$$u' + 1 = \sqrt{1 - v'^2} = 1 - \tfrac{1}{2}v'^2 - \tfrac{1}{8}v'^4 - \tfrac{1}{16}v'^6 - \tfrac{5}{128}v'^8 + ..., \qquad u' \approx -\tfrac{1}{2}v'^2 \tag{2.13a}$$

$$\sin\theta = v', \qquad \theta = \arcsin v' = v' + \tfrac{1}{6}v'^3 + \tfrac{3}{40}v'^5 + \tfrac{5}{112}v'^7 + ..., \qquad \theta \approx v' + \frac{1}{6}v'^3 \tag{2.13b}$$

The time derivative of (θ) and the squared thereof are approximated by:

$$\dot{\theta} \approx \dot{v}' + \tfrac{1}{2}\dot{v}'v'^2, \qquad \dot{\theta}^2 \approx \dot{v}'^2 + \dot{v}'^2 v'^2 \tag{2.14}$$

The normalized bending curvature and the squared curvature become:

$$\rho = \theta' = v'' + \frac{1}{2}v''v'^2 \tag{2.15a}$$

$$\rho^2 = v''^2 + v''^2 v'^2 + \frac{1}{4}v''^2 v'^4 \approx v''^2 + v''^2 v'^2 \tag{2.15b}$$

To express the time derivates of u in terms of v, the following is obtained:

$$u = -\frac{1}{2}\int_0^\xi v'^2 \,\mathrm{d}s, \qquad \dot{u} \quad = -\frac{1}{2}\frac{\partial}{\partial t}\int_0^\xi v'^2 \,\mathrm{d}s, \qquad \dot{u}^2 = \frac{1}{4}\Big(\frac{\partial}{\partial t}\int_0^\xi v'^2 \,\mathrm{d}s\Big)^2 \tag{2.16}$$

Subsequently, the kinetic and potential energies are expressed as follows:

$$T = \frac{1}{2}\int_0^L m_s\left[\frac{1}{4}\Big(\frac{\partial}{\partial t}\int_0^\xi v'^2 \,\mathrm{d}s\Big)^2 + \Big(\dot{v} + \dot{Y}\Big)^2\right]\mathrm{d}s + \frac{1}{2}\int_0^L I_r\Big(\dot{v}'^2 + \dot{v}'^2 v'^2\Big)\mathrm{d}s \tag{2.17a}$$

$$\Pi = \frac{1}{2}\int_0^L EI\Big(v''^2 + v''^2 v'^2\Big)\mathrm{d}s \tag{2.17b}$$

In a real dynamic beam system, damping is always present. Hereby a part of the mechanical motion is converted to heat, sound or other forms of energy. The damping force present during the oscillations of the beam is also included in the analysis by introducing a term for the dissipative energy, which is classified as non-conservative energy. A convenient way of treating damping forces is by the use of Rayleigh 's dissipation function where the dissipated energy can be expressed in terms of the linear viscous damping as follows [82]:

$$D = \frac{1}{2}\int_0^L c\dot{v}^2 ds \tag{2.18}$$

where c is the viscous damping coefficient.

Unlike discrete systems where the governing equations are Ordinary Differential Equations (ODEs), continuous or distributed mass systems are governed by spatial-temporal Partial Differential Equations (PDEs). Therefore, these systems require converting the PDEs (as the one expressed by Equation 2.17) to more manageable temporal forms. This can be achieved by the use of various discretization methods. Common methods used for the discretization of such problems include the Rayleigh-Ritz method and

the Gallerkin method [83]. In this work, the Assumed-Modes method is applied to obtain the discretized EoM for the cantilever beam system. This method is closely related to the Rayleigh-Ritz method and it is best suitable to model the forced response. The method removes the position dependence from the PDEs such that the displacement at a single point on the structure can be expressed as a function of time only [84]. The Assumed-Modes method begins with the discretization of the boundary-value problem. The method requires assumed approximate functions for the mode shapes of the continuous system. These mode shapes are then substituted into the PDEs. The Assumed Modes expansion and Euler-Lagrangian approach together can be utilized to ensure stability and periodicity analysis [85]. Assumed solutions are the response contribution of n-th modes [84], given by:

$$v(t,s) = \sum_{n=1}^{N} \Psi_n(s) q_n(t) \tag{2.19}$$

where Ψ_n denotes the eigenfunctions of the continuous structure, which is given by a sufficiently differentiable orthogonal set of trial functions to satisfy the kinematic boundary conditions of the system and q_n denotes the generalized coordinates, which are a function of time, that represent the time modulation of the n^{th} mode and Ψ_n.

Considering the single mode assumed solution (first mode only; $N = 1$), v can now be expressed in terms of Ψ and q:

$$v(t,s) = \Psi(s) q(t) \tag{2.20}$$

Subsequently, by substituting the assumed solution, the kinetic, potential and dissipative energies are now expressed as follows:

$$\begin{aligned} T = \frac{1}{2}\left[m_s \int_0^L \Psi^2 \,\mathrm{d}s + I_r \int_0^L \Psi'^2 \,\mathrm{d}s \right] \dot{q}^2 + \frac{1}{2}\left[m_s \int_0^L \left(\int_0^\xi \Psi'^2 \,\mathrm{d}s \right)^2 \mathrm{d}s + I_r \int_0^L \Psi'^4 \,\mathrm{d}s \right] q^2 \dot{q}^2 \\ + \left[m_s \int_0^L \Psi \,\mathrm{d}s \right] \dot{Y} \dot{q} + \frac{1}{2}\left[m_s \int_0^L \mathrm{d}s \right] \dot{Y}^2 \end{aligned} \tag{2.21a}$$

$$\Pi = \frac{1}{2}\left[\int_0^L EI \Psi''^2 \,\mathrm{d}s \right] q^2 + \frac{1}{2}\left[\int_0^L EI \Psi''^2 \Psi'^2 \,\mathrm{d}s \right] q^4 \tag{2.21b}$$

$$D = \frac{1}{2}\left[c \int_0^L \Psi^2 \,\mathrm{d}s \right] \dot{q}^2 \tag{2.21c}$$

For distributed-parameter oscillatory systems (continuous systems) Lagrangian mechanics are the method of choice for deriving equations of motion [84]. The Euler-Lagrangian equation is applied. With a term included to account for dissipative energy, this equation is expressed as [82]:

$$\frac{\partial}{\partial t}\left(\frac{\partial \mathscr{L}}{\partial \dot{q}} \right) - \frac{\partial \mathscr{L}}{\partial q} + \frac{\partial D}{\partial \dot{q}} = 0 \tag{2.22}$$

where $\mathscr{L}$ denotes the Lagrangian for a system, which is defined by: $\mathscr{L} = T - \Pi$. Noting that the potential energy is not a function of the generalized velocities, Equation 2.22 is now written as:

$$\frac{\partial}{\partial t}\left(\frac{\partial T}{\partial \dot{q}} \right) - \frac{\partial T}{\partial q} + \frac{\partial \Pi}{\partial q} + \frac{\partial D}{\partial \dot{q}} = 0 \tag{2.23}$$

The individual terms of Equation 2.23 are worked out as follows:

$$\frac{\partial T}{\partial q} = \left[m_s \int_0^L \left(\int_0^\xi \Psi'^2 \, \mathrm{d}s \right)^2 \mathrm{d}s + I_r \int_0^L \Psi'^4 \, \mathrm{d}s \right] q \dot{q}^2 \tag{2.24a}$$

$$\frac{\partial \Pi}{\partial q} = \left[\int_0^L EI \Psi''^2 \, \mathrm{d}s \right] q + 2 \left[\int_0^L EI \Psi''^2 \Psi'^2 \, \mathrm{d}s \right] q^3 \tag{2.24b}$$

$$\frac{\partial D}{\partial \dot{q}} = \left[c \int_0^L \Psi^2 \, \mathrm{d}s \right] \dot{q} \tag{2.24c}$$

$$\begin{aligned} \frac{\partial T}{\partial \dot{q}} = &\left[m_s \int_0^L \Psi^2 \, \mathrm{d}s + I_r \int_0^L \Psi'^2 \, \mathrm{d}s \right] \dot{q} + \left[m_s \int_0^L \left(\int_0^\xi \Psi'^2 \, \mathrm{d}s \right)^2 \mathrm{d}s + I_r \int_0^L \Psi'^4 \, \mathrm{d}s \right] q^2 \dot{q} \\ &+ \left[m_s \int_0^L \Psi \, \mathrm{d}s \right] \dot{Y} \end{aligned} \tag{2.24d}$$

$$\begin{aligned} \frac{\partial}{\partial t} \left(\frac{\partial T}{\partial \dot{q}} \right) = &\left[m_s \int_0^L \Psi^2 \, \mathrm{d}s + I_r \int_0^L \Psi'^2 \, \mathrm{d}s \right] \ddot{q} + \left[m_s \int_0^L \left(\int_0^\xi \Psi'^2 \, \mathrm{d}s \right)^2 \mathrm{d}s + I_r \int_0^L \Psi'^4 \, \mathrm{d}s \right] q^2 \ddot{q} \\ &+ 2 \left[m_s \int_0^L \left(\int_0^\xi \Psi'^2 \, \mathrm{d}s \right)^2 \mathrm{d}s + I_r \left(\int_0^L \Psi'^4 \, \mathrm{d}s \right) \right] q \dot{q}^2 + \left[m_s \left(\int_0^L \Psi \, \mathrm{d}s \right) \right] \ddot{Y} \end{aligned} \tag{2.24e}$$

Upon obtaining and rearranging the result of the Euler-Lagrangian, the following is produced:

$$\begin{aligned} &\left[m_s \int_0^L \Psi^2 \, \mathrm{d}s + I_r \int_0^L \Psi'^2 \, \mathrm{d}s \right] \ddot{q} \\ &+ \left[m_s \int_0^L \left(\int_0^\xi \Psi'^2 \, \mathrm{d}s \right)^2 \mathrm{d}s + I_r \int_0^L \Psi'^4 \, \mathrm{d}s \right] q^2 \ddot{q} \\ &+ \left[m_s \int_0^L \left(\int_0^\xi \Psi'^2 \, \mathrm{d}s \right)^2 \mathrm{d}s + I_r \int_0^L \Psi'^4 \, \mathrm{d}s \right] q \dot{q}^2 \\ &+ \left[c \int_0^L \Psi^2 \, \mathrm{d}s \right] \dot{q} \\ &+ \left[\int_0^L EI \Psi''^2 \, \mathrm{d}s \right] q \\ &+ \left[2 \int_0^L EI \Psi''^2 \Psi'^2 \, \mathrm{d}s \right] q^3 \\ &= - \left[m_s \int_0^L \Psi \, \mathrm{d}s \right] \ddot{Y} \end{aligned} \tag{2.25}$$

By introducing new coefficients to simplify Equation 2.25, the resulting equation of motion can now be formulated as:

$$m_1 \ddot{q} + m_3 \left(q^2 \ddot{q} + q \dot{q}^2 \right) + c_1 \dot{q} + k_1 q + k_3 q^3 = m_b \ddot{Y} \tag{2.26}$$

where:

$$
\begin{aligned}
&\text{Linear inertial coefficient:} && m_1 = m_s \int_0^L \Psi^2 \,\mathrm{d}s + \int_0^L I_r \Psi'^2 \,\mathrm{d}s \\
&\text{Nonlinear inertial coefficient:} && m_3 = m_s \int_0^L \left(\int_0^\xi \Psi'^2 \,\mathrm{d}s \right)^2 \mathrm{d}s + I_r \int_0^L \Psi'^4 \,\mathrm{d}s \\
&\text{Viscous damping coefficient:} && c_1 = c \int_0^L \Psi^2 \,\mathrm{d}s \\
&\text{Linear stiffness coefficient:} && k_1 = \int_0^L EI \Psi''^2 \,\mathrm{d}s \\
&\text{Cubic stiffness coefficient:} && k_3 = 2 \int_0^L EI \Psi''^2 \Psi'^2 \,\mathrm{d}s \\
&\text{Driving inertial coefficient:} && m_b = -m_s \int_0^L \Psi \,\mathrm{d}s
\end{aligned}
\tag{2.27}
$$

Similar expressions for a cantilever beam EoM were obtained and applied by researchers [23, 26]. To determine the coefficients, the derived equations are coded in MATLAB, by using the code created by [26] and making modifications to fit the current use case.

The mode shapes are obtained using the widely known differential eigenvalue problem, as applied in [84]. In the case of free vibration of a cantilever beam, this takes the form of the following differential equation:

$$
\frac{\mathrm{d}^4 \Psi(x)}{\mathrm{d}x^4} - \beta^4 \Psi(x) = 0, \qquad 0 < x < L; \qquad \text{with: } \beta^4 = \frac{\omega^2 m_s}{EI} \tag{2.28}
$$

The general mode shape can thereby be expressed as [84]:

$$
\Psi(x) = \alpha_1 \cos \beta x + \alpha_2 \sin \beta x + \alpha_3 \cosh \beta x + \alpha_4 \sinh \beta x \tag{2.29}
$$

In order to produce the modal equations, the boundary conditions for a cantilever beam are applied on Equation 2.29, which are:

$$
\begin{aligned}
&\Psi(x) = 0, \qquad \Psi'(x) = 0, \qquad \text{at} \quad x = 0 \\
&\Psi''(x) = 0, \qquad \Psi'''(x) = 0, \qquad \text{at} \quad x = L
\end{aligned}
\tag{2.30}
$$

Applying the boundary conditions leads to the characteristic equation:

$$
\cos(\beta L) \cosh(\beta L) = -1 \tag{2.31}
$$

The transcendental equation is solved numerically to produce the eigenvalues, of which the first three solutions of βL are: $\beta_1 L = 1.875104$, $\beta_2 L = 4.694091$, $\beta_3 L = 7.854757$. The first three mode shapes are visualized in Figure 2.3.

After applying the boundary conditions, the corresponding mode shape for each vibrational mode (n) can then be expressed as [26]:

$$
\Psi_n(x) = A_n \Big(\cos(\beta_n x) - \cosh(\beta_n x) + \frac{\sin(\beta_n L) - \sinh(\beta_n L)}{\cos(\beta_n L) + \cosh(\beta_n L)} \big(\sin(\beta_n x) - \sinh(\beta_n x) \big) \Big) \tag{2.32}
$$

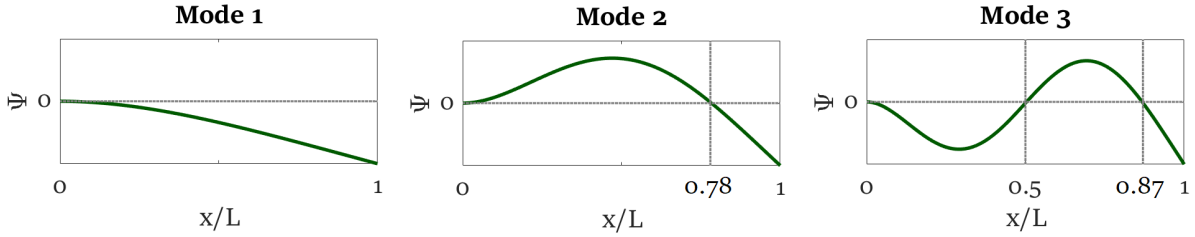

Figure 2.3: First three analytically derived mode shapes

The eigenfunction and its spatial derivatives necessary for calculating the coefficients are thus:

$$\Psi_n(x) = A_n\Big(\cos(\beta_n x) - \cosh(\beta_n x) + C_n\big(\sin(\beta_n x) - \sinh(\beta_n x)\big)\Big) \tag{2.33a}$$

$$\Psi_n'(x) = A_n\beta_n\Big(-\sin(\beta_n x) - \sinh(\beta_n x) + C_n\big(\cos(\beta_n x) - \cosh(\beta_n x)\big)\Big) \tag{2.33b}$$

$$\Psi_n''(x) = A_n\beta_n^2\Big(-\cos(\beta_n x) - \cosh(\beta_n x) + C_n\big(-\sin(\beta_n x) - \sinh(\beta_n x)\big)\Big) \tag{2.33c}$$

where:

$$C_n = \frac{\sin(\beta_n L) - \sinh(\beta_n L)}{\cos(\beta_n L) + \cosh(\beta_n L)} \tag{2.34}$$

From this, the natural frequencies for the n^{th} mode can be obtained:

$$\omega_n = (\beta_n L)^2\sqrt{\frac{EI}{m_s L^4}} \tag{2.35}$$

The eigenvectors are normalized by the total mass of the system to obtain the modal amplitude constant A_n, such that:

$$\int_0^L m_s\Psi_i\Psi_j\,\mathrm{d}s + \int_0^L I_r\Psi_i'\Psi_j'\,\mathrm{d}s = \delta_{ij} \tag{2.36}$$

where δ_{ij} is the Kronecker delta ($\delta_{ij} = 1$ for $i = j$).

Thus A_n is calculated using:

$$A_n = \sqrt{\frac{1}{m_s\int_0^L\left(\frac{\Psi}{A_n}\right)^2\mathrm{d}s + I_r\int_0^L\left(\frac{\Psi'}{A_n}\right)^2\mathrm{d}s}} \tag{2.37}$$

The final equation of motion for the cantilever beam system then becomes (substitute $\hat{F} = m_b\ddot{Y}$):

$$\ddot{q} + m_3\Big(q^2\ddot{q} + q\dot{q}^2\Big) + c_1\dot{q} + k_1 q + k_3 q^3 = \hat{F} \tag{2.38}$$

2.2 Harmonic Balance

Within SHM, the most widely-used method of visualizing the input–output properties of a dynamic system is by means of the FRF. The Harmonic Balance Method (HBM) is an applied mathematical method which allows the FRF approximation of nonlinear systems [16]. Thus, the steady-state response of nonlinear differential equations can be calculated in the frequency domain. In this work, HBM is applied to simulate the response of the slow sine-sweep excitation, which is essentially equivalent to the steady state amplitude of the beam due to stepped sine excitation. HBM is also applicable for differential equations where the nonlinear terms are not small [86]. One of the major advantages of HBM is that the different nonlinearities are additively separable within the technique [16]. This means that an additional nonlinearity can easily be incorporated into the existing model. Additionally, unlike numerical techniques for solving ODEs, HBM calculates equivalent linear and nonlinear expressions for a dynamical systems algebraically more efficiently. The expressions state for example the magnitude of the effective stiffness or the effective damping as a function of the response amplitude. Those expressions can be employed to identify experimental coefficients through curve fitting techniques on experimental results, such as backbone curves and damping skeletons (which are discussed in chapter 3).

2.2.1 Nonlinear Stiffness

This section details the harmonic balance method for solving the equation of motion for a damped dynamic system with a cubic stiffness, which is known as the damped Duffing oscillator [16]. The equation of motion of this system takes the following form:

$$\ddot{q} + c_1\dot{q} + k_1 q + k_3 q^3 = \hat{F}\sin(\omega t - \phi) \tag{2.39}$$

where ω is the excitation frequency and ϕ is the phase.

Upon using HBM, it is assumed that the response due to a sinusoidal excitation is a sinusoid, and has the same frequency. Hereby, a harmonic trial solution is substituted into the EoM (2.39). Using the first-order trial solution, $q = \alpha\sin(\omega t)$, where α is the amplitude, yields:

$$-\omega^2\alpha\sin(\omega t) + c_1\omega\alpha\cos(\omega t) + k_1\alpha\sin(\omega t) + k_3\alpha^3\sin^3(\omega t) = \hat{F}\sin(\omega t - \phi) \tag{2.40}$$

After applying the trigonometric relationships ($\sin 3\theta = 3\sin\theta - 4\sin^3\theta$), and ($\sin(A-B) = \sin A\cos B - \cos A\sin B$), the following is obtained:

$$\begin{aligned} -\omega^2\alpha\sin(\omega t) + c_1\omega\alpha\cos(\omega t) + k_1\alpha\sin(\omega t) + k_3\alpha^3\left(\tfrac{3}{4}\sin(\omega t) - \tfrac{1}{4}\sin(3\omega t)\right) \\ = \hat{F}\sin(\omega t)\cos\phi - \hat{F}\cos(\omega t)\sin\phi \end{aligned} \tag{2.41}$$

Equating the coefficients of $\sin(\omega t)$ and $\cos(\omega t)$ yields the following equations:

$$-\omega^2\alpha + k_1\alpha + \tfrac{3}{4}k_3\alpha^3 = \hat{F}\cos\phi \tag{2.42}$$

$$c_1\omega\alpha = -\hat{F}\sin\phi \tag{2.43}$$

Squaring and adding Equation 2.42 and Equation 2.43 results in:

$$\hat{F}^2 = \alpha^2 \left[\left(-\omega^2 + k_1 + \tfrac{3}{4} k_3 \alpha^2 \right)^2 + c_1^2 \omega^2 \right] \tag{2.44}$$

$$\frac{\hat{F}^2}{\alpha^2} = \omega^4 + \left(c_1^2 - 2k_1 - \tfrac{6}{4} k_3 \alpha^2 \right) \omega^2 + \tfrac{9}{16} k_3^2 \alpha^4 + \tfrac{6}{4} k_1 k_3 \alpha^2 + k_1^2 \tag{2.45}$$

Upon applying the quadratic formula, the roots are obtained, which yields the following expression for ω, based on a given input force and response amplitude:

$$\omega_{1,2} = \sqrt{\left(k_1 + \tfrac{3}{4} k_3 \alpha^2 - \tfrac{1}{2} c_1^2 \right) \pm \sqrt{-c_1^2 \left(k_1 + \tfrac{3}{4} k_3 \alpha^2 - \tfrac{1}{4} c_1^2 \right) + \frac{\hat{F}^2}{\alpha^2}}} \tag{2.46}$$

The system backbone curve is [87]:

$$\omega_{bb} = \sqrt{k_{eq} - \tfrac{1}{2} c_1^2} \tag{2.47}$$

where, k_{eq} is the equivalent stiffness of the dynamic system, which is:

$$k_{eq} = k_1 + \tfrac{3}{4} k_3 \alpha^2 \tag{2.48}$$

2.2.2 Nonlinear Damping

In addition to viscous damping forces encountered by a vibrating system, nonlinear damping can also be present at high response amplitudes. Anderson et al. [88] and Malatkar [83] showed that including quadratic damping in an analytical model may significantly improve the agreement between experimental and theoretical results for vibrating flexible beams. Quadratic damping is usually attributed to drag forces acting on cantilever beams [83, 89]. In the current work, the contribution of nonlinear damping is included in the analysis. Typically, the magnitude of nonlinear damping coefficients are determined experimentally [88, 89].

In the study of nonlinear oscillations, the influence of quadratic damping can be expressed as $c_2|\dot{q}|\dot{q}$ [90]. Hereby c_2 is the quadratic damping coefficient and the absolute velocity term ($|\dot{q}|$) is included to ensure that the force is always opposing the velocity. For compatibility, c_2, similar to the other coefficients, is also normalized by the mass.

The following damping equation is now considered, which includes linear and quadratic damping:

$$f_d(\dot{q}) = c_1 \dot{q} + c_2 |\dot{q}| \dot{q} \tag{2.49}$$

HBM is now applied to obtain the equivalent damping equation, but in a different manner than in subsection 2.2.1. The analysis performed to obtain the equivalent stiffness, although effective, is not very systematic and for other nonlinearities that manner of implementation could fail to produce a valid result [16]. Fortunately, there is a simple procedural way of implementing the HBM method that works for all types of nonlinearities, which is described in [16].

Hereby the relevant function (e.g., stiffness function, damping function or inertial function) first has to be expanded as a Fourier Series [16]. The fundamental terms are thereby considered the only important parts of this expansion. These terms are denoted by a_0, a_1 and b_1.

After applying the Fourier expansion of the fundamental terms on Equation 2.49 (with trial solution: $q = \alpha \sin(\omega t)$), whereby $a_0 = 0$ and $b_1 = 0$, the following expression is used:

$$f_d(\dot{q}) \approx a_1 \cos(\omega t) \approx c_{eq}\dot{q} \approx c_{eq}\omega\alpha \cos(\omega t) \tag{2.50}$$

Thus the equivalent damping becomes (for convenience ωt is substituted with θ):

$$c_{eq} = \frac{a_1}{\omega\alpha} = \frac{1}{\pi\omega\alpha}\int_0^{2\pi} f_d(\omega\alpha\cos\theta)\cos\theta \,\mathrm{d}\theta \tag{2.51}$$

$$c_{eq} = \frac{c_1}{\pi\omega\alpha}\int_0^{2\pi} \omega\alpha\cos^2\theta \,\mathrm{d}\theta + \frac{c_2}{\pi\omega\alpha}\int_0^{2\pi} \omega^2\alpha^2\cos^2\theta|\cos\theta| \,\mathrm{d}\theta \tag{2.52}$$

Finally, the equivalent damping can be expressed as:

$$c_{eq} = c_1 + \frac{8c_2\omega_n\alpha}{3\pi} \tag{2.53}$$

Similar expressions for the equivalent stiffness and the equivalent damping have been employed by [10] and [7], where they used the equations combined with curve fitting techniques to experimentally estimate the nonlinear stiffness and damping coefficients.

2.2.3 Nonlinear Inertia

The nonlinear inertial term can be simplified using HBM. Similar to the derivations in section 2.1, the linear and nonlinear inertial terms are expressed as:

$$f_m(\ddot{q}) = \ddot{q} + m_3(q\dot{q}^2 + q^2\ddot{q}) \tag{2.54}$$

By substituting the trial solution, $q = \alpha\sin(\omega t)$, into Equation 2.54, the following is obtained:

$$f_m(\ddot{q}) = -\omega^2\alpha\sin(\omega t) + m_3\omega^2\alpha^3\sin(\omega t)\cos^2(\omega t) - m_3\omega^2\alpha^3\sin^3(\omega t) \tag{2.55}$$

The Fourier Series expansion is employed on Equation 2.55, (whereby $a_0 = 0$ and $a_1 = 0$) to yield:

$$b_1 = -\omega^2\alpha\left(1 + \tfrac{1}{2}m_3\alpha^2\right) \tag{2.56}$$

Subsequently, the equivalent mass can be determined by the following relation:

$$f_m(\ddot{q}) \approx b_1\sin(\omega t) \approx m_{eq}\ddot{q} \approx -m_{eq}\omega^2\alpha\sin(\omega t) \tag{2.57}$$

Thus:

$$m_{eq} = 1 + \tfrac{1}{2}m_3\alpha^2 \tag{2.58}$$

2.2.4 General Expression for the Nonlinear FRF

After obtaining the equivalent expressions for the system's mass, stiffness and damping, it is necessary to derive a general expression to obtain the FRF and backbone. The relationship between $\hat{F}$ and α can be expressed as [16]:

$$\hat{F}^2 = \alpha^2 \left[\left(k_{eq} - m_{eq}\omega^2 \right)^2 + c_{eq}^2 \omega^2 \right] \tag{2.59}$$

$$\frac{\hat{F}^2}{\alpha^2} = m_{eq}^2 \omega^4 + \left(c_{eq}^2 - 2 m_{eq} k_{eq} \right) \omega^2 + k_{eq}^2 \tag{2.60}$$

Upon application of the quadratic formula, the equation can be rewritten to calculate the response frequencies corresponding to a given response amplitude and given input force. Via Harmonic Balance, the general formula to obtain frequency values ($\omega_{1,2}$) based on a given amplitude (α) and input force ($\hat{F}$) is derived and expressed as follows:

$$\omega_{1,2} = \sqrt{\frac{m_{eq} k_{eq} - \frac{1}{2} c_{eq}^2 \pm \sqrt{c_{eq}^2 \left(\frac{1}{4} c_{eq}^2 - m_{eq} k_{eq} \right) + \frac{m_{eq}^2 \hat{F}^2}{\alpha^2}}}{m_{eq}^2}} \tag{2.61}$$

This equation can be employed to simulate the FRF of a slow sine-sweep excitation (with fixed input force). Conveniently, using the first part of Equation 2.61, the backbone curve can be expressed as:

$$\omega_{bb} = \sqrt{\frac{k_{eq}}{m_{eq}} - \frac{c_{eq}^2}{2 m_{eq}^2}} \tag{2.62}$$

In figure 2.4 examples are shown of FRFs and backbones plotted using Equation 2.61 and Equation 2.62. The example also clearly shows the effect of each included nonlinear effect.

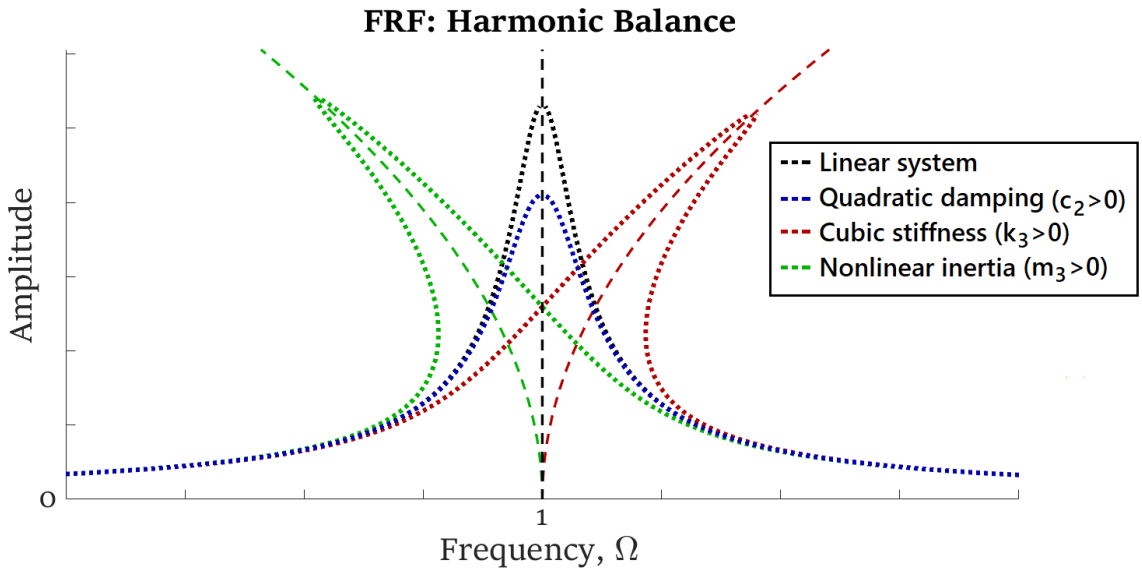

Figure 2.4: Examples of FRFs and backbone curves obtained through HBM, which show the effect of cubic stiffness, nonlinear inertia, and quadratic damping on the shape of the FRF.

2.3 Method of Averaging

This section details the analyses concerned with the free decay of the nonlinear dynamical systems. The decay envelope of a linear (viscous) system response is purely exponential, and the decay speed depends on the linear damping magnitude. For nonlinear systems, the decay envelope has to be modified according to the type of nonlinearity present. In order to determine the envelopes of nonlinear systems an effective technique known as the Method of Averaging (MoA) is utilized [90]. MoA is applied for approximating the response of slow transient response. Thus, the method is adequate for dynamic systems with low damping ratios, as the amplitude and phase do not significantly change over one period. The response is assumed of the form:

$$q(t) = \alpha(t)\sin(\omega_n t + \phi(t)) \tag{2.63}$$

where, the envelope amplitude (α) and the phase (ϕ) vary with time, but slowly compared to the natural period of the system.

The following system is considered, which describes the free decay of an oscillator with nonlinear damping, described by the function $f_d(\dot{q})$:

$$\ddot{q} + f_d(\dot{q}) + \omega_n^2 q = 0 \tag{2.64}$$

The velocity can be represented as:

$$\dot{q}(t) = \alpha(t)\omega_n \cos(\omega_n t + \phi(t)) \tag{2.65}$$

This equation is incomplete, therefore 2.63 is differentiated to uphold consistency, which results in:

$$\dot{q}(t) = \dot{\alpha}(t)\sin(\omega_n t + \phi(t)) + \alpha(t)\omega_n \cos(\omega_n t + \phi(t)) + \alpha(t)\dot{\phi}(t)\cos(\omega_n t + \phi(t)) \tag{2.66}$$

Upon comparison with 2.65 this results in:

$$\dot{\alpha}(t)\sin(\omega_n t + \phi(t)) + \alpha(t)\dot{\phi}(t)\cos(\omega_n t + \phi(t)) = 0 \tag{2.67}$$

Equation 2.65 can be differentiated to yield the acceleration:

$$\ddot{q}(t) = \dot{\alpha}(t)\omega_n \cos(\omega_n t + \phi(t)) - \alpha(t)\omega_n^2 \sin(\omega_n t + \phi(t)) - \alpha(t)\dot{\phi}(t)\omega_n \sin(\omega_n t + \phi(t)) \tag{2.68}$$

Substituting the previous equations into the equation of motion (Equation 2.64) results in:

$$\dot{\alpha}(t)\omega_n \cos(\omega_n t + \phi(t)) - \alpha(t)\dot{\phi}(t)\omega_n \sin(\omega_n t + \phi(t)) = -f_d(\alpha(t)\omega_n \cos(\omega_n t + \phi(t))) \tag{2.69}$$

Multiplying Equation 2.67 by $\omega_n \sin(\omega_n t + \phi(t))$ and 2.69 by $\cos(\omega_n t + \phi(t))$ and adding yields:

$$\dot{\alpha}(t) = -\frac{1}{\omega_n} f_d(\omega_n \alpha(t)\cos(\omega_n t + \phi(t)))\cos(\omega_n t + \phi(t)) \tag{2.70}$$

Multiplying 2.67 by $\omega_n \cos(\omega_n t + \phi(t))$ and 2.69 by $\sin(\omega_n t + \phi(t))$ and differencing yields:

$$\dot{\phi}(t) = -\frac{1}{\omega_n \alpha} f_d(\omega_n \alpha(t)\cos(\omega_n t + \phi(t)))\sin(\omega_n t + \phi(t)) \tag{2.71}$$

These equations together are two first-order differential equations equivalent to the second-order equation (Equation 2.64), which is the original equation of motion. If one makes use of the fact that $\alpha(t)$ and $\phi(t)$ are essentially constant over one vibration period, the right-hand sides of the equations can be replaced by an average over one cycle, as follows (with $\theta = \omega_n t$) [16]:

$$\dot{\alpha}(t) = -\frac{1}{2\pi\omega_n}\int_0^{2\pi} f_d(\omega_n \alpha\cos(\theta+\phi))\cos(\theta+\phi)\,\mathrm{d}\theta \tag{2.72}$$

$$\dot{\phi}(t) = -\frac{1}{2\pi\omega_n \alpha}\int_0^{2\pi} f_d(\omega_n \alpha\cos(\theta+\phi))\sin(\theta+\phi)\,\mathrm{d}\theta \tag{2.73}$$

These two equations can be used to determine the values of the amplitude and the phase over time. In the current work, only Equation 2.72 is applied, because the interest is in the amplitude decay.

At this point it is important to note that the (cubic) nonlinear stiffness term does not have a influence on the shape of the decay envelope. If one were to apply MoA on an undamped Duffing equation, the amplitude rate of change ($\dot{\alpha}(t)$) would equal zero, and the effect of cubic stiffness would manifest as a phase modulation ($\dot{\phi}(t)$) [90, 91]. The same case is assumed for the nonlinear inertial term. Hence, the equation describing the nonlinear damping (Equation 2.74) suffices in the derivation of the damping envelope.

As described in subsection 2.2.2, the suitable equation describing the damping is recalled in slightly different form than Equation 2.49 (by substituting $c_1 = 2\zeta_1\omega_n$):

$$f_d(\dot{q}) = (2\zeta_1\omega_n + c_2|\dot{q}|)\,\dot{q} \tag{2.74}$$

Upon substitution of this equation into Equation 2.72, this produces:

$$\dot{\alpha}(t) = -\frac{1}{2\pi\omega_n}\int_0^{2\pi} (2\zeta_1\omega_n + c_2|\omega_n\alpha\cos(\theta+\phi)|) \quad \omega_n\alpha\cos^2(\theta+\phi) \quad \mathrm{d}\theta \tag{2.75}$$

$$\dot{\alpha}(t) = -\frac{\omega_n\alpha}{2\pi}\int_0^{2\pi} (2\zeta_1 + c_2|\alpha\cos(\theta+\phi|) \quad \cos^2(\theta+\phi) \quad \mathrm{d}\theta \tag{2.76}$$

$$\dot{\alpha}(t) = -\frac{\zeta_1\omega_n\alpha}{\pi}\int_0^{2\pi}\cos^2(\theta+\phi)\,\mathrm{d}\theta - \frac{c_2\omega_n\alpha^2}{2\pi}\int_0^{2\pi}|\cos^3(\theta+\phi)|\,\mathrm{d}\theta \tag{2.77}$$

$$\dot{\alpha}(t) = -\zeta_1\omega_n\alpha(t) - \frac{4c_2\omega_n}{3\pi}\alpha(t)^2 \tag{2.78}$$

The first-order nonlinear differential equation (Equation 2.78) can be solved numerically or analytically to obtain the decay envelope. From this equation the linear and nonlinear part can also be considered separately. Solving the differential equation with an ansatz of $Ce^{-\zeta_1\omega_n t}$ and applying the initial condition for the linear part only (by taking $c_2 = 0$) results in the following expression for an exponential decay [84]:

$$\alpha(t) = \alpha_0 e^{-\zeta_1\omega_n t} \tag{2.79}$$

where, α_0 denotes the initial displacement amplitude at $t = 0$. For vibrations in the small amplitude range this damping model holds up fairly accurate. When the velocity amplitude becomes significantly

large, it becomes necessary to apply nonlinear damping models. Considering the nonlinear part of Equation 2.78 only (by taking $\zeta_1 = 0$), the quadratic decay envelope is [90]:

$$\alpha(t) = \frac{\alpha_0}{1 + \frac{4c_2\omega_n\alpha_0}{3\pi}t} \tag{2.80}$$

In this case, the amplitude decays algebraically rather than exponentially. If the amplitude of the initial displacement is large, one expects the initial decay to be slower for linear damping than for quadratic damping. If the initial amplitude is small, the opposite is true [90]. For small amplitude vibrations quadratic damping solely cannot properly simulate the decay. A proper expression would have to incorporate both damping contributions (linear viscous and quadratic). By solving Equation 2.78, the analytical expression for both damping models combined is obtained. This is achieved through employing the Wolfram|Alpha engine. This leads to the final expression of the decay envelope based on Equation 2.74:

$$\alpha(t) = \frac{\zeta_1\omega_n\alpha_0}{\frac{4c_2\omega_n\alpha_0}{3\pi}(e^{\zeta_1\omega_n t} - 1) + \zeta_1\omega_n e^{\zeta_1\omega_n t}} \tag{2.81}$$

Examples of decay envelopes plotted using Equations 2.79, 2.80, and 2.81 are shown in Figure 2.5.

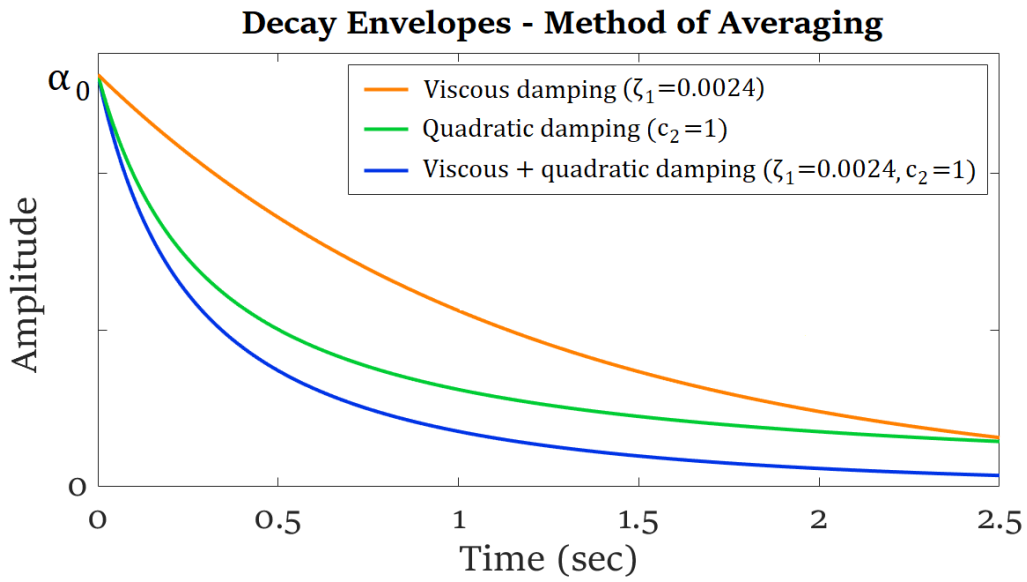

Figure 2.5: Examples of decay envelopes obtained through MoA equations.

2.4 Numerical Method (Runge-Kutta)

The nonlinear EoM is also solved using Runge-Kutta, which is a numerical method that considers a discrete-time solution directly. The technique can be applied to systems for which the nonlinearity is not necessarily small [84]. The numerical integration for the equation of motion is carried out in terms of two first-order ODE equations.

By adding quadratic damping (Equation 2.49) to Equation 2.38, the complete system EoM becomes:

$$\ddot{q} + m_3\left(q^2\ddot{q} + q\dot{q}^2\right) + c_1\dot{q} + c_2|\dot{q}|\dot{q} + k_1 q + k_3 q^3 = \hat{F} \tag{2.82}$$

Equation 2.82 is recast into a set of first-order ODEs in the following manner:

$$\begin{bmatrix} y_1 \\ y_2 \end{bmatrix} = \begin{bmatrix} q \\ \dot{q} \end{bmatrix} \quad \Rightarrow \quad \begin{bmatrix} \dot{y}_1 \\ \dot{y}_2 \end{bmatrix} = \begin{bmatrix} \dot{q} \\ \ddot{q} \end{bmatrix} = \begin{bmatrix} y_2 \\ \frac{-m_3 y_1 y_1^2 - c_1 y_2 - c_2 y_2|y_2| - k_1 y_1 - k_3 y_1^3 + \hat{F}}{1 + m_3 y_1^2} \end{bmatrix} \tag{2.83}$$

MATLAB software includes a function (`ode45`) which is used to conveniently solve the first order equations above. This numerical solver combines an explicit fourth order and a fifth order method (called the Dormand-Prince pair), which is a variation of the common Runge-Kutta method. The solver `ode45` is suitable for a broad range of initial value problems [92]. The numerical method has been used by several authors [7, 10, 93]. An example of a FRF obtained using `ode45` based on Equation 2.82 is depicted in Figure 2.6.

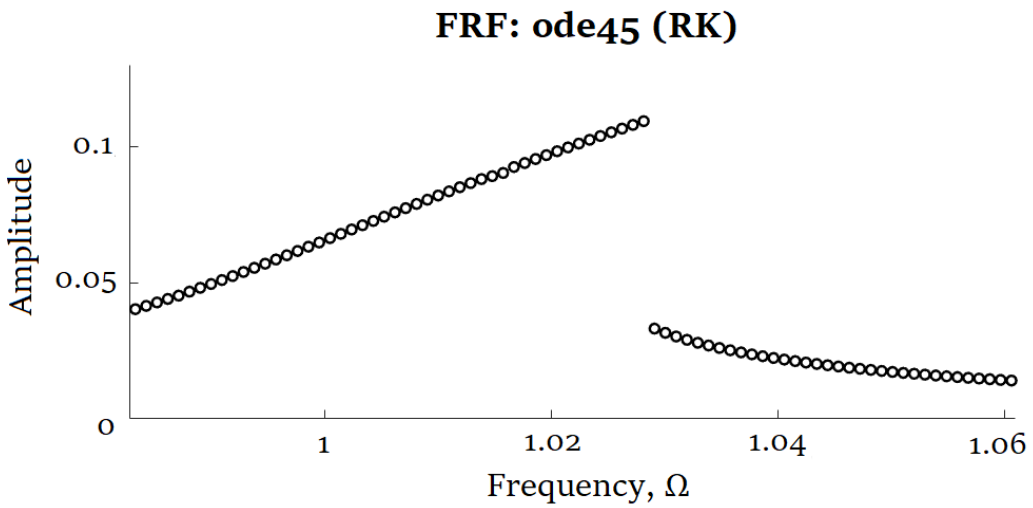

Figure 2.6: Example of a FRF obtained through `ode45` (current result for $m_3 = 2 \cdot 10^4$, ζ_1=0.002, ζ_2=0.002 $k_1 = 1.25 \cdot 10^5$, $k_3 = 2 \cdot 10^{10}$ and $\hat{F} = 2$).

CHAPTER 3

Experimental Design and Method

In this chapter the experimental approach, which entails testing and characterizing the linear and nonlinear dynamic response of cantilever beams at different fatigue damage levels, is detailed. Firstly, in section 3.1 information about the test samples and testing equipment is provided. The test plan is detailed in section 3.2. Several FEM analyses that aided in obtaining necessary testing parameters are provided in section 3.3. The specific testing procedure and test parameters are detailed in section 3.4. Hereafter, in section 3.5, a static deflection experiment performed to investigate the static stiffness of the structure, is discussed. Finally, the data processing methods are detailed in section 3.6.

3.1 Sample Information and Testing Equipment

For the experiments a cantilever beam setup is used with blade-like aluminum beams. The beam samples used for testing are made from aluminum alloy type Al7075-T6, provided by the manufacturer Kaiser Aluminum. Table 3.1 lists the material properties [94] and the complete manufacturers specification is provided in Figure D.3. Figure 3.1 shows a compilation of fatigue data and S-N curves of the material AL7075-T6 obtained from various sources [95] [96] [97] [98]. The beams are dimensioned at a length of 150mm (of which a part is clamped), a width of 50 mm and thickness of 1mm. It is also verified that the grain direction is parallel to the beam length. A picture of a clamped sample is shown in Figure 3.2c.

Property	Value
Density	2810 kg/m^3
Ultimate Tensile Strength	557 MPa
Tensile Yield Strength	485 MPa
Hardness	150 HB
Ultimate Shearing Strength	330 MPa
Fatigue Endurance Limit [(a)]	158 Mpa
Elastic Modulus	71 Gpa

(a) R.R. Moore type endurance limit based on 5×10^8 cycles of completely reversed stress [99].

Table 3.1: Material properties of Al7075-T6

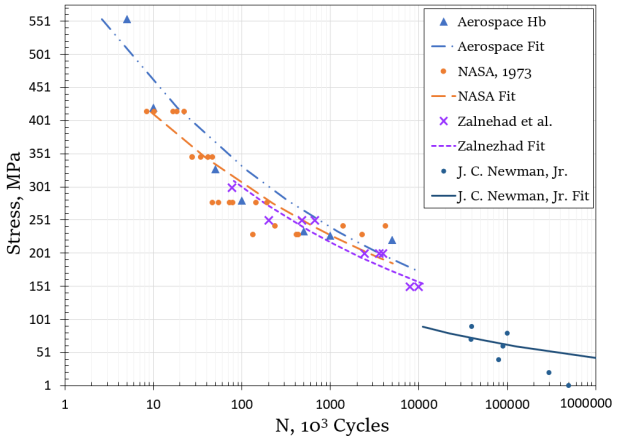

Figure 3.1: Stress versus life (S-N) curves obtained from various sources

The equipment used to perform the experiments include the following:

- Bruel & Kjaer Electrodynamic Vibration Exciter Body Type 4802 with head attachment Type 4817 (Figure 3.2b); used to excite the structure
- Bruel & Kjaer Power Amplifier Type 2708; to amplify the generator signal going to the exciter
- Polytec PSV-500 Scanning Laser Vibrometer and Workstation (Figure 3.2a); used to measure the response velocity at the beam tip, for data acquisition and for excitation signal generation
- Steel fixture (self-manufactured); used to clamp the beam samples and to fasten to the shaker head (Figure 3.2c)
- PCB Piezotronics single-axis accelerometer (Model number: 352A21); used to measure the base acceleration (input)

The software used for generating the excitation signals, monitoring real time testing parameters and collecting all the measurement data is the Polytec Scanning Vibrometer Software Suite.

(a) PSV-500 vibrometer (b) Main test setup (c) Fixture with clamped sample

Figure 3.2: Hardware used for the experiments

3.2 Test Plan

A testing strategy is designed to characterize the linear and nonlinear behavior of cantilever beams over various stages of fatigue life.

1. Linear characterizations conducted at low response amplitudes, consisting of:
   a) Free vibration through initial displacements in the linear region
   b) Sine-sweep excitations over a wide range of frequencies for modal analysis.
2. Nonlinear response characterizations conducted at high response amplitudes, consisting of:
   a) Free vibration through imposed initial displacements at high amplitudes.
   b) Sine-sweep excitations (forward and backward) with a slow frequency rate of change.
3. Fatigue testing to induce different levels of damage to the specimens. After each fatigue test the whole process is repeated again starting at step 1, until the beam has failed.

After having completed all the tests, it is recommended that the samples are further analyzed micro-structurally by utilizing techniques such as DMA and EBSD. This provides the possibility for

analyzing the link between the changes in global dynamic behavior and evolution of microstructural properties. However, this aspect is not considered within the scope of the current work.

Figure 3.3 depicts a schematic overview of the test plan. To describe the plan in more detail, the testing methods are detailed in the following subsections.

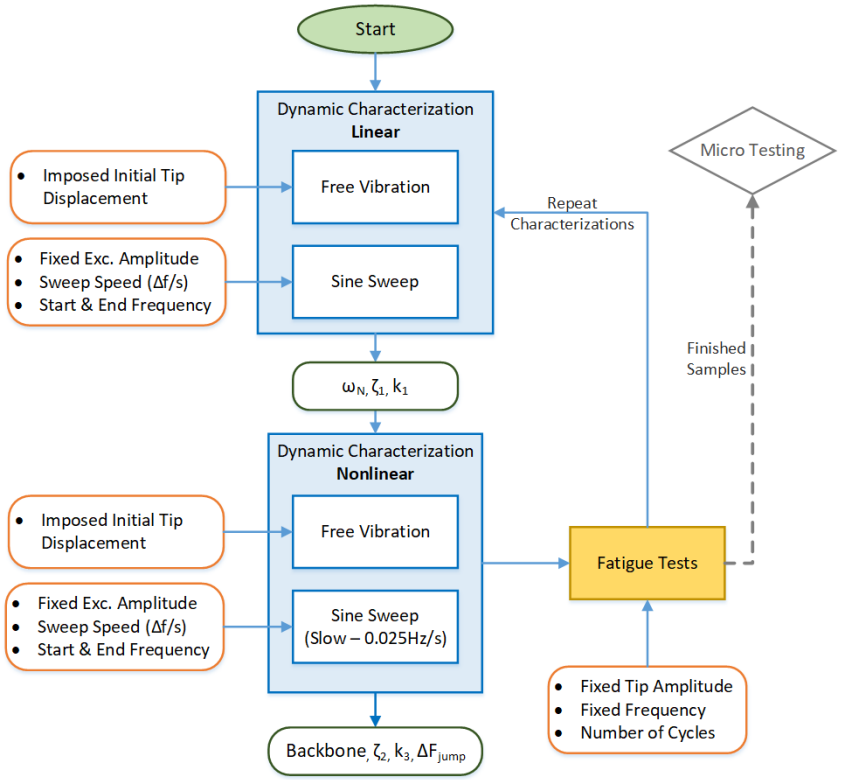

Figure 3.3: Schematic depiction of the testing strategy with relevant inputs and outputs.

3.2.1 Linear Characterization

Linear characterizations are performed to obtain the linear coefficients (natural frequency and viscous damping) of the underlying linear system. As explained in section 1.1, linear characterizations are the general method for SHM techniques. This will also enable the comparison between results obtained from linear analysis and nonlinear analysis. Within the current work, the linear region is defined for tip displacement amplitudes of less than 1% of the beam length (decided after examination of the results).

Free Vibration

Free vibration testing is performed by imposing an initial displacement upon the beam, quickly releasing and waiting until it comes to a rest. This is repeated at least five times per beam per fatigue level. The nonlinear and linear responses are obtained from the same tests. This testing method is important for the quantification of the linear damping coefficients (c_1).

Sine-sweep Excitation

This test phase consists of sine-sweep excitations, which are performed at low response amplitudes (≈ 1mm). Forward and backward sine-sweep testing is conducted in the linear region and the time data is collected. The sweeps are performed at relatively fast speeds (compared to the nonlinear sweeps) and the frequency range is chosen to cover the first three vibrational modes.

3.2.2 Nonlinear Characterization

After performing the linear characterizations, nonlinear experimental characterizations are conducted. In order to generate a nonlinear beam response, high amplitude excitations are required. This entails tip responses greater than 1% of the beam length.

Free Vibration

This is performed the same way as for the linear characterization, but the initial displacement is of a higher magnitude. From these measurements backbone curves and damping skeletons can also be obtained by employing signal processing techniques. This will be further explained in section 3.6.

Slow Sine-sweep Excitation

These experiments include forward and backward sweeps. The excitation frequency is varied with a constant rate between two frequency values around the nonlinear resonant frequency. The sweep speed is kept very low (0.025 Hz/s). With a sweep speed this low the response is highly similar to a stepped sine exctitation, which is steady-state for each increment. This way HBM can be applied to model this experimental response, as it approximates steady state responses. The slow sweep speed also enables the proper capturing of jump phenomena. Similar experimental methods were performed by Haynes et al. [11], Lu et al. [64] and Dossogne et al. [8], in which they showed this excitation method effective for characterizing nonlinear dynamic behaviour of metal beams.

3.2.3 Fatigue Testing

After having performed the free vibration and sine-sweep tests, fatigue testing is performed. This entails applying an excitation of a fixed force and fixed frequency for specific periods of time in order to impose certain levels of fatigue damage to the specimens. The excitation frequency used is near the natural frequency ω_n (≈ 0.5 Hz lower) of the system. To obtain multiple increments of fatigue infliction, each fatigue period is first chosen to be 10 minutes. Based on the S-N curve of Aluminum 7075-T6 an excitation force is chosen that results in a stress associated with the desired degradation rate. After each fatigue test the beams go trough the complete testing process again until complete fatigue is reached. This is defined to be when the crack has grown to approximately half of the beam width.

3.3 FEM Analyses

Prior to performing tests, several estimations are performed to obtain certain necessary testing parameters. For this reason, analyses are performed using Finite Element Method (FEM) in Abaqus

software. This includes a static stress analysis and a modal analysis. Hereby sensitivity analyses were also performed to ensure enough elements were used.

3.3.1 Static Stress Analysis

A stress analysis is performed to correlate certain tip displacement magnitudes with local stresses. In combination with the S-N curves (Figure 3.1) the fatigue life can be roughly estimated. The estimation will provide an indication of the necessary parameters to be used with the sine-sweep, free vibration and fatigue testing. Deflection amplitudes are chosen, in such a way that the stresses do not exceed the yield strength. A test sample is modeled in ABAQUS using quadratic quadrilateral elements. At the fixture the sample is fixed and at the beam tip various initial deflections are imposed. Figure 3.4 depicts the model in its deflected state. The stresses in the x-direction (parallel to the beam length) are shown as well. Bending of the beam causes the largest stresses in this direction. The region with the highest stress is near the beam root (clamped end).

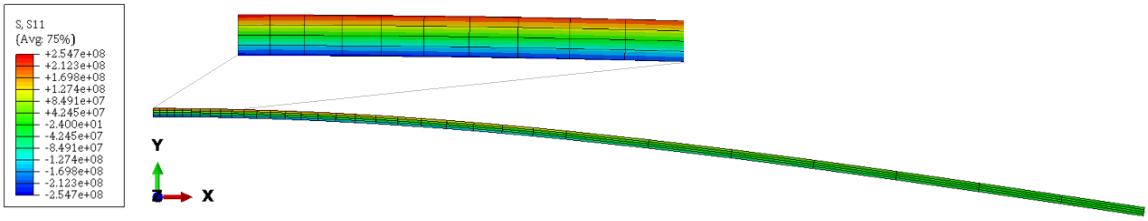

Figure 3.4: Maximum stresses occurring during a tip deflection of 28 mm for a beam length of 120mm.

3.3.2 Modal Analysis

Modal analysis is performed to obtain the natural frequencies and mode shapes of the system. This enables the assurance that the natural frequencies are sufficiently spaced out from each other and gives insight into the necessary excitation frequency ranges for the sine-sweep tests. Figure 3.5 shows the first three mode shapes of the test subjects. The corresponding frequencies for the first five modes are provided in Table 3.2.

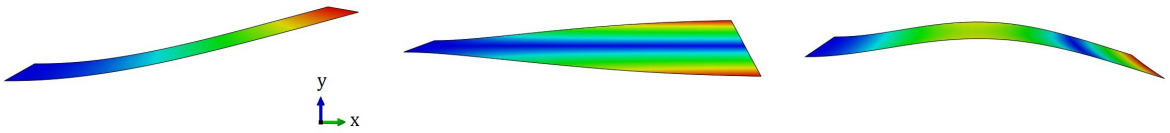

(a) Mode 1: Bending (b) Mode 2: Twisting (c) Mode 3: Bending

Figure 3.5: First three mode shapes of test subject

	Mode 1	**Mode 2**	**Mode 3**	**Mode 4**	**Mode 5**
Type	Bend	Twist	Bend	Twist	Bend
Natural Frequency (Hz)	58.3	289	363	926	1023
Natural Frequency (ω_i/ω_1)	1	4.96	6.23	15.88	17.5
Relative error with analytical (%)	2.62%	-	2.37%	-	2.44%

Table 3.2: Natural frequencies of test samples with the relative error

3.4 Testing Procedure and Parameters

Testing Parameters

An overview off all testing parameters is provided in Table 3.3. Hereby f_{R1} and f_{R3} denote the experimentally obtained (nonlinear) resonant frequencies for mode 1 and mode 3 respectively.

Test type	**Start freq. (Hz)**	**End freq. (Hz)**	**Sweep speed (Hz/s)**	**Sampling freq. (Hz)**	**Time per test (s)**
Linear sweep	10	450	10	3125	44
NL Forward (Mode 1)	$f_{R1}-2$	$f_{R1}+2$	0.025	3125	160
NL Backward (Mode 1)	$f_{R1}+2$	$f_{R1}-2$	0.025	3125	160
NL Forward (Mode 3)	$f_{R3}-2$	$f_{R3}+2$	0.025	3125	160
NL Backward (Mode 3)	$f_{R3}+2$	$f_{R3}-2$	0.025	3125	160
Free Vibration	N/A	N/A	N/A	3125	64
Fatigue	$f_{R1}-0.5$	$f_{R1}-0.5$	N/A	1000	600

Table 3.3: Testing parameters.

Testing Procedure

Test samples are securely clamped in a steel fixture which is attached to the shaker. To ensure the bolts have equal pressure distribution and the fixture is securely fastened, a calibrated torque wrench is used for the fastening. Each time the test is paused, the bolt tightness is checked again with the torque wrench to ensure proper boundary conditions. The clamping length is measured and it is ensured that the sensors and additional measurement devices are properly fastened and connected. The generation of excitation signals and data acquisition is performed using the Polytec workstation and software suite. The measurements from the laser vibrometer, the accelerometer and reference voltage are collected. The time data with values for each sensor measurement is saved along with the time value at each sampling interval. Thereafter the data is exported in ASCII format, which is accessed within MATLAB for further processing.

3.5 Static Deflection Experiment

To gain greater insight into the static stiffness over different measures of beam tip deflection, a static deflection experiment is performed. The underlying theory is first explained.

3.5.1 Static Bending Theory

Nonlinear springs show a force-deflection relation according to Equation 3.1 [100]. Hereby k_{1s} denotes the linear stiffness and k_{3s} the cubic stiffness.

$$F_s = k_{1s} v + k_{3s} v^3 \tag{3.1}$$

The effective static stiffness can thus be expressed as:

$$k_{ES} = \frac{F_s}{v} = k_{1s} + k_{3s} v^2 \tag{3.2}$$

It should be noted, however, that the static stiffness is not of the same value as the dynamic stiffness of the first mode. This is mainly due to the fact that part of the energy goes to higher modes of vibration. Considering the linear regime, the dynamic stiffness and static stiffness are closely related. In fact the static stiffness is near identical to the first mode dynamic stiffness [101]. In the linear regime the static stiffness can be represented by the equation as derived from standard Euler-bernouilli beam theory. This is achieved by first obtaining the deflection formula for a end-loaded cantilever beam, given by:

$$v(x) = \frac{Fx^2}{6EI}(3L - x) \tag{3.3}$$

From Equation 3.3, the linear static stiffness at the beam tip ($x = L$) can be expressed as:

$$k_{1s} = \frac{3EI}{L^3} \tag{3.4}$$

The effective mass (modal mass) can be expressed by m_1 from Equation 2.27, with Ψ now normalized to equal 1 at $x = L$, denoted by $\hat{\Psi}$ [101]. The expression and subsequent computation become:

$$m_{1m} = m_s \int_0^L \hat{\Psi}(x)^2 \, \mathrm{d}x = \frac{m_s L}{4} \tag{3.5}$$

By using Equation 2.35, 3.4 and 3.5, the ratio of the linear modal stiffness of the fundamental mode (k_{1m}) to the linear static stiffness (k_{1s}) can be determined:

$$\frac{k_{1m}}{k_{1s}} = \omega_{1m}^2 \cdot m_{1m} \cdot \frac{1}{k_{1s}} = (\beta_1 L)^4 \frac{EI}{m_s L^4} \cdot \frac{m_s L}{4} \cdot \frac{L^3}{3EI} = \frac{(\beta_1 L)^4}{12} \approx 1.03 \tag{3.6}$$

This result agrees with the statement that the modal stiffness of the fundamental mode is very close to the static stiffness for the studied case.

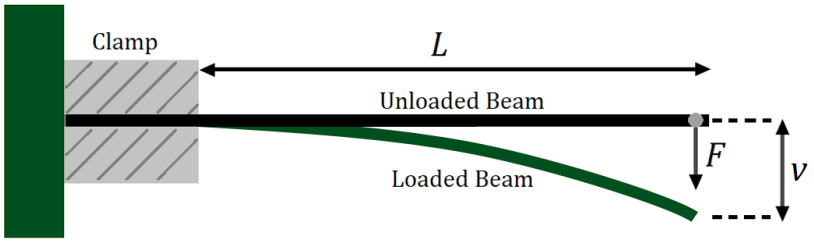

Figure 3.6: Setup of the static deflection test.

3.5.2 The Experiment

During the experiment a beam sample is tightly clamped at the base and gradually loaded with weights. The test set-up is visualized in Figure 3.6. Deflection is measured using a vernier height caliper after the addition of each weight. The test is performed three times with beams of slightly different lengths.

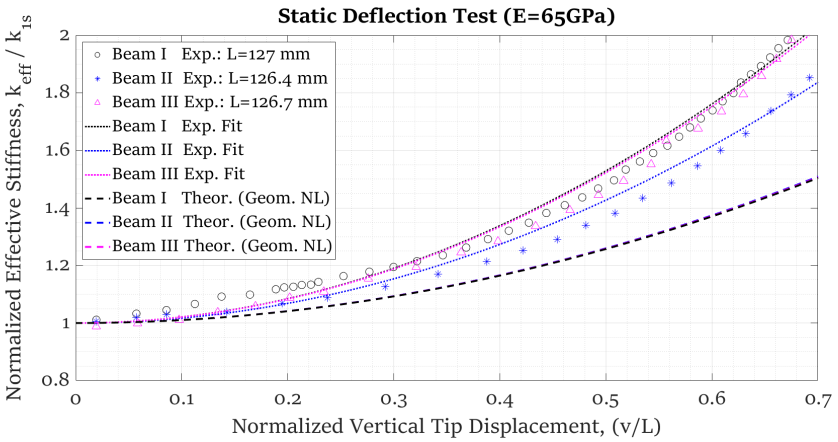

Figure 3.7: Resulting normalized effective stiffness from the deflection test using E=65GPa

Figure 3.7 depicts the results obtained from the experiment. The effective stiffness is normalized by k_{1s}, to clearly show the deviation of linear behavior. The results show that the stiffness is well approximated as a cubic nonlinearity, which is justified by good agreement using a curve fit in form of Equation 3.2. It is also relevant to know that at a vertical deflection of $0.75L$, the effective stiffness is approximately twice as large in value compared to the original (linear) static bending stiffness, k_{1S}. The effect of the nonlinear geometric nonlinearity as defined in the analytical approach is also included in Figure 3.7. Hereby k_3 is calculated in Equation 2.27 using the deflection formula in Equation 3.3. The results show that at large ampltudes, this underpredicts the effective stiffness. Figure 3.8 gives a visual explanation of this underestimation of the nonlinear static stiffness. As the deflection increases, part of the force gets compensated by the axial rigidity and pure bending is no longer an accurate assumption. The exact relationship between the nonlinear static and nonlinear dynamic stiffness given the relevant loading conditions is unknown.

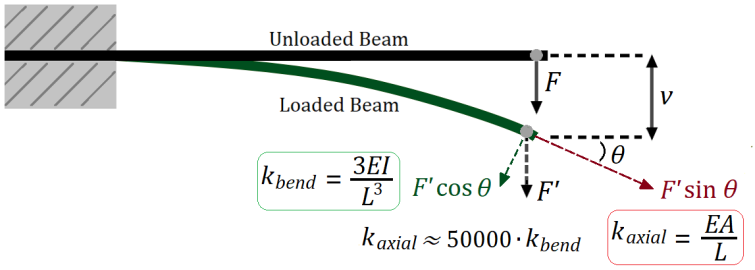

Figure 3.8: Bending stiffness transitions into axial stiffness at high displacements

3.6 Data Processing

The data processing (signal processing) strategy used for converting the experimentally obtained data into proficient results is detailed within the current section. The section is divided into the processing of the free vibration tests (subsection 3.6.1) and the sine-sweep tests (subsection 3.6.2). All collected experimental data is processed using MATLAB software.

3.6.1 Free Vibration Processing

The free vibration data files contain measurements of tip responses as an effect of imposing an initial displacement. Per measurement at least five free vibrations are imposed, with each one starting in the nonlinear region of displacement. The linear parameters are obtained from the same measurements by using the data starting at low amplitudes (< 1% of the beam length). The MATLAB code created for processing free vibration data is provided in Appendix B. The processing steps are explained in the following.

Subtract Base Velocity

The beam tip response measured by the laser vibrometer is recorded in terms of the absolute velocity. As the response velocity relative to the base velocity is desired, the base velocity is subtracted from the tip response data. The base acceleration is measured by the accelerometer attached to the base fixture. The acceleration data is converted to velocity data by applying numerical cumulative trapezoidal integration (MATLAB `cumtrapz` function). A bandpass filter (Butterworth) was hereby applied to prevent data drifting and a moving average filter was applied to improve the accelerometer signal, which was not clean compared to the laser vibrometer signal.

Obtain Partitioned Displacement Data

The relative beam tip response is now obtained in terms of velocity. From this data, the tip displacement is obtained by integrating the signal, again via trapezoidal integration. For each fatigue level, each free vibration decay is first separated by using a peak identification function (MATLAB `findpeaks` function). An example of a tip displacement time signal with identified peaks is depicted in Figure 3.9a. Based on the minimum distance between peaks, a general time window is determined and the time data is partitioned to have 1 single free vibration in one window. The data is also sorted from high to low initial amplitude vibrations. The nonlinear and linear region are separated by applying a threshold for the tip displacement amplitude at 0.01L (1% of beam length) and the signals are split at that point. Peak envelopes are then created for the linear signal part in order to identify the linear damping magnitude. An example of partitioned and split up signals with fitted envelopes is depicted in Figure 3.9b.

Linear Damping Ratio (ζ_1) Estimation

The damping ratio (ζ_1) is generally obtained using methods such as the Logarithmic Decrement or the Half Power Method [102] [103]. In this work a method based on the logarithmic decrement is followed to estimate ζ_1. The displacement time signal of a free vibration can be expressed as:

$$v(t) = \alpha_0 e^{-\zeta_1 \omega_n t} \sin(\omega_d t + \phi); \quad t > 0 \tag{3.7}$$

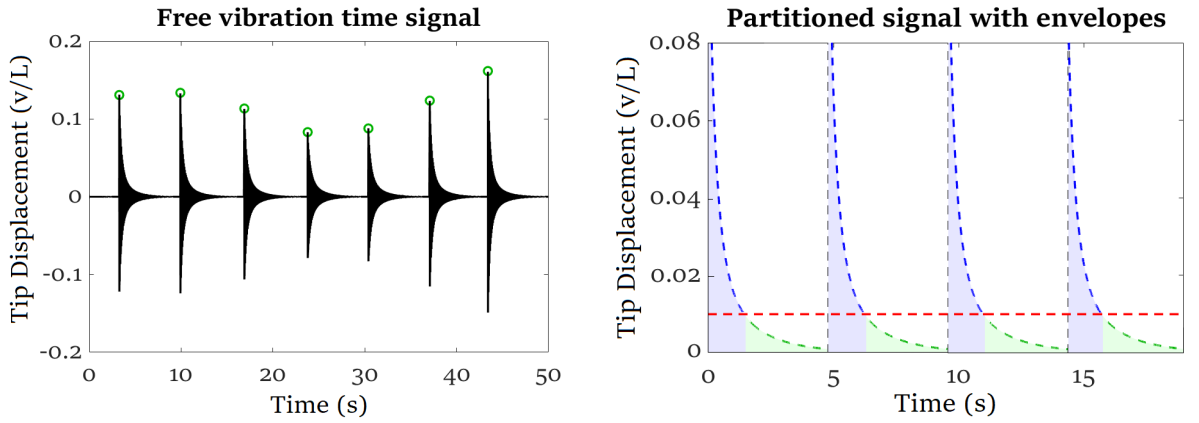

(a) Time signal of the tip displacement

(b) Partitioned and split data with peak envelopes

Figure 3.9: Experimental data processing methods (Free Vibration)

where α_0 is the initial maximum displacement amplitude and ω_d is the damped natural frequency ($\omega_d \approx \omega_n$ for small damping ratios). ζ_1 is related to the linear damping coefficient c_1 by:

$$c_1 = 2m_1\zeta_1\omega_n \quad \left(\text{for mass normalized EoM: } c_1 = 2\zeta_1\omega_n\right) \tag{3.8}$$

Considering only the peaks, the decay envelope for linear free vibration can be represented using the first part of Equation 3.7 ($\alpha(t) = \alpha_0 e^{-\zeta_1\omega_n t}$). By taking the natural logarithm of this expression, the following relationship is obtained:

$$\ln(\alpha(t)) = \ln(\alpha_0) - \omega_n\zeta_1 t; \quad t > 0 \tag{3.9}$$

Hence, the slope of the logarithmic decay envelope is equal to $-\omega_n\zeta_1$. To experimentally estimate the linear damping, a straight line is fitted over the logarithmic envelope, which should behave this way according to Equation 3.9. The value of the slope of this line allows the estimation of the linear damping ratio ζ_1. Hereby only results with a relatively low standard deviation over the different measurements are kept, due to high amounts of noise present in some of the cases (filtering techniques would not solve this issue). This process is visualized in Figure 3.10a. In the figure it also clearly evident that the logarithmic decay envelope of the nonlinear signal part is not linear.

Backbone Curves

Generally backbone curves are obtained by performing a series of sweep tests over different excitation levels and capturing each resonant frequency. In the current work free decay data is used for the estimation. By applying processing methods on the decay data, backbone curves can be obtained with better efficiency and accuracy. The backbone curves can be used to estimate the nonlinear parameters by fitting the experimental data to the equations derived from the Harmonic Balance analysis. Processing methods to estimate the backbone curves, as conducted by Londono et al. [10], are applied in the current work. This first requires the assessment of the instantaneous frequency and the decay envelope, which is explained in the following.

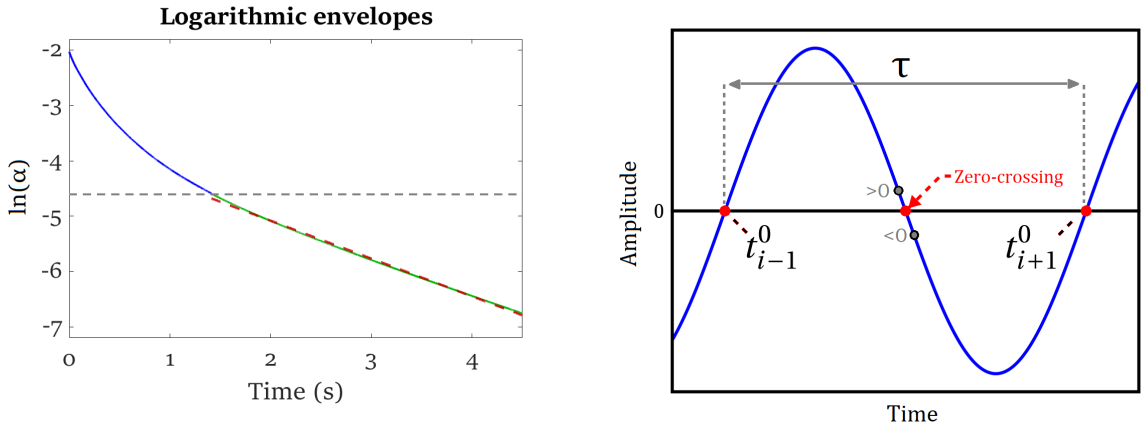

(a) Logarithmic envelopes

(b) Zero-crossing method

Figure 3.10: Experimental processing methods

Instantaneous Frequency Assessment

The zero-crossing method is used to estimate the instantaneous frequency. For every time the input signal crosses the x-axis in a downward manner, the two data points that capture this crossing are identified ($x_k > 0 \wedge x_{k+1} < 0$), as visualized in Figure 3.10b. By means of interpolation based on each pair of point amplitude values, the exact time at which the crossing of the horizontal axis occurs, is approximated. The periods between crossing points are then directly related to the frequency within that specific time period. The instantaneous frequency is thus expressed as [10]:

$$\hat{f}(t_i^0) = (t_{i+1}^0 - t_{i-1}^0)^{-1} \tag{3.10}$$

An additional process is necessary to smooth out imperfect predictions of Equation 3.10. A moving average (MA) filter is hereby proposed, which in spite of its simplicity, offers optimal reduction of random noise [10]. The final result delivers only the dominant frequency variation in the decaying signal. . This procedure assumes that the instantaneous frequency is not rapidly altered for sequential vibration periods. The filter order needs to be selected based on the magnitude of noise present in the signal. In this work the instantaneous frequencies are smoothed over 5 points, gave sufficient results while not negatively influencing the overall result values. An example of an instantaneous frequency estimation is depicted in Figure 3.11a.

Amplitude Envelope

The experimental decay envelope can be obtained by employing a peak envelope function in MATLAB. The envelopes are determined using spline interpolation over local maxima separated by at least a specified number of samples. This sample number is chosen such that slight immediate fluctuations in the decay envelope are not captured.

After having obtained the instantaneous frequencies and amplitude envelopes, the backbone curves and damping skeletons can be produced. The backbone curves are simply created by plotting each

instantaneous frequency data point, along with the corresponding magnitude of the amplitude envelope at that point. The processing and theory related to the damping skeletons are explained next.

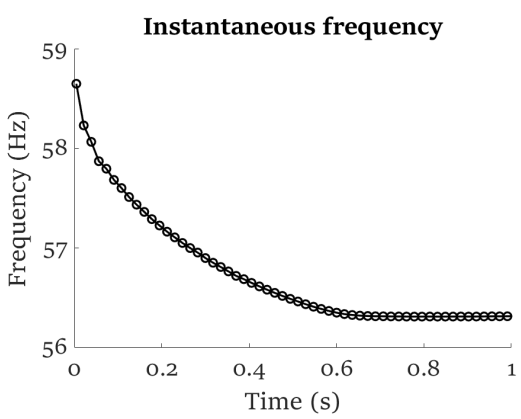

(a) Instantaneous frequency

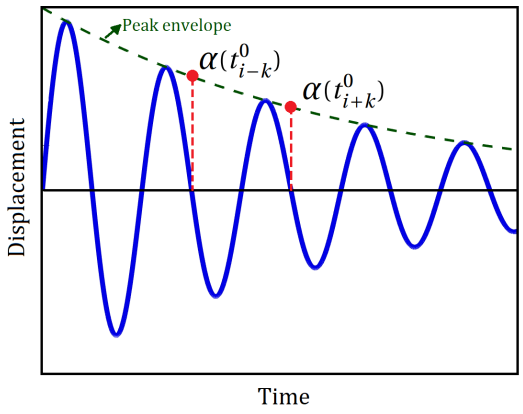

(b) Amplitude envelope depicting the method for obtaining the effective damping ratio, ζ_{eff} (visualized for $k = 1$).

Figure 3.11: Experimental processing methods

Damping Skeletons

A damping skeleton plots the effective damping ratio of the system versus the amplitude of vibration [10]. In this work the damping skeletons are used to analyze the nonlinear damping contribution. The method is based on the logarithmic decrement method, but in this case, applied for sequential increments within a single decay. An approach similar to Londono [10] is used to estimate the damping skeletons. However, in this work the effective damping ratio is estimated in a slightly different manner, by assuming the logarithmic decay envelope as a piece-wise linear function.

For the nonlinear signal, the same equation describing the decay of a viscous damper is used to express the amplitude envelope, but now ζ and ω_n are taken as variables instead of constants:

$$\alpha(t) = \alpha_{t-k} e^{-\zeta(t)\omega_0(t)\Delta t} \tag{3.11}$$

For each increment, the effective (linear) damping ratio is determined. Hence, based on Equation 3.11, the effective damping ratio at each zero-crossing can be determined using the following expression (similar to Equation 3.9):

$$\zeta_{eff}(t_i^0) = \frac{1}{\omega_0(t_i^0)\Delta t}\left(\ln(\alpha(t_{i-k}^0)) - \ln(\alpha(t_{i+k}^0))\right) \tag{3.12}$$

For clarity this is visualized in Figure 3.11b. The relationship between the effective damping ratio (ζ_{eff}) and effective damping coefficient (c_{eff}) is hereby defined as [10]:

$$c_{eff} = 2m\zeta_{eff}(t_i^0)\omega_0(t_i^0) \tag{3.13}$$

Equation 3.13 and Equation 2.53 (HBM) allow the following expression for the effective damping ratio in the following manner (substitute $c_2 = 2\zeta_2\omega_n$):

$$\zeta_{eff} = \zeta_1 + \frac{8\zeta_2\omega_n\alpha}{3\pi} \tag{3.14}$$

The estimation of the quadratic damping (c_2 or ζ_2) is performed using the damping skeletons. To obtain ζ_2, Equation 3.14 is matched to the experimental effective damping ratio by performing curve fitting (MATLAB Curve Fitting Toolbox) with ζ_1 fixed at the previously determined values. At this point in the analysis the linear (viscous) and nonlinear (quadratic) damping coefficients are both known.

Repeatability

Figure 3.12 provides an example of obtained backbone curves and damping skeletons. In this figure different colors represent different vibration decays for the pristine case. Evidently, the repeatability is fairly good. The plots also clearly show that the shape of the curve is not influenced by varying initial tip displacement amplitudes. Throughout all cases a similar level of repeatability was observed, although certain cases had a higher influence of noise.

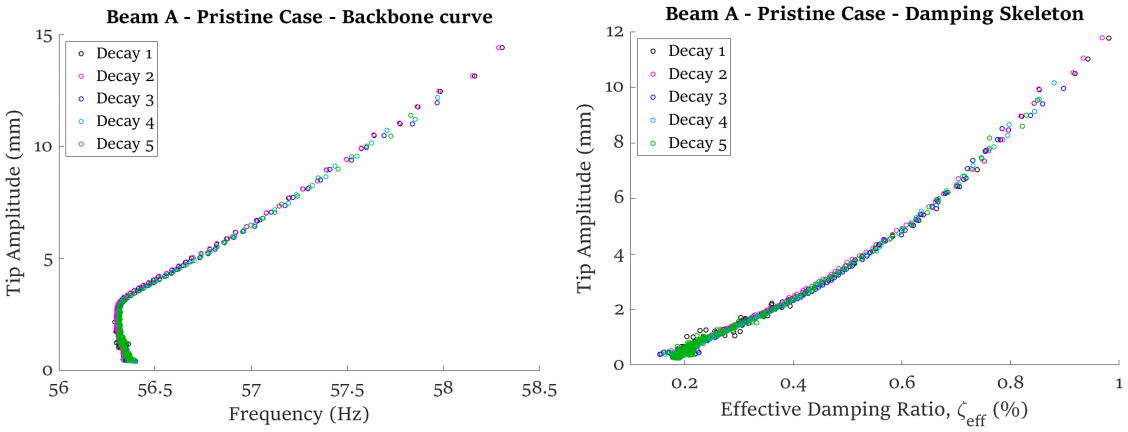

Figure 3.12: Example of experimental backbone curve and damping skeleton

3.6.2 Sine-sweep Processing

The collected data from the sine-sweep excitations include forward and backward sweeps performed in the linear and nonlinear region. The processing of this data is explained in the following.

Linear Sweeps

For the linear sweeps the data is processed by means of a Fast Fourier Transform (FFT) analysis. The linear natural frequencies are determined to serve as a baseline for the nonlinear results. The simple FFT procedure is depicted in Figure 3.13a, which shows that the response is in fact linear and the repeatability between the forward and backward sweeps is evident. The figure also shows that the frequency consistently decreases for increasing fatigue cycles.

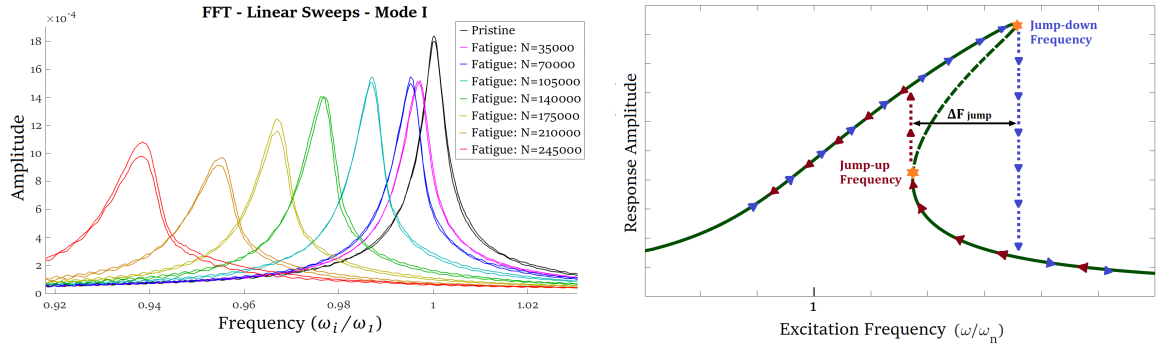

(a) FFTs performed for the linear sine-sweeps zoomed in on the first mode for various damage cases

(b) A nonlinear response of a cubic spring system which shows jump phenomena

Figure 3.13: FFT of linear sweeps and definition of ΔF_{jump}

Nonlinear Sweeps

The nonlinear sweeps are processed differently in order to capture the instabilities (jumps) and to represent the actual maximum amplitudes on the vertical axis of the plots. Firstly, integration is performed to obtain the tip and base signals in terms of displacement. This is achieved using the same computational methods as described in subsection 3.6.1. Subsequently, peak identification is performed on the absolute of the signal to capture all the data points where the amplitude is at a maximum. Hereby the minimum distance between peaks is chosen to be as small as possible, while not capturing signal peaks below the actual amplitude envelope. The time data is converted to the frequency domain by means of the zero-crossing method to assess the instantaneous frequency. This method is the same as the one described in the previous section (Equation 3.10), but this time performed on the input signal. Hereby the start frequency, the end frequency and the frequency rate of change (sweep speed) are determined and potential syncing errors (which were observed in the current case) due to hardware and software delay issues are compensated. A frequency vector is then created by fitting a linear line to the instantaneous frequency data and thus the time data is accurately converted to the frequency domain. Finally, the response displacement is divided by the base displacement to obtain the FRFs. Important parameters within this test type include ω_{jd} and ω_{ju}, which denote the jump down and jump up frequency respectively. The difference between the jump frequencies is hereby also of interest, which is denoted by ΔF_{jump}. Jump phenomena and ΔF_{jump} are visualized in Figure 3.13b.

Supplementary information regarding the experimental approach is provided in Appendix D.

CHAPTER 4

Results and Discussion

In this chapter the obtained results are provided and critically discussed. Firstly, the experimental results are provided in section 4.1. Subsequently, the results obtained through the analytical approach are detailed in section 4.2. Finally, the results are compared and discussed in section 4.3.

Procedure for nonlinear system identification

At this phase of the research, a procedure is followed by combining the experimental and analytical aspects in order to successfully achieve the identification of nonlinear system coefficients. This procedure is depicted in Figure 4.1 and serves as a guide for this chapter. The visualization shows the method for obtaining the various coefficients and graphs. It also shows the necessary conditions to successfully achieve and verify physics-based identification of the nonlinear system. Although tests were also performed for higher modes, only results for the first mode are considered in this work.

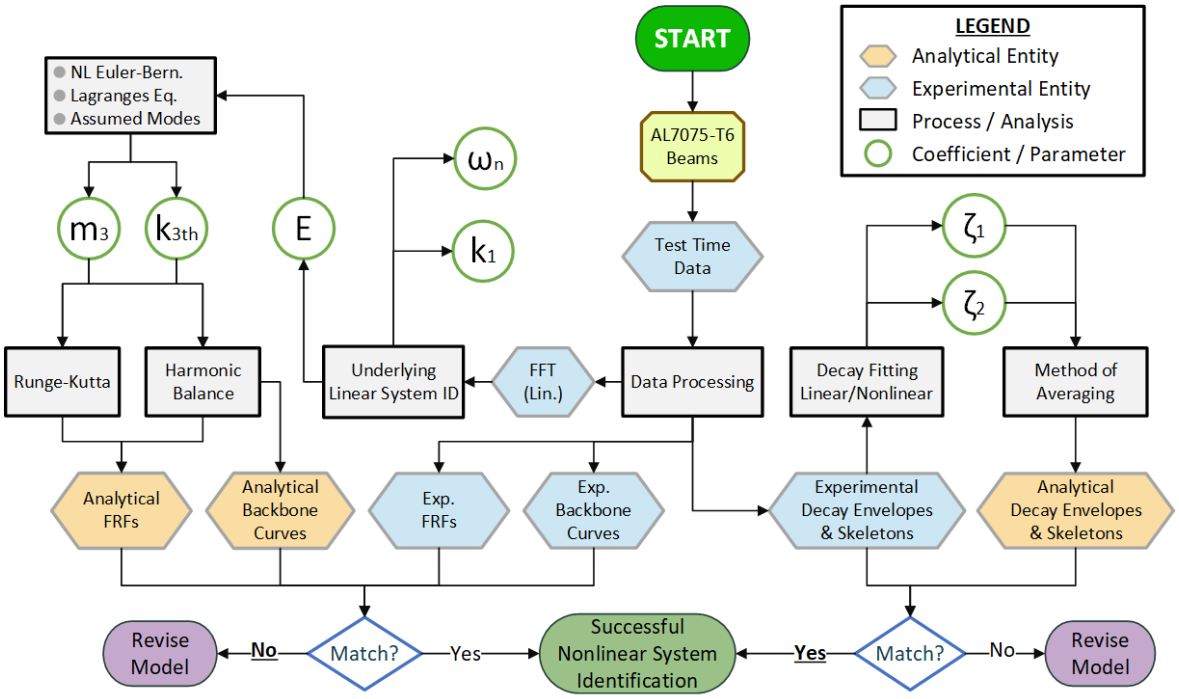

Figure 4.1: Procedure employed for nonlinear system identification

4.1 Experimental Results

The results obtained for three beams are provided in this work, which are named 'Beam A', 'Beam B' and 'Beam C'. Table 4.1 lists the details of the beams and the fatigue testing specifications.

Beam	Fatigue Periods	Fatigue Cycles per Period (≈)	Free Length (mm)	Prist. Exp. F_{nat} (Hz)	Avg. Fatigue Stress (MPa)
A	7	35000	115.5	56.4	174.8
B	5	35000	114	57.8	183.4
C	3	35000	115	56.8	195.9

Table 4.1: Fatigue testing parameters.

4.1.1 Free Vibration Results

Backbone Curves

The backbone curves obtained for all beams are depicted in Figure 4.2. For further insight into the repeatability of all backbone curves, refer to Appendix C. Additionally, the same backbone curves zoomed into the linear amplitude region are depicted in Figure 4.3a. In all these figures, the colored dashed vertical lines represent the (linear) natural frequencies obtained from the linear sine-sweeps. For the backbone curves zoomed into the linear region, a (heavy) Gaussian filter is applied to make the results more presentable. This additional filter was necessary to remove noise originating from the amplifier, which was left on during some of the tests. Hence Figure 4.3a serves more as an indicative result. The effect of the noise is mostly present at low amplitudes, but at high amplitudes it becomes negligible. In the linear region, it is evident that the frequency stays nearly constant and is approximately equal to the natural frequency from the linear sine-sweeps (dashed lines). Considering the backbone curves of the whole amplitude range (Figure 4.2), significant nonlinear behavior is observed. At high amplitudes, significant deviation from the natural frequency is present.

Three interesting occurrences are witnessed in the backbone curves (Figure 4.2):

- For each curve there is a noticeable amplitude point at which the hardening starts to occur. The amplitude of this point seems to drop for increasing fatigue cycles.
- The shape of the curves become more complex for increasing fatigue cycles. Two additional inflection points appear. In pristine cases and early fatigue cycles, the shape is almost coincident with a bilinear line, but in later stages of fatigue life the dynamics become more rich.
- At amplitudes around $0.015L$, slight softening is present at later fatigue stages. This is attributed to changes in the material stiffness, as it was ensured that the boundary conditions were kept consistent by continually checking the torque of the bolts.

These three witnessed phenomena are speculated to be attributed to crack occurrence and other DP-related material changes. With the current experimental approach it is not possible to say to what extent damage precursors or crack occurrences have contributed to these effects.

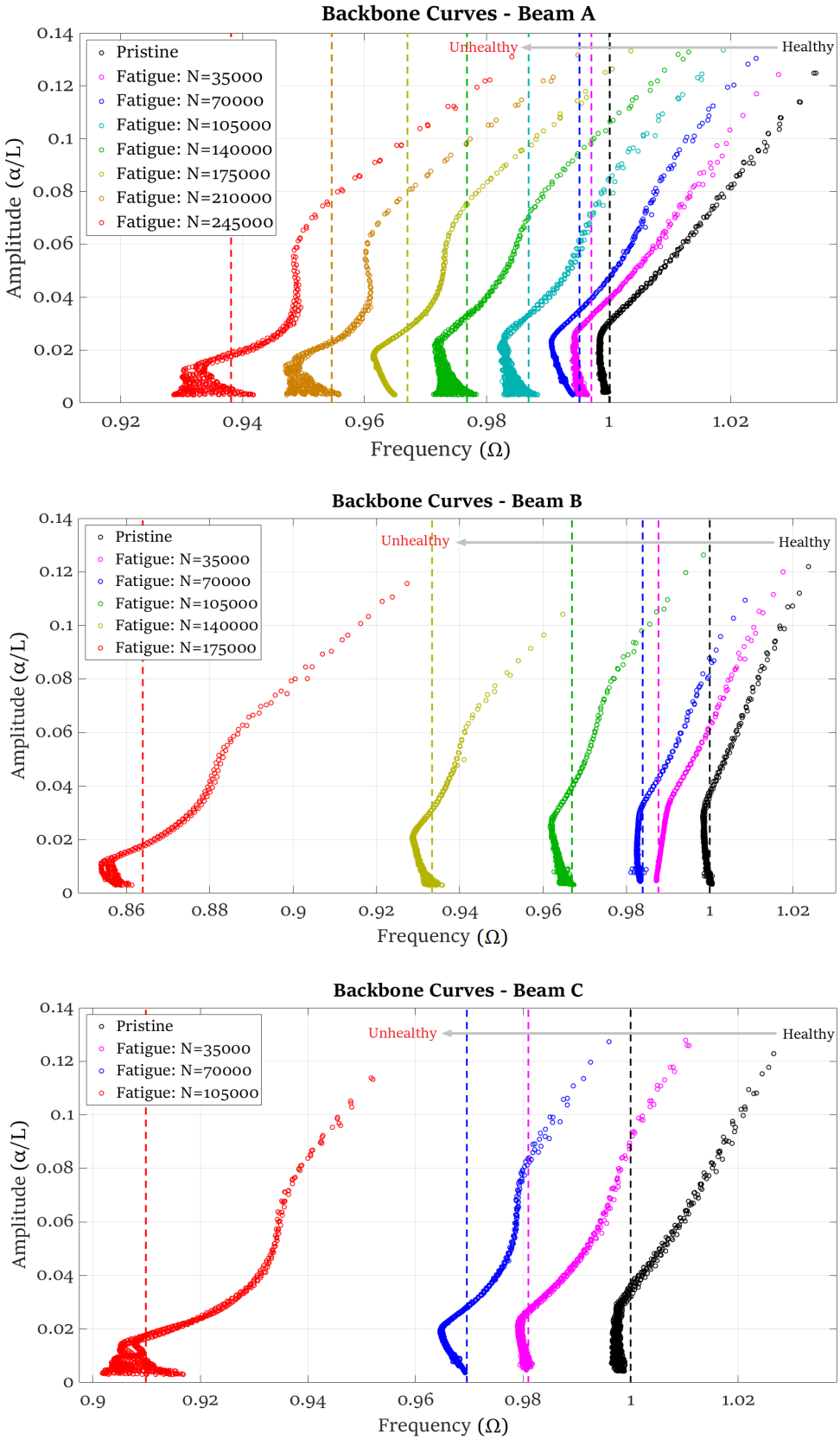

Figure 4.2: Backbone curves obtained for all three beams over different fatigue cycles

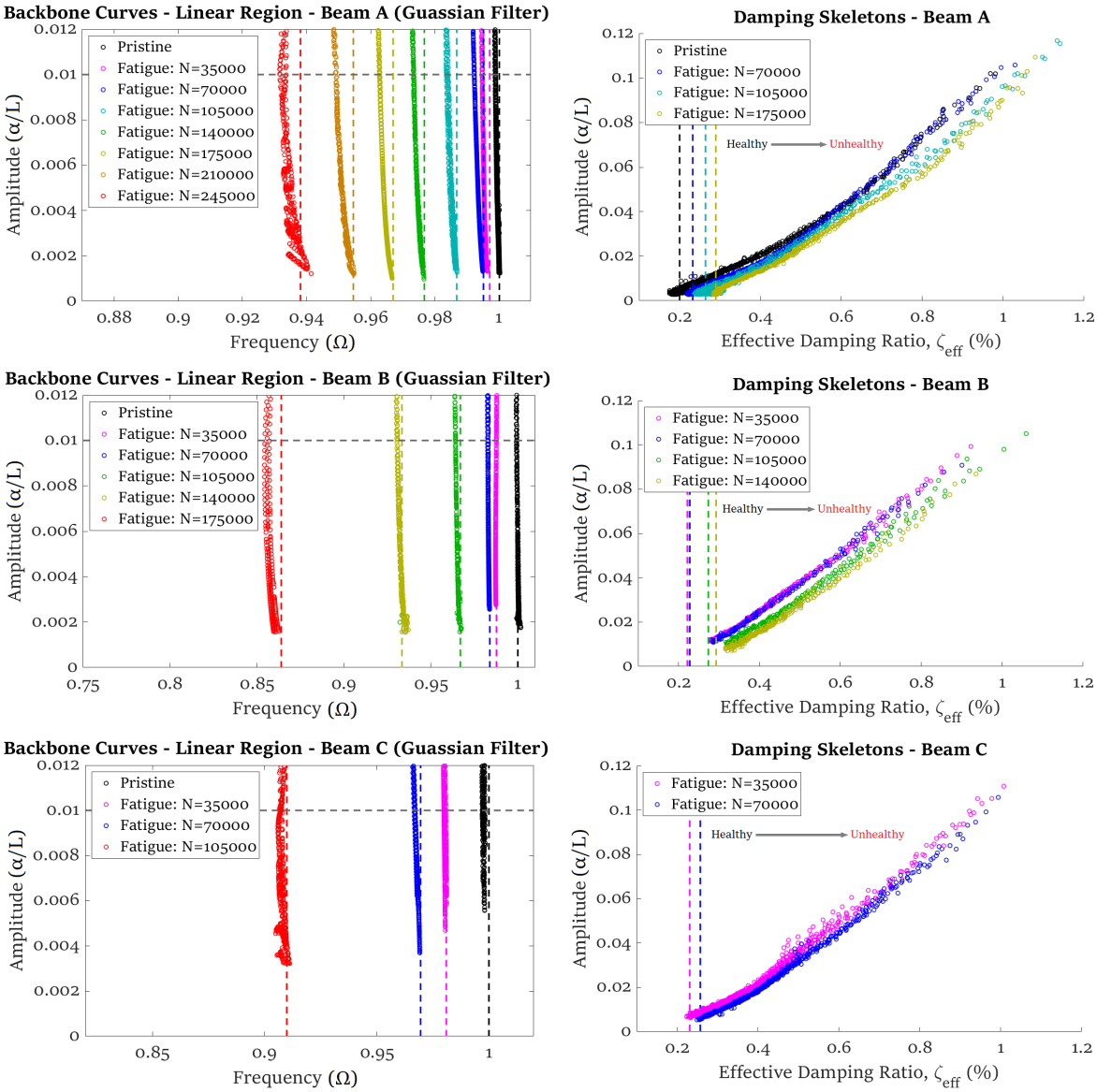

(a) Filtered backbone curves (linear region).

(b) Damping skeletons.

Figure 4.3: (a) Backbone curves filtered and zoomed into the linear region and (b) Damping skeletons.

Damping Skeletons

The obtained damping skeletons are depicted in Figure 4.3b. These curves show the effective damping ratio as a function of the amplitude of vibration by assuming piecewise logarithmic decay. In these figures the dashed lines indicate the viscous damping ratio, ζ_1 (of the linear signal). Due to excessive noise (damping estimation was extremely sensitive to noise) in some of the measurements, the damping skeletons were not constructed for all cases. From the obtained damping skeletons it appears that the effective damping ratio is approximately equal to the viscous damping ratio at low amplitudes. However, the effective damping ratio appears to increase in a nearly linear fashion as the amplitude increases. Various coefficients and metrics obtained from the backbone curves and damping skeletons are detailed in the following.

Nonlinear Coefficients and Other Metrics

Using Equation 3.14, ζ_2 is obtained from the damping skeletons by performing curve fitting with ζ_1 fixed at the obtained value. The obtained values for ζ_1 and ζ_2 are plotted in Figure 4.4 and provided in Table A.1. Upon examination of Figure 4.4a, it was observed that the linear damping (ζ_1) consistently increased for accumulating fatigue cycles. This could be caused by increased dissipation due to the occurrence of cracks and other micro-structural changes. In the literature viscous damping ratio's (ζ_1) for aluminum cantilever beams have been reported at 0.35% [104]. The quadratic damping, depicted in Figure 4.4b, does not appear to change substantially over fatigue cycles. No clear pattern of change was observed, which is in line with expectations. The quadratic damping is mainly attributed to the air drag force, which is a function of beam geometry, beam orientation and velocity. Because these parameters stay the same, it is logical that the quadratic damping stays (nearly) constant over different fatigue cycles.

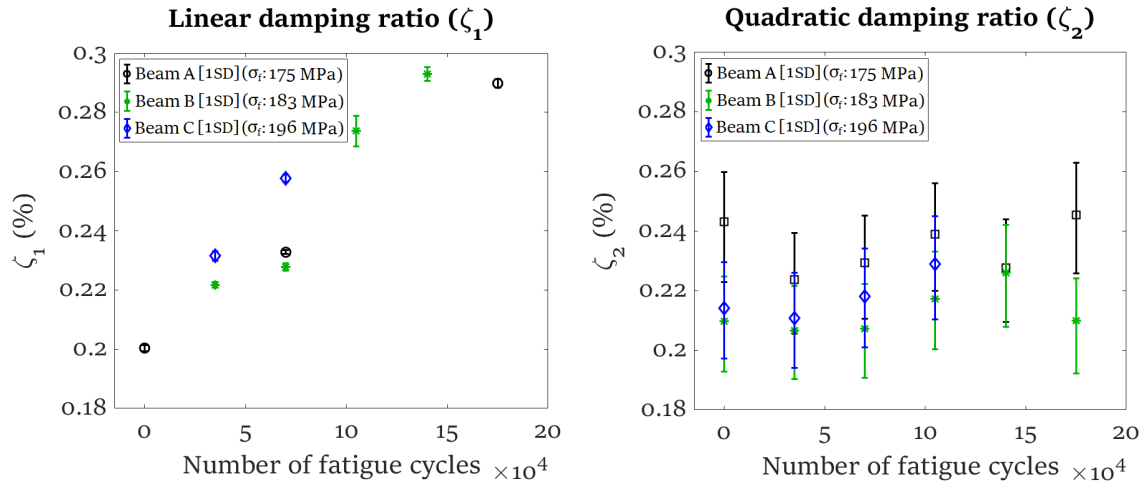

(a) Linear damping

(b) Quadratic damping

Figure 4.4: Linear and quadratic damping ratios

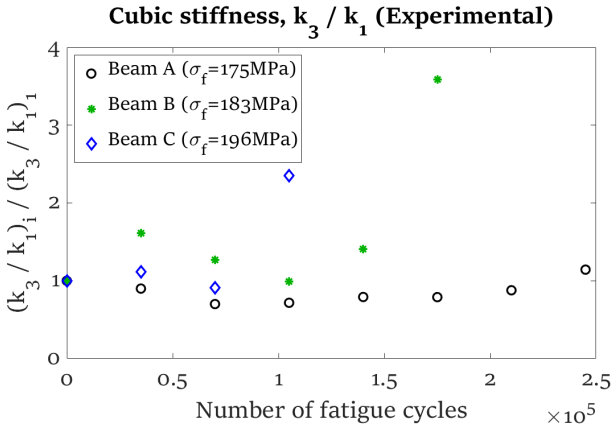

Figure 4.5: Values for cubic stiffness obtained from curve fitting

From this point in the analysis, a distinction is made between k_3 from the structural (analytical)

model, now called k_{3th} (theoretical cubic stiffness), and k_3 obtained through curve fitting Equation 2.62 with the experimental backbones, simply denoted by k_3. The nonlinear stiffness (k_3) is obtained through curve fitting Equation 2.62 to the experimental data. Obtained k_3 values are shown in Figure 4.5 and the specific values are provided in Table A.1. No clear pattern of change was observed for this parameter. The accuracy of this coefficient estimation is not ideal, because the curve fits had insufficient goodness of fit measures (avg. R^2=0.90). Experimental values for k_3 are used instead of the values calculated from the analytical model (k_{3th}), because of a severe underestimation of this coefficient through the model, which is further explained in section 4.3. The theoretical values for m_3 are hereby assumed to be correct. Table 4.2 gives an overview of theoretical and experimental coefficients.

Beam	$k_1(\times 10^5)$	$k_{1th}(\times 10^5)$	$m_3(\times 10^4)$	$k_3(\times 10^{10})$	$k_{3th}(\times 10^{10})$
A	1.26	1.26	2.13	1.87	0.191
B	1.32	1.33	2.22	1.32	0.21
C	1.27	1.28	2.16	1.51	0.197

Table 4.2: Theoretical and experimental coefficient values for the pristine cases (using E=61GPa).

Aside from the k_3 coefficient, other ways of quantifying the changes in shape of the backbone curves, are explored. An interpretative dissection of the backbone curves is depicted in Figure 4.6. Within this figure: (i) inflection points are identified, (ii) based on these points four regions are identified, (iii) slopes of different sections are considered. This analysis is mainly qualitative, but two features are hereby quantified. The quantified parameters are the amplitude of the first bending point, called bending point amplitude (BPA), and the instantaneous slope upward of this bending point, called the bending point slope (BPS). These metrics are correlated to fatigue life and depicted in Figure 4.7. Both metrics show a consistent and considerable drop of magnitude. The other inflection points (IP1 and IP2) and the slope between them also show consistent changes, however these are not quantified.

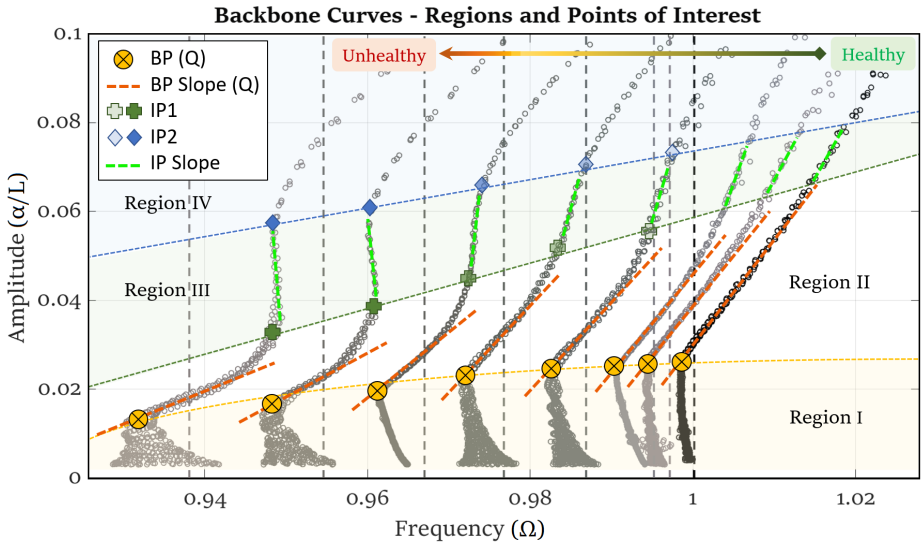

Figure 4.6: Dissection of the backbone curves showing identified regions and points of interest.

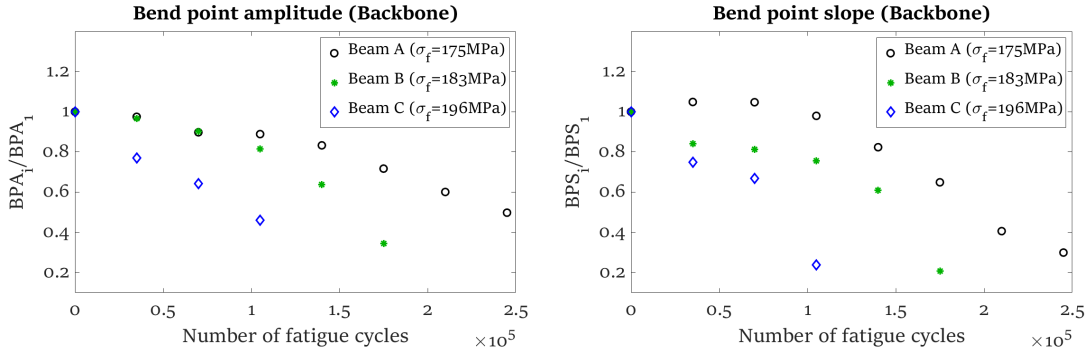

(a) Amplitude of bending point

(b) Slope upward of bending point

Figure 4.7: Secondary damage features from the backbone curves (semi-quantitative)

4.1.2 Sine-sweep Results

The evolution of the natural frequencies obtained from the linear sine-sweeps (FFT) is shown in Figure 4.8a. The results from the forward and backward slow sine-sweeps, after applying the processing techniques, are depicted in Figure 4.9. The y-axis represents the displacement amplitude of the tip (response) divided by the displacement amplitude of the base (input). The average acceleration at the base is also provided in the plots (grey labels), because this was not exactly constant for all measurements, as was aimed for. The metrics obtained using these results are provided in Table A.1 (Appendix A). These include the nonlinear resonant frequency (F_{RS}) and the difference between the jump-down and jump-up frequencies (ΔF_{jump}). The maximum amplitudes are hereby not considered as viable metric, because of the aforementioned undesired variability in excitation amplitude. It is evident that the nonlinear resonant frequency decreases as the fatigue cycles increase, which is expected because it is based on the linear natural frequency, which also decreases. Of interest, is the observed increase in the difference between the jump-up and jump-down frequencies (ΔF_{jump}). The evolution of ΔF_{jump} is visualized in Figure 4.8b. It is unknown at which point in time significant cracks occurred.

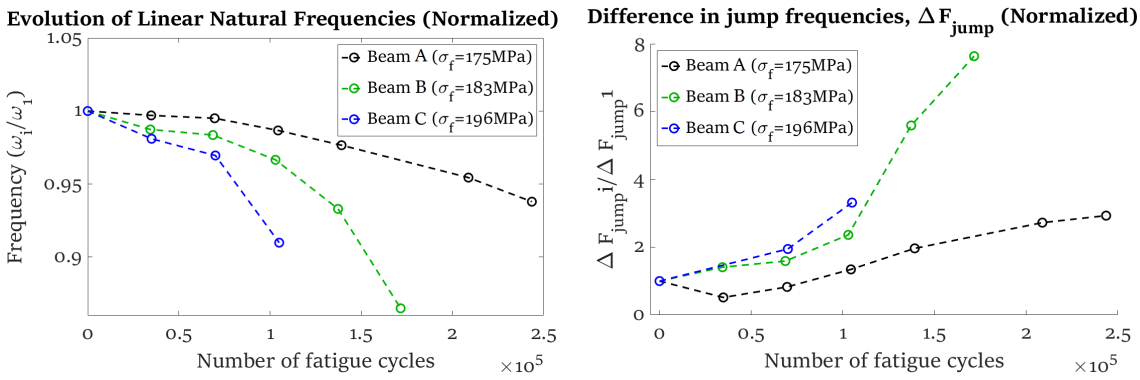

(a) Natural frequencies (Linear)

(b) Difference in jump up and jump down frequencies

Figure 4.8: Natural frequencies and difference in jump frequencies

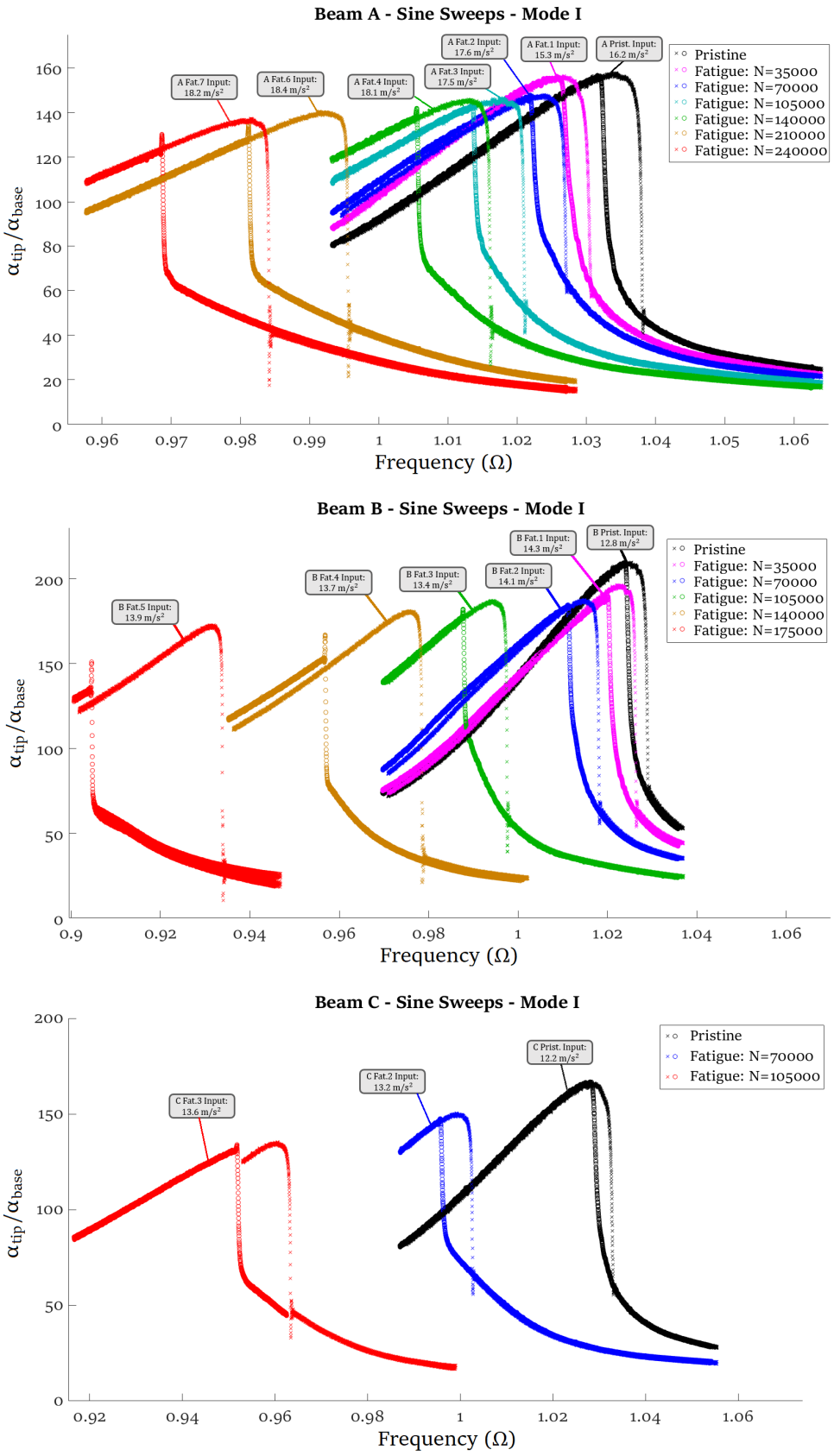

Figure 4.9: Results of the forward and backward sweeps of all beams over different fatigue cycles

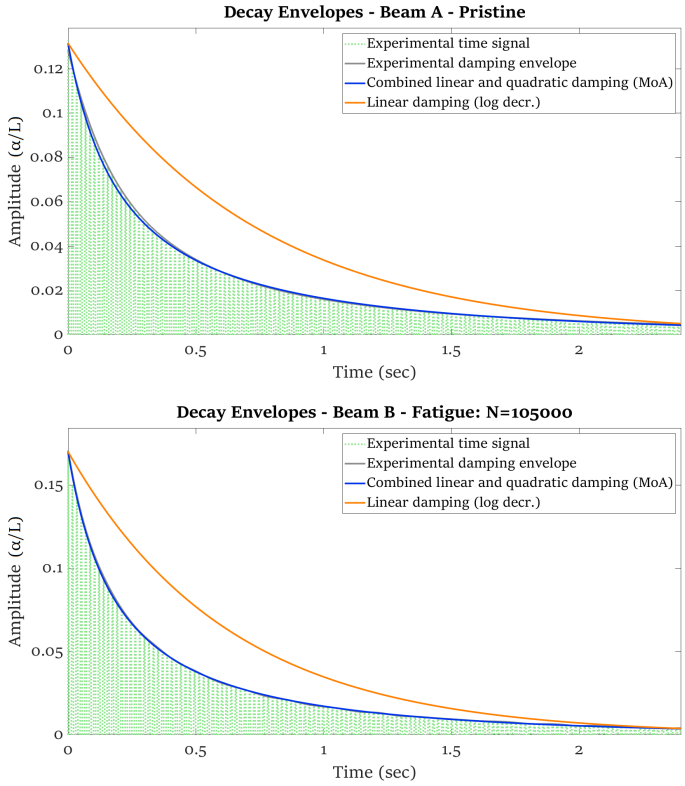

Figure 4.10: Nonlinear decay envelopes of two cases

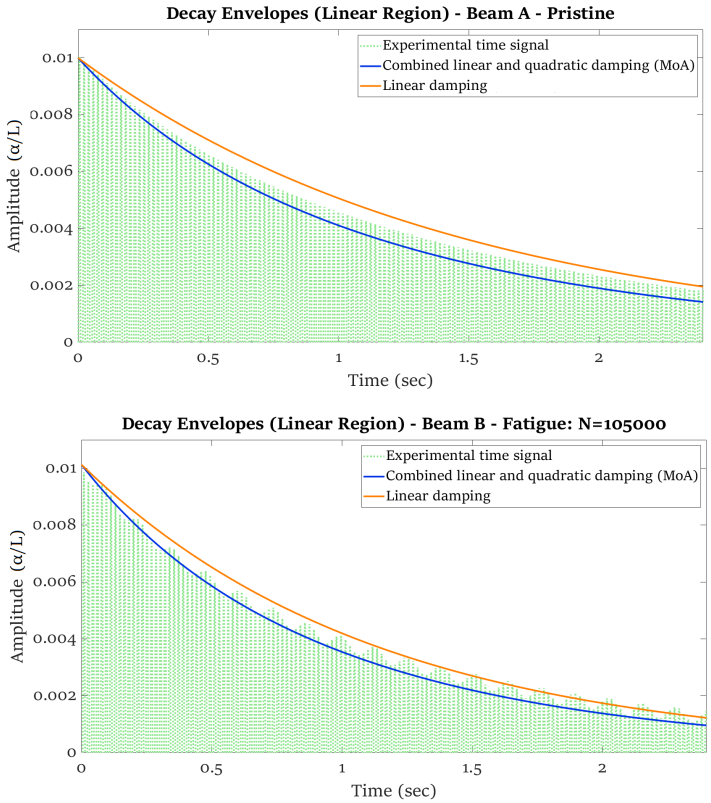

Figure 4.11: Linear decay envelopes of two cases

4.2 Analytical Results

Decay Envelopes (Method of Averaging)

The derived analytical equation to plot the decay of combined linear and quadratic damped system (Equation 2.81), is now applied. The experimentally obtained linear (ζ_1) and nonlinear (ζ_2) damping ratios, which were specified in Table A.1, are used as input parameters to plot the decay. Two arbitrary cases are chosen to display the results: Beam A in pristine condition and Beam B fatigued at 105000 cycles. The resulting envelopes for decays in the nonlinear and linear range are depicted in Figures 4.10 and 4.11. Considering the decay starting at high amplitude values (Figure 4.10), it is remarkable that the analytical envelope with combined linear and quadratic damping is almost indistinguishable from the experimental signal envelope. In these same cases it is evident that a solely linear decay model (standard logarithmic decrement) does not even remotely model the path of the actual decay. Now, upon examination of the decays originating from an amplitude in the linear range equal to $0.01L$ (Figure 4.10), it can be stated that both damping models are fairly accurate in estimating the decay. In this amplitude range the decay is in fact well approximated by a pure exponential decay (viscous linear damper). These results indicate that the obtained values for ζ_1 and ζ_2 are accurate.

Harmonic Balance and ODE45

In Figure 4.12 nonlinear FRFs are plotted using HBM and RK (ODE45). The results of the two methods agree very well with each other. The fact that these results match also gives greater confidence in the correctness of the derived equivalent equations from HBM used for curve fitting. One aspect where the models differ is the additional range HBM extends to, which could give greater insight into jump phenomena (instabilities).

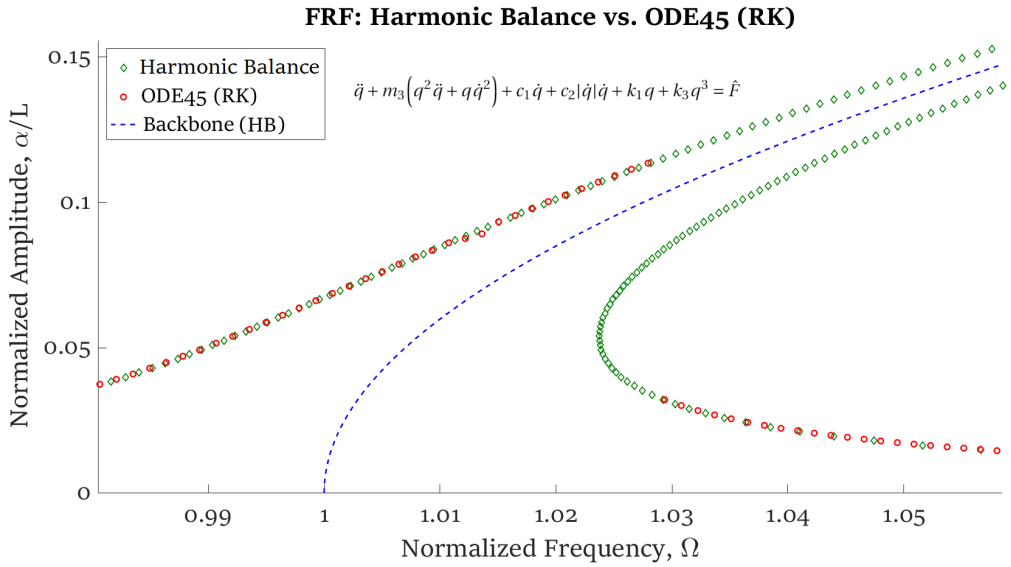

Figure 4.12: Results of the Harmonic Balance Method compared with Runge-Kutta (ODE45)

4.3 Comparison of Results

In the current section results obtained through the various methods are compared and similarities or discrepancies are discussed. Figure 4.13 plots different results in a single graph. These include the FRFs obtained through HBM and RK, the experimental backbones and the experimental sine-sweeps. These results are plotted using k_3 values from curve fitting the backbones, m_3 values from the analytical model and c_2 values from curve fitting the damping skeletons. The results show that the analytical result underestimates the response amplitude. The reason for this is unknown.

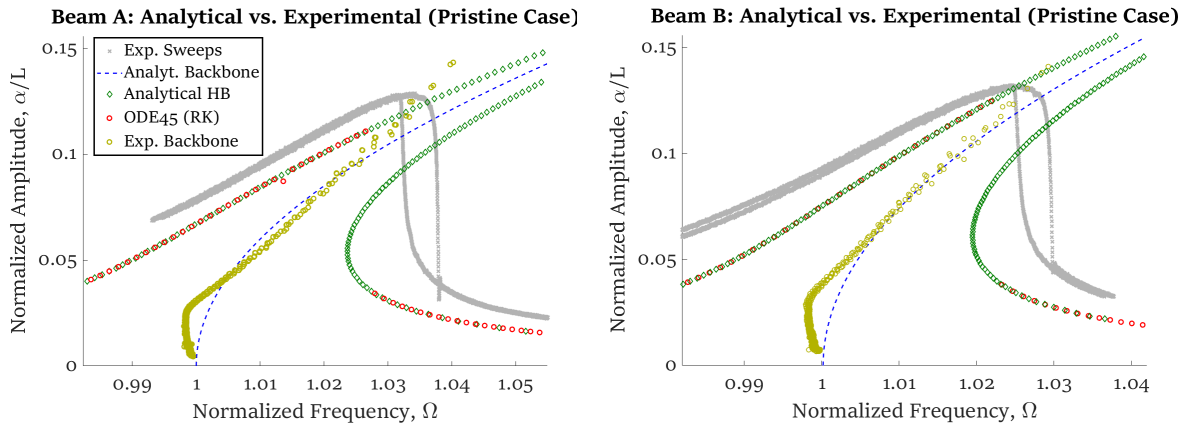

Figure 4.13: Experimental results compared with analytical results; FRF and backbone.

Discrepancy between analytic and experimental cubic stiffness

A discrepancy between experimental and analytical cubic stiffness coefficients was witnessed (Table 4.2). The analytically obtained values for the cubic stiffness (k_{3th}) are significantly lower than the experimental values (k_3). More specifically stated, the hardening was underestimated in the model. This means that either the experimental results or the analytical results are inaccurate. Upon comparison of the experimental results, it is evident that the FRFs, backbones and FFTs all agree with each other and therefore no significant errors are expected. Hence, the analytical model might have shortcomings for the current use case. According to the fundamental relationship expressed in Equation 4.1, the discrepancy is attributed to either an underestimation of the nonlinear stiffness or an overestimation of the nonlinear inertia. The nonlinear inertia is assumed to be accurate in the current case.

$$\omega(\alpha) \approx \sqrt{\frac{k_{eq}(\alpha)}{m_{eq}(\alpha)}} \tag{4.1}$$

Reasons for the discrepancy and potential model improvement suggestions are now speculated:

- The assumption in the analytical model that the bending strain energy is the only contribution to the potential energy might be incorrect. At low amplitudes this assumption does hold true, however, at large amplitudes, geometrical effects could cause this assumption to no longer be valid. At high amplitudes, a part of the inertial forces causes axial stresses. This hypothesised effect is visualized in Figure 4.14. The occurring axial stress does not contribute to the bending strain. This would explain the additional hardening at high amplitudes. Pure bending is therefore

no longer the case and the mechanics become more complicated. This effect can be seen as an additional nonlinearity. The contribution of the axial strain energy would have to be included to account for these effects. A stiffening effect due to axial stresses for vibrating cantilever beams subjected to base rotation was also reported by researchers [22] [105]. Using the same nonlinear structural theory as this work (nonlinear Euler-Bernouilli theory), Villanueva et al. [23] also witnessed a significant mismatch between their analytical and experimental results for the first bending mode of cantilever beams. They also found the discrepancy to increase for lower length to width ratios. According to the researchers [23], theories beyond Euler-Bernoulli would have to applied, which account for more complex stress distributions.

- To account for nonlinearities with large deformations, Euler-Bernouilli can be extended using von Karman strains. The full von Karman nonlinearity accounts for the coupling between extensional and bending responses in beams with moderately large rotations but small strains. According to Khodabakhshi and Reddy [106], the von Karman nonlinearity has a stiffening effect in beams. They also stated that the influence is more prominent in thin beams than in thick beams [106].
- The exclusion of higher order terms in the Taylor series expansions and related approximations (Equation 2.13, 2.14 and 2.15) might have led to significant inaccuracies. Only terms up to the third order were kept within the approximation, but at high amplitudes of vibration the influence of these terms could be increasingly significant. As evident from the experimental backbone curves, the inclusion of higher order terms would result in better agreement between results.
- It might give improved results by calculating the nonlinear mechanics using nonlinear classical plate theory instead of beam theory. According to Rao [107], if the thickness to width ratio is less than 0.05 (which is true in the current case), plate theory should be employed to model the system. Nonlinear plate theories as described in [81] would be applicable for the system of focus.

In accordance with these statements, the limitations and assumptions of the applied model should be kept in mind upon application. It should be pointed out that the model in the current form is less suitable for highly nonlinear systems of this kind. Therefore it should be avoided for nonlinearities of this degree or improvements would have to be made to facilitate the mentioned shortcomings. All the suggested improvements would inevitably give rise to more complexity in the model.

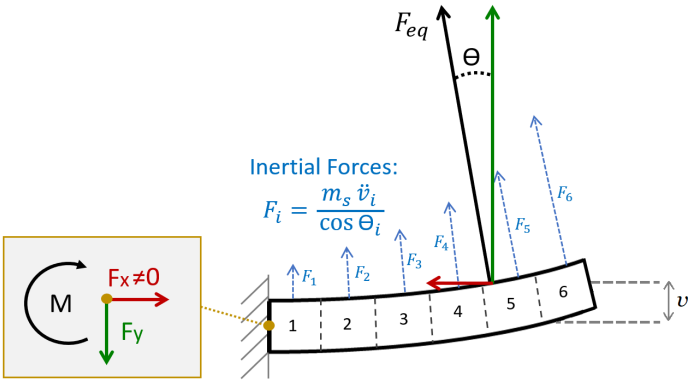

Figure 4.14: Possible explanation for the discrepancy in k_3 values.

CHAPTER 5

Conclusions and Recommendations

This research has investigated the nonlinear dynamic behavior of AL7075-T6 cantilever beams. Free vibration and sine-sweep experiments were performed showing significant nonlinear behavior. Several metrics were obtained and correlated to various stages of fatigue life. An analytical method based on Nonlinear Euler-Bernouilli theory and the Assumed Modes method, was employed to obtain the equation of motion. Analytical approximations, including Harmonic Balance, the Method of Averaging and Runge-Kutta, were applied to model the system response. The following section (5.1) details the conclusions drawn from this work, provides answers to the research questions, and states possible technical challenges. Finally, in section 5.2, recommendations for future work are given.

5.1 Conclusions

5.1.1 Answers to the Research Questions

Firstly, the research sub-questions stated in section 1.3 are answered:

1. *Which nonlinear effects (e.g. stiffness, damping, inertial) significantly contribute to the system dynamics and are therefore important to include in the analysis?*
   Nonlinear stiffness (k_3), which is the main cause of the hardening (stiffening), can be stated to have been the most influential nonlinearity. Nonlinear stiffness had the biggest influence on the shape of the FRFs and backbone curves. It is hereby important to note that the local changes in material elasticity (E) are linked to this parameter.
   It was evident that nonlinear damping (c_2 or ζ_2) was significant. Through estimation of this coefficient via the damping skeletons and subsequent verification using the MoA decay envelope model, the influence of this nonlinearity was clearly present. It was shown that at high amplitudes (≈0.1L) the effective damping ratio increased to approximately 500% of ζ_1 for all beams.
   Nonlinear inertia (m_3), is also determined to have a significant influence based on the analytical model. In the current case, the inclusion of the nonlinear inertial effects had a significant impact on the shape of the FRF (shifts to the left). Noninclusion of this coefficient would unfairly neglect the effect of all horizontal inertial forces.

2. *Can the applied analytical approach accurately describe the experimental results?*
   In terms of the free decay analysis, the decay envelopes obtained through MoA had excellent accuracy. The analytically determined envelopes were essentially indistinguishable from the

experimental envelopes. These results indicate the proper estimation of the damping coefficients c_1 (ζ_1) and c_2 (ζ_2).

Considering the FRFs and backbones, a difference in results was witnessed. The k_{3th} values from the theoretical analysis significantly underestimated the stiffening. Because of this, k_3 values obtained through curve-fitting the experimental backbones were used to plot the FRFs, which resulted in a better (but still imperfect) agreement. This indicates that the considered nonlinear effects in the analytical model are not the only factors for the nonlinear behavior. The discrepancy is expected to be caused by shortcomings of the model for the current use case. The potential reasons for this and model improvement suggestions were broadly detailed in section 4.3.

3. *How sensitive are the changes in nonlinear parameters over fatigue cycles compared to changes in the standard linear parameters?*

   The experimental results revealed significant changes in the shape of the backbone curves. For the obtained k_3 values no consistent pattern of change was noticeable. This is speculated to be caused by the insufficient fit of the model and the experimental data. Attributing the changes in the backbones to only the single coefficient k_3 would be unfair, because evidently higher order coefficients would be necessary to correctly quantify the witnessed phenomena.

   By quantifying the changes in the backbone curves in a different manner, such as the proposed bending point amplitude (BPA) and bending point slope (BPS), a damage precursor index could also be developed. The witnessed changes in BPA and BPS were fairly consistent and for all beams approximately 5 times more sensitive than the changes in linear frequencies. Based on the sensitivity alone, this would be a highly effective damage indicator.

   The metric ΔF_{jump} was also shown to be sensitive to damage. For all three beams this metric increased over fatigue levels, with a sensitivity more than ten times higher than changes in linear frequencies. However, because the magnitude of excitation was not precisely constant for all tests, this correlation can only be stated with a certain level of uncertainty.

   In the case of nonlinear damping **(c_2)** there was no definitive pattern of change, which is in line with the expectations, because no potential changes could have occurred with the parameters linked to the physics behind this nonlinearity (air drag).

4. *What is the potential value of including nonlinear analysis in SHM applications?*

   Depending on the degree of nonlinearity that the system exhibits, the value of monitoring the identified nonlinear parameters can be essential. Aside from the mentioned increased sensitivity to damage, these identification methods and additional parameters provide more system information than one would obtain by traditional (linear) methods. Incorrect estimations of the natural frequency due to nonlinearities would also be avoided. By incorporating nonlinear effects in failure models and control techniques, increased reliability and resilience is soundly expected. These nonlinear techniques should not be considered a replacement for current techniques, but rather an extension that enables more sophisticated failure models.

Having answered the sub-questions, the main research question is answered next:

■ *Can nonlinear dynamic analysis lead to improved damage precursor detection and why?*

Based on the obtained results, it can be stated that the monitoring of nonlinear parameters can lead to improved detection. The increased sensitivity observed for parameters linked to the backbone curves (BPA and BPS), could be exploited for improved damage detection. Other techniques, such as data-driven methods, could also be applied to assess the clear changes witnessed in the backbone curves. The metric Δf_{jump} was also found to be sensitive, but may not be practical to monitor in real-world applications, because of the necessity of highly specific and controlled excitation frequency and amplitude. The additional system information associated with the inclusion of nonlinear effects is also expected to result in improved decision-making and control techniques. It is hereby important to note that a thorough understanding of nonlinear dynamics, nonlinear structural mechanics and the potential failure mechanisms, is considered a necessity for effective implementation. The discussed dynamic effects also depend on the type of system in question and it is unknown how these parameters evolve for other systems (e.g.: other shapes, materials and dimensions). In summary, if it is possible to extract the necessary parameters for nonlinear systems in real-world applications with reasonable accuracy, then the answer to the research question is: yes.

5.1.2 General Conclusions

Further relevant conclusions drawn from the current research are stated in the following:

- The experimental and signal processing techniques applied in this work are a simple and effective means for the production of useful graphs, such as backbone curves and damping skeletons. It was shown that the nonlinear coefficients can be obtained experimentally using these graphs and the equivalent equations (k_{eq} and c_{eq}) derived from the Harmonic Balance Method.
- Backbone curves have proven to be a very valuable tool for tracking material degradation. It was evident that the shapes of the obtained backbone curves change for increasing fatigue cycles. This is caused by local changes in the elasticity and the occurrence of cracks in the damage-prone region. In terms of data-driven or hybrid analysis, higher order terms (stiffness and inertial) would be necessary to accurately replicate this behavior. The inclusion of higher order stiffness terms was also recommended and applied by [78].
- Nonlinearities of the magnitudes in the experiments of this work are unlikely to be encountered in practical applications, therefore the structural mechanical theory used within this work, which works better in regions of weakly nonlinear behavior, could still be fairly accurate to apply.

It can be stated that for systems exhibiting nonlinear behavior, the monitoring of changes in nonlinear system parameters can potentially lead to higher sensitivity in tracking damage precursors and the inclusion of these parameters should result in more sophisticated failure models. This does depend on the system and use case. Further investigation is necessary to establish a proper failure model or damage precursor index. Technical challenges that may arise upon implementation are discussed in the following.

5.1.3 Technical Challenges

Although the methods treated in this work show to be very promising for application in damage (precursor) detection, it is important to note that certain technical challenges may arise upon implementation, which should be considered to successfully incorporate into practical applications. The first challenge entails the necessity of high accuracy sensors capable of identifying structural response with minimal error and noise. Whats more, most of the analysis techniques require a considerable amount of computing power, which might not be practical for real time application. On a positive note, sensor and computing technologies continue to improve, allowing for the implementation of increasingly complex identification methods in the future. Experimental techniques for nonlinear dynamical analysis usually depend on controlled excitations, but in practical applications the loads are less predictable and more random in nature. The practical constraints should be kept in mind, such as the time-varying nature of the response and the absence of precise excitation measurement. The presence of noise, which was witnessed to be highly detrimental to the results, is also an important aspect to consider, because practical applications are generally not noise proof. The additional burden associated with nonlinear analysis can be substantial. Therefore the additional efforts should be weighed against the impact of nonlinearities. And of course, if the system does not exhibit nonlinear behavior, there is no need to apply such methods.

5.2 Recommendations

Based on the findings and shortcomings of this study, the following recommendations are given for potential future work:

Analytical Approach:

- Investigate potential improvements upon the nonlinear structural model based on the stated suggestions in section 4.3 to resolve the observed discrepancy for the nonlinear stiffness.
- Perform FEM analyses (dynamic nonlinear) to model the behavior. The complexity associated with (strongly) nonlinear behavior makes accurate analytical methods difficult to realize. Cracks and local changes in elasticity could be modelled to investigate the effects on the system dynamics.
- Investigate the evolution of parameters related to the phase (e.g. phase portraits and Bode plots).
- Develop an expression for drops in material elasticity as a function of beam horizontal position, $E(x)$. For this additional micro/meso-experiments would have to be performed to assess the changes in elasticity along the length of the beam. This could then be used to analytically simulate the damaged responses.

Experimental approach

- Investigate sequential amplitude values of resonance (both linear and nonlinear regime). This would give an additional metric, which can be correlated to fatigue life. Due to unfavorable variances in the sine-sweep excitation amplitudes this was not possible in the current work. The magnitude of stiffening is also sensitive to small changes in excitation amplitude.

- Perform automatically controlled (with feedback loop) fatigue testing instead of manually controlled tests. This would achieve more sophisticated and consistent infliction of fatigue damage.
- Vary the fatigue testing parameters including the stress (amplitude) and duration of each period. A lower fatigue infliction per period would better detail the 'damage precursor' zone.
- Retrieve more data sets through extensive experiments to have stronger statistical verification of the results. Due to technical difficulties not all the planned tests were executed in this work.
- Additionally test nonlinear sine sweeps at lower excitation amplitudes. Based on the obtained backbone curves, softening is expected at response amplitudes around $0.015L$, for increasing fatigue cycles. It would be interesting to experimentally verify this notion. Furthermore, it would be worthwhile to also obtain the backbones using sine sweep excitations of varying amplitudes and to assess whether they match the backbones curves obtained from free decay data.
- Include more measuring points across the beam length to assess the changes in the mode shapes. In the current work only the response at the beam tip was measured.
- It is important to have zero/minimal noise during free vibration testing, because it can have a detrimental effect on the backbone curves and damping skeletons. It would also be interesting to investigate whether nonlinear parameters can be extracted from data with noise levels similar to practical cases.
- Develop a method for analyzing nonlinear response due to excitations similar to loads in occurring practice, which are less predictable or consistent. The processing would not be as straightforward as controlled testing, but some of the techniques in this work could be applied.
- Employ a method to visually verify cracks upon occurrence to distinguish between dynamics brought on by cracks or by other microstructural changes associated with damage precursors.

Bibliography

[1] L. Bornn, C. R. Farrar, and G. Park, "Damage detection in initially nonlinear systems," *International Journal of Engineering Science*, vol. 48, pp. 909–920, oct 2010.

[2] J. B. Libot, L. Arnaud, O. Dalverny, J. Alexis, P. Milesi, and F. Dulondel, "Mechanical fatigue assessment of SAC305 solder joints under harmonic and random vibrations," 2016.

[3] S. Mathew, D. Das, M. Osterman, M. Pecht, R. Ferebee, and J. Clayton, "Virtual Remaining Life Assessment of Electronic Hardware Subjected to Shock and Random Vibration Life Cycle Loads," *Journal of the IEST*, vol. 50, pp. 86–97, apr 2007.

[4] C. R. Farrar and K. Worden, "An introduction to structural health monitoring," *Philosophical Transactions of the Royal Society A: Mathematical, Physical and Engineering Sciences*, vol. 365, pp. 303–315, feb 2007.

[5] E. M. Habtour, D. P. Cole, C. M. Kube, T. C. Henry, R. A. Haynes, F. Gardea, T. Sano, and T. Tinga, "Structural state awareness through integration of global dynamic and local material behavior," *Journal of Intelligent Material Systems and Structures*, 2019.

[6] Ö. Arslan, M. Aykan, and H. Nevzat Özgüven, "Parametric identification of structural nonlinearities from measured frequency response data," *Mechanical Systems and Signal Processing*, vol. 25, no. 4, pp. 1112–1125, 2011.

[7] A. Carrella and D. J. Ewins, "Identifying and quantifying structural nonlinearities in engineering applications from measured frequency response functions," *Mechanical Systems and Signal Processing*, vol. 25, no. 3, pp. 1011–1027, 2011.

[8] T. Dossogne, J. P. Noël, L. Masset, G. Kerschen, and B. Peeters, "Understanding and Modeling Nonlinear Behaviors in Aerospace Structures using Sine-Sweep Testing," 2018.

[9] T. Butlin, J. Woodhouse, and A. R. Champneys, "The landscape of nonlinear structural dynamics: an introduction," *Philosophical Transactions of the Royal Society A: Mathematical, Physical and Engineering Sciences*, vol. 373, p. 20140400, sep 2015.

[10] J. M. Londoño, S. A. Neild, and J. E. Cooper, "Identification of backbone curves of nonlinear systems from resonance decay responses," *Journal of Sound and Vibration*, vol. 348, pp. 224–238, 2015.

[11] R. A. Haynes, E. Habtour, T. C. Henry, D. P. Cole, and B. Wisner, "Damage Precursor Indicator for Aluminum 7075-T6 based on Nonlinear Dynamics," 2019.

[12] P. M. S. Burt and J. H. de Morais Goulart, "Efficient Computation of Bilinear Approximations and Volterra Models of Nonlinear Systems," *IEEE Transactions on Signal Processing*, vol. 66, pp. 804–816, feb 2018.

[13] M. Akbarzade and A. Farshidianfar, "Nonlinear transversely vibrating beams by the improved energy balance method and the global residue harmonic balance method," *Applied Mathematical Modelling*, vol. 45, pp. 393–404, 2017.

[14] J. Liu, D. T. Martin, T. Nishida, L. N. Cattafesta, M. Sheplak, and B. P. Mann, "Harmonic Balance Nonlinear Identification of a Capacitive Dual-Backplate MEMS Microphone," 2008.

[15] S. S. Singh, P. Pal, and A. K. Pandey, "Pull-in analysis of non-uniform microcantilever beams

under large deflection," *Journal of Applied Physics*, vol. 118, no. 20, 2015.

[16] K. Worden and G. R. Tomlinson, *Nonlinearity in Structural Dynamics: Detection, Identification and Modelling*.
CRC Press, 2000.

[17] L. Renson, G. Kerschen, and A. Newerla, "Nonlinear Modal Analysis of the Smallsat Spacecraft," 2012.

[18] B. Zaghari, E. Rustighi, and M. G. Tehrani, "Dynamic response of a nonlinear parametrically excited system subject to harmonic base excitation," *Journal of Physics: Conference Series*, vol. 744, no. 1, 2016.

[19] S. B. Shiki and S. da Silva, "Evaluation of damage indexes for structural health monitoring in nonlinear mechanical systems based on Volterra series," *Journal of Physics: Conference Series*, vol. 628, jul 2015.

[20] K. Worden, C. R. Farrar, J. Haywood, and M. Todd, "A review of nonlinear dynamics applications to structural health monitoring," *Structural Control and Health Monitoring*, 2008.

[21] P. T. Brewick and S. F. Masri, "An evaluation of data-driven identification strategies for complex nonlinear dynamic systems," *Nonlinear Dynamics*, vol. 85, no. 2, pp. 1297–1318, 2016.

[22] O. Thomas, A. Sénéchal, and J.-F. Deü, "Hardening/softening behavior and reduced order modeling of nonlinear vibrations of rotating cantilever beams," *Nonlinear Dynamics*, vol. 86, pp. 1293–1318, oct 2016.

[23] L. G. Villanueva, R. B. Karabalin, M. H. Matheny, D. Chi, J. E. Sader, and M. L. Roukes, "Nonlinearity in nanomechanical cantilevers," *Physical Review B - Condensed Matter and Materials Physics*, vol. 87, no. 2, pp. 1–8, 2013.

[24] A. Motallebi, S. Irani, and S. Sazesh, "Analysis on jump and bifurcation phenomena in the forced vibration of nonlinear cantilever beam using HBM," *Journal of the Brazilian Society of Mechanical Sciences and Engineering*, vol. 38, no. 2, pp. 515–524, 2016.

[25] D. P. Cole, E. M. Habtour, T. Sano, S. J. Fudger, S. M. Grendahl, and A. Dasgupta, "Local Mechanical Behavior of Steel Exposed to Nonlinear Harmonic Oscillation," *Experimental Mechanics*, vol. 57, no. 7, pp. 1027–1035, 2017.

[26] E. M. Habtour, D. P. Cole, J. Riddick, V. Weiss, M. Robeson, R. Sridharan, and A. Dasgupta, "Detection of fatigue damage precursor using a nonlinear vibration approach," *Structural Control and Health Monitoring*, no. 1, 2016.

[27] E. Habtour, D. P. Cole, S. C. Stanton, R. Sridharan, and A. Dasgupta, "Damage precursor detection for structures subjected to rotational base vibration," *International Journal of Non-Linear Mechanics*, vol. 82, pp. 49–58, 2016.

[28] L. Ljung, "Perspectives on system identification," *Annual Reviews in Control*, vol. 34, pp. 1–12, apr 2010.

[29] J. Sjoberg, Q. Zhang, L. Ljung, A. Benveniste, B. Delyon, P. Glorennec, H. Hjalmarsson, and A. Juditsky, "Nonlinear Black-box Modeling in System Identification: a Unified Overview," *Automatica*, vol. 31, no. 12, 1995.

[30] G. J. G. Jin, M. Sain, K. Pham, J. Billie, F.S., and J. Ramallo, "Modeling MR-dampers: a nonlinear blackbox approach," *Proceedings of the 2001 American Control Conference*, vol. 1, 2001.

[31] L. A. Aguirre and C. Letellier, "Modeling Nonlinear Dynamics and Chaos: A Review," *Mathematical Problems in Engineering*, vol. 2009, pp. 1–35, 2009.

[32] M. Maboodi, E. F. Camacho, and A. Khaki-Sedigh, "Non-linear generalised minimum variance control state space design for a second-order Volterra series model," *International Journal of Systems Science*, vol. 46, pp. 2607–2616, oct 2015.

[33] C. M. Cheng, Z. K. Peng, W. M. Zhang, and G. Meng, "Volterra-series-based nonlinear system modeling and its engineering applications_ A state-of-the-art review," *Mechanical Systems and Signal Processing*, vol. 87, no. November 2016, pp. 340–364, 2017.

[34] A. Chatterjee, "Structural damage assessment in a cantilever beam with a breathing crack using higher order frequency response functions," *Journal of Sound and Vibration*, vol. 329, pp. 3325–3334, aug 2010.

[35] E. Rabiei, E. L. Droguett, and M. Modarres, "A prognostics approach based on the evolution of damage precursors using dynamic Bayesian networks," *Advances in Mechanical Engineering*, vol. 8, no. 9, pp. 1–19, 2016.

[36] S. Gupta and A. Ray, "Symbolic Dynamic Filtering for Data-Driven Pattern Recognition," 2007.

[37] C. Rao, A. Ray, S. Sarkar, and M. Yasar, "Review and comparative evaluation of symbolic dynamic filtering for detection of anomaly patterns," *Signal, Image and Video Processing*, vol. 3, no. 2, pp. 101–114, 2009.

[38] R. P. Patankar, V. Rajagopalan, and A. Ray, "Failure precursor detection in complex electrical systems using symbolic dynamics," 2008.

[39] G. Sirca and H. Adeli, "System identification in structural engineering," *Scientia Iranica*, vol. 19, no. 6, pp. 1355 – 1364, 2012.

[40] W. Lacarbonara, *Nonlinear Structural Mechanics*.
Boston, MA: Springer US, 2013.

[41] T. L. Hill, S. A. Neild, and D. J. Wagg, "Comparing the direct normal form method with harmonic balance and the method of multiple scales," 2017.

[42] Z. Yan, H. E. Taha, and T. Tan, "Nonlinear characteristics of an autoparametric vibration system," *Journal of Sound and Vibration*, vol. 390, pp. 1–22, 2017.

[43] S. K. Chakrapani and D. J. Barnard, "Determination of acoustic nonlinearity parameter (β) using nonlinear resonance ultrasound spectroscopy: Theory and experiment," *The Journal of the Acoustical Society of America*, vol. 141, no. 2, pp. 919–928, 2017.

[44] G. Kerschen, K. Worden, A. F Vakakis, and J.-C. Golinval, "Nonlinear system identification in structural dynamics: Current status and future directions," *Conference Proceedings of the Society for Experimental Mechanics Series*, 01 2007.

[45] G. Kerschen, M. Peeters, J. Golinval, and A. Vakakis, "Nonlinear normal modes, Part I: A useful framework for the structural dynamicist," *Mechanical Systems and Signal Processing*, vol. 23, pp. 170–194, jan 2009.

[46] M. Peeters, G. Kerschen, and J. Golinval, "Dynamic testing of nonlinear vibrating structures using nonlinear normal modes," *Journal of Sound and Vibration*, vol. 330, pp. 486–509, jan 2011.

[47] W. Lacarbonara, B. Carboni, and G. Quaranta, "Nonlinear normal modes for damage detection," *Meccanica*, vol. 51, pp. 2629–2645, nov 2016.

[48] S. A. Neild, A. R. Champneys, D. J. Wagg, T. L. Hill, and A. Cammarano, "The use of normal forms for analysing nonlinear mechanical vibrations," *Philosophical Transactions of the Royal Society A: Mathematical, Physical and Engineering Sciences*, vol. 373, no. 2051, 2015.

[49] S. A. Neild and D. J. Wagg, "Applying the method of normal forms to second-order nonlinear vibration problems," *Proceedings of the Royal Society A: Mathematical, Physical and Engineering Sciences*, vol. 467, no. 2128, pp. 1141–1163, 2011.

[50] A. Cammarano, T. L. Hill, P. L. Green, and S. A. Neild, "Backbone curves and Nonlinear normal modes: a new identification tool," *Proceedings of the British Society for Strain Measurement*, 2015.

[51] A. D. Shaw, T. L. Hill, S. A. Neild, and M. I. Friswell, "Periodic responses of a structure with 3:1 internal resonance," *Mechanical Systems and Signal Processing*, vol. 81, pp. 19–34, 2016.

[52] J. A. Belinchon, T. Harko, and M. K. Mak, "Approximate Analytical Solution for the Dynamic Model of Large Amplitude Non-Linear Oscillations Arising in Structural Engineering," 2017.

[53] X. Wang, T. L. Hill, S. A. Neild, A. D. Shaw, H. Haddad Khodaparast, and M. I. Friswell, "Model updating strategy for structures with localised nonlinearities using frequency response measurements," *Mechanical Systems and Signal Processing*, vol. 100, pp. 940–961, 2018.

[54] M. Jamal-Omidi, M. Shayanmehr, and S. Sazesh, "A fundamental study on the free vibration of geometrical nonlinear cantlever beam using an exact solution and experimental investigation," *Archive of Mechanical Engineering*, vol. 65, no. 1, 2018.

[55] W. M. Ostachowicz and M. Krawczuk, "Analysis of the effect of cracks on the natural frequencies of a cantilever beam," *Journal of Sound and Vibration*, vol. 150, no. 2, pp. 191–201, 1991.

[56] M. S. Mia, M. S. Islam, and U. Ghosh, "Modal analysis of cracked cantilever beam by finite element simulation," *Procedia Engineering*, vol. 194, pp. 509–516, 2017.

[57] T. Tinga and R. Loendersloot, "Aligning PHM, SHM and CBM by understanding the physical system failure behaviour," *Proceedings of the European Conference of the Prognostics and Health Management Society*, pp. 162–171, 2014.

[58] T. H. Ooijevaar, L. L. Warnet, R. Loendersloot, R. Akkerman, and T. Tinga, "Impact damage identification in composite skin-stiffener structures based on modal curvatures," *Structural Control and Health Monitoring*, vol. 23, pp. 198–217, feb 2016.

[59] V. P. Kos, J. Slavic, and M. Boltezar, "Fatigue Damage for Sweep-Sine and Random Accelerated Vibration Testing," *Advances in Mechanical Engineering*, vol. 7, no. 1, 2015.

[60] M. Mršnik, J. Slavič, and M. Boltežar, "Vibration fatigue using modal decomposition," *Mechanical Systems and Signal Processing*, vol. 98, pp. 548–556, 2018.

[61] D. W. Jordan and P. Smith, *Nonlinear Ordinary Differential Equations: An Introduction for Scientists and Engineers*.
Oxford University Press, 4 ed., 2007.

[62] M. A. Hosen and M. S. Chowdhury, "A new analytical technique based on harmonic balance method to determine approximate periods for Duffing-harmonic oscillator," *Alexandria Engineering Journal*, vol. 54, no. 2, pp. 233–239, 2015.

[63] H. Liao, "Piecewise constrained optimization harmonic balance method for predicting the limit cycle oscillations of an airfoil with various nonlinear structures," *Journal of Fluids and Structures*,

vol. 55, pp. 324–346, 2015.

[64] Z. Q. Lu, G. S. Hu, H. Ding, and L. Q. Chen, "Jump-based estimation for nonlinear stiffness and damping parameters," *JVC/Journal of Vibration and Control*, no. June, 2018.

[65] T. A. Doughty, P. Davies, and A. K. Bajaj, "A comparison of three techniques using steady state data to identify non-linear modal behavior of an externally excited cantilever beam," *Journal of Sound and Vibration*, vol. 249, no. 4, pp. 785–813, 2002.

[66] A. J. Elliott, A. Cammarano, and S. A. Neild, "Comparing Analytical Approximation Methods with Numerical Results for Nonlinear Systems," *Nonlinear Dynamics, Volume 1*, vol. 1, pp. 37–49, 2017.

[67] S. Dou and J. S. Jensen, "Optimization of nonlinear structural resonance using the incremental harmonic balance method," *Journal of Sound and Vibration*, vol. 334, pp. 239–254, 2015.

[68] J. K. Liu, F. X. Chen, and Y. M. Chen, "Bifurcation analysis of aeroelastic systems with hysteresis by incremental harmonic balance method," *Applied Mathematics and Computation*, vol. 219, no. 5, pp. 2398–2411, 2012.

[69] M. H. U. Molla and M. Alam, "Higher accuracy analytical approximations to nonlinear oscillators with discontinuity by energy balance method," *Results in Physics*, vol. 7, 2017.

[70] M. A. Hosen, M. S. Chowdhury, M. Y. Ali, and A. F. Ismail, "A novel analytical approximation technique for highly nonlinear oscillators based on the energy balance method," *Results in Physics*, vol. 6, pp. 496–504, 2016.

[71] R. Roy, "Averaging method for strongly non-linear oscillators with periodic excitations," *International Journal of Non-Linear Mechanics*, vol. 29, pp. 737–753, sep 1994.

[72] V. Kumar, J. K. Miller, and J. F. Rhoads, "Nonlinear parametric amplification and attenuation in a base-excited cantilever beam," *Journal of Sound and Vibration*, vol. 330, no. 22, 2011.

[73] S. J. Zhu, Y. F. Zheng, and Y. M. Fu, "Analysis of non-linear dynamics of a two-degree-of-freedom vibration system with non-linear damping and non-linear spring," *Journal of Sound and Vibration*, vol. 271, no. 1-2, pp. 15–24, 2004.

[74] E. H. Dowell, "Some Recent Advances in Nonlinear Aeroelasticity: Fluid-Structure Interaction in the 21st Century," *Structure*, no. April, 2010.

[75] U. Fuellekrug and D. Goege, "Identification of weak non-linearities within complex aerospace structures," *Aerospace Science and Technology*, vol. 23, no. 1, pp. 53–62, 2012.

[76] M. Piraccini, D. Di Maio, and R. Di Sante, "Nonlinear Modal Testing Performed by Pulsed-Air Jet Excitation System," 2016.

[77] L. Renson, A. Gonzalez-Buelga, D. A. Barton, and S. A. Neild, "Robust identification of backbone curves using control-based continuation," *Journal of Sound and Vibration*, vol. 367, pp. 145–158, 2016.

[78] J. M. Londoño, J. E. Cooper, and S. A. Neild, "Identification of systems containing nonlinear stiffnesses using backbone curves," *Mechanical Systems and Signal Processing*, vol. 84, 2017.

[79] A. M. J. Pickard, "Composite non-linearity in high cycle fatigue experimentation," in *Nonlinear Dynamics, Volume 2* (G. Kerschen, ed.), pp. 183–189, Springer, 2014.

[80] S. Vantadori, R. Haynes, G. Fortese, E. Habtour, C. Ronchei, D. Scorza, and A. Zanichelli, "Methodology for assessing embryonic cracks development in structures under high-cycle

multiaxial random vibrations," *Fatigue and Fracture of Engineering Materials and Structures*, vol. 41, no. 1, pp. 20–28, 2018.

[81] A. H. Nayfeh and P. F. Pai, *Linear and Nonlinear Structural Mechanics*.
John Wiley & Sons, Inc., 2004.

[82] H. Baruh, *Analytical Dynamics*.
McGraw-Hill, 1999.

[83] P. Malatkar, *Nonlinear Vibrations of Cantilever Beams and Plates*.
Phd thesis, Virginia Tech, 2003.

[84] L. Meirovitch, *Fundamentals of Vibrations*.
Mcgraw-Hill, 2000.

[85] E. Esmailzadeh and N. Jalili, "Parametric response of cantilever Timoshenko beams with tip mass under harmonic support motion," *International Journal of Non-Linear Mechanics*, vol. 33, no. 5, pp. 765–781, 1998.

[86] R. E. Mickens, *Truly Nonlinear Oscillations*.
World Scientific, jan 2010.

[87] M. J. Brennan, I. Kovacic, A. Carrella, and T. P. Waters, "On the jump-up and jump-down frequencies of the Duffing oscillator," *Journal of Sound and Vibration*, vol. 318, no. 4-5, pp. 1250–1261, 2008.

[88] T. J. Anderson, A. H. Nayfeh, and B. Balachandran, "Experimental Verification of the Importance of The Nonlinear Curvature in the Response of a Cantilever Beam," *Journal of Vibration and Acoustics*, vol. 118, no. 1, p. 21, 1996.

[89] A. G. Egorov, A. M. Kamalutdinov, and A. N. Nuriev, "Evaluation of aerodynamic forces acting on oscillating cantilever beams based on the study of the damped flexural vibration of aluminium test samples," *Journal of Sound and Vibration*, vol. 421, pp. 334–347, 2018.

[90] A. H. Nayfeh and D. T. Mook, *Nonlinear Oscillations*.
John Wiley & Sons, Inc., 1995.

[91] A. H. Nayfeh, *Perturbation Methods*.
Weinheim, Germany: John Wiley & Sons, Inc, 2000.

[92] B. R. Hunt, *Differential Equations with Matlab*.
Wiley, 3 ed., 2012.

[93] Z. F. Xin, S. A. Neild, D. J. Wagg, and Z. X. Zuo, "Resonant response functions for nonlinear oscillators with polynomial type nonlinearities," *Journal of Sound and Vibration*, vol. 332, no. 7, 2013.

[94] R. Nunes and J. Adams, "Metals HandBook Vol. 2, Properties and Selection: Nonferrous Alloys and Special-Purpose Materials," 1992.

[95] C. Hudson, "A study of fatigue and fracture in 7075-T6 aluminum alloy in vacuum and air environments," 1973.

[96] E. Zalnezhad, A. A. D. Sarhan, and M. Hamdi, "A fuzzy logic based model to predict surface hardness of thin film TiN coating on aerospace AL7075-T6 alloy," *The International Journal of Advanced Manufacturing Technology*, vol. 68, pp. 415–423, sep 2013.

[97] V. Weiss and J. Sessler, "Aerospace Structural Metals Handbook," 1972.

[98] J. Newman, "Fatigue and Crack-growth Analyses under Giga-cycle Loading on Aluminum Alloys," *Procedia Engineering*, vol. 101, pp. 339–346, 2015.

[99] ASM International Handbook Committee, *Properties and Selection: Nonferrous Alloys and Special-Purpose Materials*, vol. Vol. 2.
ASM International, 1992.

[100] A. Carrella, M. J. Brennan, T. P. Waters, and V. Lopes, "Force and displacement transmissibility of a nonlinear isolator with high-static-low-dynamic-stiffness," *International Journal of Mechanical Sciences*, vol. 55, no. 1, pp. 22–29, 2012.

[101] E. Wahyuni and T. Ji, "Relationship between Static Stiffness and Modal Stiffness of Structures," *The Journal for Technology and Science*, vol. 21, no. 2, 2010.

[102] M. S. Cao, G. G. Sha, Y. F. Gao, and W. Ostachowicz, "Structural damage identification using damping: A compendium of uses and features," *Smart Materials and Structures*, vol. 26, no. 4, 2017.

[103] M. Brunetti, J. Ciambella, L. Evangelista, E. Lofrano, A. Paolone, and A. Vittozzi, "Experimental results in damping evaluation of a high-speed railway bridge," *Procedia Engineering*, vol. 199, pp. 3015–3020, 2017.

[104] H. Mevada and D. Patel, "Experimental Determination of Structural Damping of Different Materials," *Procedia Engineering*, vol. 144, pp. 110–115, 2016.

[105] H. Kim, H. Hee Yoo, and J. Chung, "Dynamic model for free vibration and response analysis of rotating beams," *Journal of Sound and Vibration*, vol. 332, no. 22, pp. 5917–5928, 2013.

[106] P. Khodabakhshi and J. N. Reddy, "A unified beam theory with strain gradient effect and the von Kármán nonlinearity," *Journal of Applied Mathematics and Mechanics*, vol. 97, jan 2017.

[107] S. S. Rao, *Vibration of Continuous Systems*.
John Wiley & Sons, Inc., 1 ed., 2006.

Appendices

APPENDIX A

Tables of Experimental Results

Beam A						
Fatigue Level	ζ_1 **(%)**	ζ_2(%)	$k_3(\times 10^{10})$	F_{nat} **(Hz)**	F_{RS} **(Hz)**	ΔF_{jump} **(Hz)**
Pristine	0.201	0.243	1.87	56.4	58.33	0.29
1	n/a	0.224	1.67	56.21	57.9	0.15
2	0.233	0.229	1.3	56.11	57.74	0.24
3	n/a	0.239	1.31	55.65	57.41	0.39
4	n/a	0.228	1.41	55.07	57.12	0.57
5	0.29	0.245	1.38	54.53	n/a	n/a
6	n/a	0.239	1.5	53.81	55.96	0.79
7	n/a	0.239	1.88	52.9	55.35	0.85
Beam B						
Fatigue Level	ζ_1 **(%)**	ζ_2(%)	$k_3(\times 10^{10})$	F_{nat} **(Hz)**	F_{RS} **(Hz)**	ΔF_{jump} **(Hz)**
Pristine	n/a	0.21	1.32	57.77	59.27	0.22
1	0.222	0.207	2.07	57.04	59.15	0.31
2	0.228	0.207	1.62	56.82	58.67	0.35
3	0.274	0.217	1.22	55.84	57.5	0.52
4	0.293	0.226	1.62	53.9	56.4	1.23
5	n/a	0.21	3.53	49.97	53.82	1.68
Beam C						
Fatigue Level	ζ_1 **(%)**	ζ_2(%)	$k_3(\times 10^{10})$	F_{nat} **(Hz)**	F_{RS} **(Hz)**	ΔF_{jump} **(Hz)**
Pristine	n/a	0.214	1.51	56.82	58.41	0.19
1	0.231	0.211	1.62	55.74	n/a	n/a
2	0.258	0.218	1.29	55.09	56.75	0.37
3	n/a	0.229	2.94	51.7	54.56	0.63

Table A.1: Experimentally obtained nonlinear coefficients (k_3, ζ_1 and ζ_2) and parameters from the sine sweeps (F_{nat}, F_{RS} and ΔF_{jump}).

ζ_1: Viscous damping ratio (Experimental)

ζ_2: Quadratic damping ratio (Experimental)

k_3: Cubic stiffness coefficient (Experimental)

F_{nat}: Natural frequency from linear sine-sweeps

F_{RS}: Resonant frequency from nonlinear (slow) sine-sweeps

F_{jump}: Difference between jump up and jump down frequencies

(Each fatigue level is 35000 cycles.)

APPENDIX B

MATLAB CODE FOR PROCESSING FREE VIBRATION DATA

```
%%%%%%%%%%%%%%%%%%%%%%%%%%%%%%%%%%%%%%%%%%%%%%%%%%%%%%%%%%%%%%%%%%%%%%%%%%%%%%%%
% DESCRIPTION:
% Experimental Data Processing - Free Vibration
% Code for analyzing time data of the free vibration of a cantilever beam.
% ************************************************************************
% Code Created: july 2018
% Code Author: T. Dragman
% University of Twente, Enschede, The Netherlands
% ************************************************************************
%REFERENCES:
%Londono, J. M., Neild, S. A., & Cooper, J. E. (2015). Identification of
%backbone curves of nonlinear systems from resonance decay responses.
%%%%%%%%%%%%%%%%%%%%%%%%%%%%%%%%%%%%%%%%%%%%%%%%%%%%%%%%%%%%%%%%%%%%%%%%%%%%%%%%
clear all; close all; clc;
set(0,'defaultAxesFontSize',22);set(0,'DefaultTextFontSize',22);
set(0,'DefaultLineLineWidth',1); set(0,'DefaultLineMarkerSize',5);
set(0,'DefaultAxesFontName','Sitka Subheading')

%% Load data from experiments
delimiterIn = ' '; %Data seperator character
headerlinesIn = 7; %Number of lines in the text file before the main data starts

%Tip response velocity data (laser vibrometer):
filename0 = 'Data\b06_fl0_free_vib_1.txt';
A0 = importdata(filename0,delimiterIn,headerlinesIn);
filename1 = 'Data\b06_fl1_free_vib_1.txt';
A1 = importdata(filename1,delimiterIn,headerlinesIn);
filename2 = 'Data\b06_fl2_free_vib_1.txt';
A2 = importdata(filename2,delimiterIn,headerlinesIn);
filename3 = 'Data\b06_fl3_free_vib_1.txt';
A3 = importdata(filename3,delimiterIn,headerlinesIn);
filename4 = 'Data\b06_fl4_free_vib_1.txt';
A4 = importdata(filename4,delimiterIn,headerlinesIn);
filename5 = 'Data\b06_fl5_free_vib_1.txt';
A5 = importdata(filename5,delimiterIn,headerlinesIn);
%Base acceleration data (accelerometer):
```

```
filename0 = 'Data\b06_fl0_free_r2a_1.txt';
C0 = importdata(filename0,delimiterIn,headerlinesIn);
filename1 = 'Data\b06_fl1_free_r2a_1.txt';
C1 = importdata(filename1,delimiterIn,headerlinesIn);
filename2 = 'Data\b06_fl2_free_r2a_1.txt';
C2 = importdata(filename2,delimiterIn,headerlinesIn);
filename3 = 'Data\b06_fl3_free_r2a_1.txt';
C3 = importdata(filename3,delimiterIn,headerlinesIn);
filename4 = 'Data\b06_fl4_free_r2a_1.txt';
C4 = importdata(filename4,delimiterIn,headerlinesIn);
filename5 = 'Data\b06_fl5_free_r2a_1.txt';
C5 = importdata(filename5,delimiterIn,headerlinesIn);

%% Specify sample and test details
%The natural frequency is obtained by running two or three linear sine sweep
%experiments at the start of an experimental session and averaging those values.
Fnat=57.75; %ENTER the average natural frequency (Fnat) of beam B in Hz (Pristine
    case)
CL=114;    %ENTER clamping length (CL) in mm
N=6;       %ENTER the number of measurements (# Damage cases + 1)
SL = length(A1.data(:,2));  %Sample length (#samples)
T  = A1.data(:,1);          %Time vector (Same for all files)
Ts = T(2)-T(1);             %Sampling rate (secs)
Fs = 1/Ts;                  %Sampling Freq (Hz)
NoNoise=[2 3 5];            %Cases without noise (Prist=1,Fat1=2,Fat2=3,...)
% ENTER Experimental natural frequencies obtained from linear sine sweeps:
Fvect=[57.75 57.04 56.82 55.84 53.9 49.89];
Nvect=[1 2 3 4 5 6];
%Color specification vector used to add colors to the plots at the various
%fatigue levels ([r g b], black=[0 0 0], white=[1 1 1])
C = {'k','m','b',[0 .7 0],[.7 .7 0],'r',[.8 .5 0],[0 .7 .7]};

%% Creation of data matrices
%Creation of matrices consisting of a seperate column for each fatigue level
    measurement.
%The sampling length and frequency should be the same for each column. E.g. column
    1 is
%data for pristine case, column 2 is data for fatigue level 1,...etc

Umat=zeros(SL,N); Amat=zeros(SL,N); %(rows=SL , columns=N)
%Tip Velocity
Umat(:,1) = A0.data(:,2)-mean(A0.data(:,2));
Umat(:,2) = A1.data(:,2)-mean(A1.data(:,2));
Umat(:,3) = A2.data(:,2)-mean(A2.data(:,2));
Umat(:,4) = A3.data(:,2)-mean(A3.data(:,2));
Umat(:,5) = A4.data(:,2)-mean(A4.data(:,2));
Umat(:,6) = A5.data(:,2)-mean(A5.data(:,2));
%Base Acceleration
Amat(:,1) = C0.data(:,2)-mean(C0.data(:,2));
Amat(:,2) = C1.data(:,2)-mean(C1.data(:,2));
```

```
Amat(:,3) = C2.data(:,2)-mean(C2.data(:,2));
Amat(:,4) = C3.data(:,2)-mean(C3.data(:,2));
Amat(:,5) = C4.data(:,2)-mean(C4.data(:,2));
Amat(:,6) = C5.data(:,2)-mean(C5.data(:,2));

%% Subtract base acceleration to get relative response and obtain improved results
%Intergrate base acceleration signal to obtain base velocity
Afilt=zeros(SL,N);  BaseVel=zeros(SL,N);
%Bandpass filter to prevent drift in base velocity (Butterworth filter)
%(order,[F1/Nyquist F2/Nyquist],'bandpass')
[b, a] = butter(2,[0.003 0.5],'bandpass'); %LP & HP: 0.003[4.7Hz] & 0.5[782Hz]
for i=1:N
Afilt(:,i)=filtfilt(b,a,Amat(:,i));
BaseVel(:,i)=cumtrapz(T(:,1),Afilt(:,i));     %Perform the trapezoidal integration
    and normalize (x/L)
BaseVel(:,i)=-1*smooth(BaseVel(:,i),20);      %Apply smoothing to base signal (very
     noisy compared to laser data)
BaseVel(:,i)=BaseVel(:,i)-mean(BaseVel(:,i)); %Subtract mean again
Umat(:,i)=Umat(:,i)-BaseVel(:,i);             %Subtract the base velocity from
    response velocity
end

%% Identifying peaks to determine time periods of interest
pksU=zeros(10,N); %Assuming no more than 10 free vibrations per measurement
locsU=zeros(10,N);
for i=1:N
[pks,locs] = findpeaks(Umat(:,i),'MinPeakDistance',10000,'MinPeakHeight',0.5);
Nlocu=length(locs);
pksU(1:Nlocu,i)=pks;
locsU(1:Nlocu,i)=locs;
NlocsU(1,i)=Nlocu;
end

%Plot figure displaying velocity time signals along with the identified peaks
figure(1),
title('Forward Sweeps with peaks')
for i = 1:N
subplot(3,2,i), hold on
caption = sprintf('Beam 3 - Tip Velocity - Free Vibration Case #%d', i);
title(caption, 'FontSize', 10);
plot(T(locsU(1:NlocsU(i),i),1),pksU(1:NlocsU(i),i),'color',C{i},'marker','o','
    linestyle','none');
hold on
plot(T(:,1),Umat(:,i),'color',C{9-i},'linestyle','-');
xlim([0 60])
ylim([-10 10])
end

%Make values of range ZeroLen right before peaks zero. This eliminates
%unwanted data regions when the beam is loaded before being released.
```

```
ZeroLen=5000;  % 5000points ~ 1.5 sec
for i=1:N
    for k=1:NlocsU(i)
Umat((locsU(k,i)-ZeroLen):locsU(k,i),i)=0;
    end
end

%Initialize variables to integrate velocity signal
Xmat=zeros(SL,N); Ufilt=zeros(SL,N);

%Bandpass filter (Butterworth) to prevent drift in displacement
%(order[=2],[F1/Nyquist F2/Nyquist],'bandpass')
[b, a] = butter(2,[0.003 0.5],'bandpass'); %0.003[4.7Hz] & 0.5[781Hz]
for i=1:N
Ufilt(:,i)=filtfilt(b,a,Umat(:,i));
end
clear a b
% Perform the integration using the Riemann method and normalize (x/L)
for i=1:N
   Xmat(:,i)=cumtrapz(T(:,1),Ufilt(:,i));  %Cumulative trapezoidal integration
   Xmat(:,i)=Xmat(:,i)/CL*1000;            %Normalize by beam length
   Xmat(:,i)=Xmat(:,i)-mean(Xmat(:,i));    %Subtract mean again
end

%Identify peaks in Displacement matrix (Xmatrix)
for i=1:N %(play with peak ID parameters)
[pksx,locsx] = findpeaks(Xmat(:,i),'MinPeakDistance',10000,'MinPeakHeight',0.01);
Nlocsx=length(locsx);
pksMx(1:Nlocsx,i)=pksx;
locsMx(1:Nlocsx,i)=locsx;
NlocsMx(1,i)=Nlocsx;
end

%Make values of range ZeroLen right before peaks zero again
for i=1:N
    for k=1:NlocsMx(i)
       Xmat((locsMx(k,i)-ZeroLen):locsMx(k,i),i)=0;
    end
end

%% Construct 3D X Matrix for further processing
maxNpeaks=max(NlocsMx); %Maximum number of peaks
minNpeaks=min(NlocsMx); %Maximum number of peaks

% Calculate distances between consecutive peaks
DistLocs=zeros(maxNpeaks,N);
for i=1:N
    for k=1:NlocsMx(i)-1
 DistLocs(k,i)=locsMx(k+1,i)-locsMx(k,i);
    end
```

```
end

MinDistLocs=min(DistLocs(DistLocs>0),[],'all');

N3D=MinDistLocs-501; %length for 3D displacement matrix
for i=1:N
    for k=1:NlocsMx(i)
        if (length(Umat(:,i))-locsMx(k,i) < N3D) % if last peak too close to end of time signal
     Xmat(locsMx(k,i)-20:end,i)=0;               % make that part of the signal zero
        end
    end
end

%Identify peaks in the new displacement matrix (Xmat)
for i=1:N
[pksx,locsx] = findpeaks(Xmat(:,i),'MinPeakDistance',10000,'MinPeakHeight',0.01);
Nlocsx=length(locsx);
pksMx(1:Nlocsx,i)=pksx;
locsMx(1:Nlocsx,i)=locsx;
NlocsMx(1,i)=Nlocsx;
end

%% Sort displacement signal to go from highest to lowest initial amplitude
LocSort=zeros(size(pksMx)); PksSort=LocSort; IdxSort=LocSort;
for i=1:N
[PksSort(:,i),IdxSort(:,i)] = sort(pksMx(:,i),'descend');
LocSort(:,i)=locsMx(IdxSort(:,i),i);
end

%Create 3D Displacement Matrix
X3D=zeros(N3D,N,minNpeaks);
for i=1:N
    for k=1:NlocsMx(i)
 X3D(1:N3D,i,k)=Xmat(LocSort(k,i):LocSort(k,i)+N3D-1,i);
    end
end

%% Plot figure displaying modified normalized displacement time signals along with the identified peaks
figure(2),
for i = 1:N
subplot(3,2,i), hold on
caption = sprintf('Beam B - Tip Displacement - Free Vibration Case #%d', i);
title(caption, 'FontSize', 10);
plot(T(locsMx(1:NlocsMx(i),i),1),pksMx(1:NlocsMx(i),i),'color',C{9-i},'marker','o','linestyle','none');
hold on
plot(T(:,1),Xmat(:,i),'color',C{i},'linestyle','-');
```

```
xlim([0 60])
ylim([-0.25 0.25])
end

%% Plot to check 3D matrix structure
figure(3),
for i = 1:N
    for k=1
subplot(3,2,i),
plot(T(1:N3D,1),X3D(:,i,k),'color',C{i},'linestyle','-');
    end
end

Nk=min(NlocsMx); %MINIMUM NUMBER OF MEASUREMENTS
PSL=10000;       %PLOT WINDOW LENGTH

%Plot sectioned displacement
figure(4),
for i = 1:N
for    k=1:Nk
subplot(3,2,i)
hold on
plot(T(1+(k-1)*PSL:k*PSL,1),X3D(1:PSL,i,k),'color',C{i},'linestyle','-');
hold on
line([k*PSL/Fs k*PSL/Fs],[-0.25 0.25],'Color',[.5 .5 .5],'LineStyle','--');
end
hold on
caption = sprintf('Beam B - Tip Displacement - Free Vibration Case #%d', i);
title(caption, 'FontSize', 10);
ylim([-0.25 0.25])
xlabel('Time (sec)')
ylabel('Amplitude (mm/mm)')
end

%% Separate Linear/Nonlinear
pksM3x=zeros(100,N,Nk); locsM3x=zeros(100,N,Nk);
for i=1:N %(play with peak ID parameters)
    for k=1:Nk
[pks3x,locs3x] = findpeaks(X3D(:,i,k),'MinPeakDistance',50,'MinPeakHeight',0.01);
Nlocs3x=length(locs3x);
pksM3x(1:Nlocs3x,i,k)=pks3x;
locsM3x(1:Nlocs3x,i,k)=locs3x;
NlocsM3x(1,i,k)=Nlocs3x;
    end
end

%Split the signal into a linear part and a nonlinear part
X3Dnl=X3D; X3Dli=X3D; ZZ=zeros(1,N,Nk);
for i=1:N
   for k=1:Nk
```

```
      for j=1:100-1
       if (locsM3x(j,i,k)>0) && (locsM3x(j+1,i,k)==0) % Find the last peak
ZZ(1,i,k) = locsM3x(j,i,k);
       end
      end
    X3Dli( 1:ZZ(1,i,k)   ,i,k)=0; %Nonlinear part
    X3Dnl( ZZ(1,i,k):end ,i,k)=0; %Linear part
   end
end

%% Envelopes construction
ESL=12000; %Envelope signal length total signal
EnvLI=zeros(N3D,N,Nk);    EnvNL=zeros(N3D,N,Nk);    EnvX=zeros(ESL,N,Nk);
logEnvLI=zeros(N3D,N,Nk); logEnvNL=zeros(N3D,N,Nk); logEnvX=zeros(ESL,N,Nk);
%The envelopes are determined using spline interpolation over local maxima
    separated by at least np samples.
 for i=1:N
   for k=1:Nk
%Construction of peak envelopes for the split up data.
EnvLI(:,i,k)=envelope(X3Dli(:,i,k),100,'peak'); %LI peak envelope
EnvNL(:,i,k)=envelope(X3Dnl(:,i,k), 25,'peak'); %NL peak envelope
%Set specific regions to zero:
EnvLI( 1:ZZ(1,i,k),i,k)=0;  EnvLI( N3D-200:end ,i,k)=0; EnvNL( ZZ(1,i,k)+1:end ,i,k
    )=0;
logEnvLI(:,i,k)=  log(EnvLI(:,i,k)); logEnvNL(:,i,k)=  log(EnvNL(:,i,k)); %
    Logarithmic envelopes
%Envelope construction for complete signal
EnvX(:,i,k)=envelope(X3D(1:ESL,i,k),25,'peak'); %Complete envelope for nonlinear
    analyses
logEnvX(:,i,k)=  log(EnvX(:,i,k)) ;             %Logarithmic envelope of complete
    signal
   end
 end

%%  Plot partitioned signal with envelopes
figure(5),
for i = 1:N
for    k=1:Nk
subplot(3,2,i)
hold on
plot(T(1+(k-1)*PSL:k*PSL,1),X3Dli(1:PSL,i,k),'color',C{i},'linestyle','-');
hold on
plot(T(1+(k-1)*PSL:k*PSL,1),X3Dnl(1:PSL,i,k),'color',C{9-i},'linestyle','-');
hold on
plot(T(1+(k-1)*PSL:k*PSL,1),EnvNL(1:PSL,i,k),'color',C{i},'linestyle','--');
hold on
plot(T(1+(k-1)*PSL:k*PSL,1),EnvLI(1:PSL,i,k),'color',C{9-i},'linestyle','--');
line([k*PSL/Fs k*PSL/Fs],[-0.25 0.25],'Color',[.5 .5 .5],'LineStyle','--');
line([0 25],[0.01 0.01],'Color','r','LineStyle','--');
end
```

```
hold on
caption = sprintf('Beam B - Tip Displacement - Free Vibration Case #%d', i);
title(caption, 'FontSize', 10);
ylim([0 0.1])
ylabel('Amplitude (mm/mm)')
end

%% Plot envelopes only
figure(6),
for i = 1:N
for    k=1:Nk
subplot(3,2,i)
hold on
plot(T(1+(k-1)*PSL:k*PSL,1),EnvNL(1:PSL,i,k),'color',C{i},'linestyle','-');
hold on
plot(T(1+(k-1)*PSL:k*PSL,1),EnvLI(1:PSL,i,k),'color',C{9-i},'linestyle','-');
line([k*PSL/Fs k*PSL/Fs],[-0.25 0.25],'Color',[.5 .5 .5],'LineStyle','--');
end
hold on
caption = sprintf('Beam B - Tip Displacement Envelope - Free Vibration Case #%d', i
    );
title(caption, 'FontSize', 10);
ylim([0 0.08])
end
%% Plot complete envelopes only
figure(7),
for i = 1:N
for    k=1:Nk
subplot(3,2,i)
hold on
plot(T(1+(k-1)*PSL:k*PSL,1),X3D(1:PSL,i,k),'color',[0.87 0.87 0.87],'linestyle','-'
    );
hold on
plot(T(1+(k-1)*PSL:k*PSL,1),EnvX(1:PSL,i,k),'color',C{7-i},'linestyle','-');
hold on
line([k*PSL/Fs k*PSL/Fs],[-0.25 0.25],'Color',[.5 .5 .5],'LineStyle','--');
end
hold on
caption = sprintf('Beam B - Tip Displacement Envelope - Free Vibration Case #%d', i
    );
title(caption, 'FontSize', 10);
ylim([0 0.08])
end
%% Polyfitting of logarithmic envelopes to obtain zeta1 (c1)
Lp=4500; %length for linear fitting
LinSlope=zeros(2,N,Nk); pvl=zeros(Lp,N,Nk);
for i=1:N
    for k=1:Nk
LinSlope(:,i,k) = polyfit( T(1:Lp,1),logEnvLI((ZZ(1,i,k)+1:ZZ(1,i,k)+Lp),i,k) ,1);
    %linear polyfit
```

```
pvl(:,i,k) = polyval(LinSlope(:,i,k),T(1:Lp,1));
    end
end
%% Plot envelopes in log scale (Linear part should give an approximate straight
    line)
figure(8)
for i = 1:N
for    k=1:Nk
subplot(3,2,i)
hold on
plot(T(1+(k-1)*PSL:k*PSL,1),logEnvNL(1:PSL,i,k),'color',C{i},'linestyle','-');
hold on
plot(T(1+(k-1)*PSL:k*PSL,1),logEnvLI(1:PSL,i,k),'color',C{9-i},'linestyle','-');
line([k*PSL/Fs k*PSL/Fs],[-10 0],'Color',[.5 .5 .5],'LineStyle','--');
hold on
plot(T(1+(k-1)*PSL+ZZ(1,i,k):ZZ(1,i,k)+k*PSL-(PSL-Lp),1),pvl(:,i,k),'color','g','
    linestyle','--');
end
hold on
caption = sprintf('Beam B - Tip Displacement Envelope - Free Vibration Case #%d', i
    );
title(caption, 'FontSize', 10);
xlim([0 25])
ylim([-8 -1])
ylabel('ln(X) (mm/mm)')
end

%% Plot slope values of linear envelopes
LinSlope(1,4,3)=LinSlope(1,4,2); LinSlope(1,5,3)=LinSlope(1,5,2);    %manual
    correction (single outlier points)
figure(9)
for i=1:N
    for k=1:Nk
hold on
plot(i,LinSlope(1,i,k),'marker','o','color',C{k})
    end
end
legend('1','2','3','4','5','6')

%% The linear damping coefficient is analyzed next.
% For the linear case the damping decrement abides a logarithmic relation.
% By plotting this in logarithmic scale, a straight line can be fitted to the
% signal peak envelope to estimate the damping coefficient. In the nonlinear
% case, however this is not possible.
avgli=zeros(1,N); ZetaLin=avgli; stdli=avgli; stdz1=avgli;
for i=1:N
avgli(i)=mean(LinSlope(1,i,:));
ZetaLin(i)= -avgli(i)/(2*pi*Fvect(i));
stdli(i)= std(LinSlope(1,i,:));
stdz1(i)= std(LinSlope(1,i,:)/(2*pi*Fvect(i)));
```

```
413 end
414
415 figure(10) %plot the linear damping ratios and standard deviations
416 subplot(1,3,1)
417 for i=1:N
418     hold on
419 plot(Nvect(i),ZetaLin(i),'marker','o','linestyle','--','color',C{i})
420 end
421 xlim([0 8])
422 xlabel('Test Number')
423 ylabel('\zeta_1 (%)')
424 subplot(1,3,2)
425 for i=[2 3 4 5]
426     hold on
427 errorbar(Nvect(i),ZetaLin(i)*100,stdz1(i)*100,'marker','o','linestyle','--','color'
    ,C{i},'linewidth',1.5)
428 end
429 xlim([0 8])
430 xlabel('Test Number')
431 ylabel('\zeta_1 (%)')
432 subplot(1,3,3)
433 plot(Nvect,stdz1,'marker','x','linestyle','none')
434 line([0 8],[0.008/100 0.008/100],'color',C{1},'LineStyle','--');
435 xlim([0 8])
436 xlabel('Test Number')
437 ylabel('Standard deviation of \zeta_1 values')
438
439 figure(11)
440 for i=[2 3 4 5]
441     hold on
442 errorbar(Nvect(i)*35000-35000,ZetaLin(i)*100,stdz1(i)*100,'marker','o','linestyle',
    '--','color',C{i},'linewidth',1.5)
443 end
444 xlim([-2000 180000])
445 ylim([0.2 0.35])
446 xlabel('Cycles')
447 ylabel('\zeta_1 (%)')
448
449 %% FFT's for frequency overview and to check for presence of amplifier noise
450 for a=1
451 Lf = N3D;               % Length of signal
452 t = Ts;                 % Time vector
453 f = Fs*(0:(Lf/2))/Lf;   % Frequency axis
454 FFN=zeros(N3D,N,Nk); FFL=FFN; FFNP2=FFN; FFLP2=FFN;
455 FFNP1=zeros(N3D/2+1,N,Nk); FFLP1=FFNP1;
456 for i=1:N
457 for k=1:Nk
458 FFN(:,i,k) = fft(X3Dnl(:,i,k));
459 FFNP2(:,i,k) = abs(FFN(:,i,k)/Lf);
460 FFNP1(:,i,k) = FFNP2(1:Lf/2+1,i,k);
```

```
FFNP1(2:end-1,i,k) = 2*FFNP1(2:end-1,i,k);
FFL(:,i,k) = fft(X3Dli(:,i,k));
FFLP2(:,i,k) = abs(FFL(:,i,k)/Lf);
FFLP1(:,i,k) = FFLP2(1:Lf/2+1,i,k);
FFLP1(2:end-1,i,k) = 2*FFLP1(2:end-1,i,k);
end
end

figure(20) % plot linear and nonlinear fft's
for i = 1:N
    for    k=1:Nk
subplot(3,2,i)
caption = sprintf('FFT - Linear and Nonlinear #%d', i);
title(caption, 'FontSize', 5);
plot( f/Fnat*Fnat , FFNP1(:,i,k))%,'marker','x')%,'markersize',6,'linestyle','none
    ')
hold on
plot( f/Fnat*Fnat , FFLP1(:,i,k) ,'linestyle','-')
hold on
caption = sprintf('Beam B - FFT - Linear Free Vibe Case #%d', i);
title(caption, 'FontSize', 10);
xlim([0.8*Fnat 1.1*Fnat])
set(gca, 'YScale', 'log')
title('Single-Sided Amplitude Spectrum of X(t)')
xlabel('Frequency (\omega/\omega_n)')
    end
end
end

%% Zero-crossing instantaneous frequency analysis
%Algorithm to find two time points between each downward zero crossing
SLF=N3D-2000;
ZeroCros=zeros(SLF,N,Nk);
for i=1:N
  for j=1:Nk
    for k=1:SLF-1
      if (X3D(k,i,j)>0) && (X3D(k+1,i,j)<0)
%downward-crossings interpolation to estimate exact time point of zero-crossing:
ZeroCros(k,i,j) = X3D(k,i,j)/(X3D(k,i,j)-X3D(k+1,i,j))*(T(k+1,1)-T(k,1))+T(k,1);
      end
    end
  end
end

% Run peak alg. over ZeroCros to asses nonzero data and find the indices of
    crossings in the main signal
PMzf=zeros(700,N,Nk); LMzf=zeros(700,N,Nk); NLMzf=zeros(1,N,Nk);
for i=1:N
    for j=1:Nk
[Pzf,Lzf] = findpeaks((ZeroCros(:,i,j)),'MinPeakDistance',5,'MinPeakHeight'
```

```
    ,0.00001);
NLzf=length(Lzf);
PMzf(1:NLzf,i,j)=Pzf; %creates peak matrix
LMzf(1:NLzf,i,j)=Lzf; %creates peak locations matrix
NLMzf(1,i,j)=NLzf;    %the amount of peaks per case
    end
end

NZ1=1; NZ2=180; %Data range for zero-cross analysis
InstFreq=zeros(NZ2,N,Nk);
%Obtain instantaneous frequency from distances between consecutive crossings
for i=1:N
  for j=1:Nk
    for k=NZ1:NZ2
    InstFreq(k-NZ1+1,i,j)=1/(PMzf(k+1,i,j)-PMzf(k,i,j));
      %make infinities and absurdly large frequencies zero
      if (InstFreq(k,i,j)>100)
      InstFreq(k,i,j) = 0;
      end
    end
% Moving average filter (smooth function)
% set span of moving average (for span of five, first two points unfiltered)
InstFreq(1:NZ2,i,j) = smooth(InstFreq(1:NZ2,i,j),5);
  end
end
clear ZeroCros

%% Plot the instantaneous frequencies for each damage case
TFaxis=zeros(NZ2,N,Nk); % Time axis
figure(30)
for i=1:N
for j=1:Nk
TFaxis(1:NZ2,i,j)=T(LMzf(1:NZ2,i,j),1);
subplot(3,2,i)
hold on
plot(TFaxis(:,i,j),InstFreq(:,i,j),'color',C{j},'marker','o');
end
end

%% Plot the amplitude envelopes for each damage case
figure(31)
for i=1:N
for j=1:Nk
subplot(3,2,i)
hold on
plot(T(1:ESL,1),EnvX(:,i,j),'color',C{j},'marker','o');
end
end

%% Plot backbone curves of pristine case only
```

```
figure(40)
for i=1
for j=1:Nk
hold on
plot(InstFreq(5:158,i,j),CL*EnvX(LMzf(5:158,i,j),i,j),'color',C{j},'marker','o','
    linestyle','none');
end
end
title('Beam B - Pristine Case - Backbone curve')
xlabel('Frequency (Hz)')
ylabel('Tip Amplitude (mm)')

%% Plot the main backcurves for all cases
figure(41)
for a=5:140
 for j=1:Nk-3
  for i=1:N
    if (EnvX(LMzf(a,i,j),i,j)>0.003) % Avoids plotting very low amplitude values
    for cleaner graph
hold on
plot(InstFreq(a,i,j)/Fnat,EnvX(LMzf(a,i,j),i,j),'color',C{i},'marker','o','
    linestyle','none');
    end
  end
 end
end
for i=1:N
hold on
line([Fvect(i)/Fnat Fvect(i)/Fnat],[0 CL*0.12],'Color',C{i}','LineStyle','--','
    linewidth',2);
end
xlim([49/Fnat 59.5/Fnat])
ylim([0 0.14])
grid on
set(gca,'box','on')
legend('Pristine','Fatigue: N=35000','Fatigue: N=70000','Fatigue: N=105000'...
    ,'Fatigue: N=140000','Fatigue: N=175000','Location','NorthWest')
xlabel('Frequency (\omega/\omega_n)')
ylabel('Amplitude (X/L)')
title('Backbone Curves - Beam B')

Zrange=[180 180 180 180 180 180]; %custom range for each damage case
figure(42) % Plot Backbones with longer signal length and custom ranges
for j=1:Nk
 for i=1:N
    hold on
plot(InstFreq(5:Zrange(i),i,j),EnvX(LMzf(5:Zrange(i),i,j),i,j),'color',C{j},'marker
    ','o','linestyle','none');
hold on
line([Fvect(i) Fvect(i)],[0 CL*0.18],'Color',C{i}','LineStyle','--');
```

```
603 end
604 end
605 xlim([52 59.5])
606 ylim([0 0.14])
607 grid on
608 legend('Pristine','Fatigue: N=35000','Fatigue: N=70000','Fatigue: N=105000','
    Fatigue: N=140000',...
609     'Fatigue: N=175000','Fatigue: N=210000','Fatigue: N=245000','Location','
    NorthWest')
610 xlabel('Frequency (\omega/\omega_n)')
611 ylabel('Amplitude (X/L)')
612 title('Backbone Curves - Beam B')
613
614 %% Plot linear region of backbone curves with Gaussian Filter (Heavy Filtering)
615 Zgauss=zeros(size(InstFreq)); % Apply Gaussian filter to make linear region
    presentable
616 for i=1:N
617     for j=1:Nk
618 Zgauss(:,i,j) = smoothdata(InstFreq(:,i,j),'gaussian',30);
619     end
620 end
621
622 %Plot linear region backbone
623 figure(43)
624 for j=1:Nk-3
625  for i=1:N
626 hold on
627 plot(Zgauss(5:Zrange(i),i,j)/Fnat,EnvX(LMzf(5:Zrange(i),i,j),i,j),'color',C{i},'
    marker','o','linestyle','none');
628  end
629 end
630 for i=1:N
631   hold on
632 line([Fvect(i)/Fnat Fvect(i)/Fnat],[0 0.025],'Color',C{i}','LineStyle','--','
    linewidth',2);
633 end
634 hold on
635 line([0.7 1.3],[0.01 0.01],'Color',[0.4 0.4 0.4],'LineStyle','--','linewidth',2);
636 xlim([0.75 1.01])
637 ylim([0 0.012])
638 set(gca,'box','on')
639 legend('Pristine','Fatigue: N=35000','Fatigue: N=70000','Fatigue: N=105000','
    Fatigue: N=140000',...
640     'Fatigue: N=175000','Location','NorthWest')
641 xlabel('Frequency (\omega/\omega_n)')
642 ylabel('Amplitude (X/L)')
643 title('Backbone Curves - Linear Region - Beam B (Guassian Filter)')
644
645 %% Effective damping ratio calculation.
646 NZ2=150; NZend=180; zetaEFF=zeros(NZend-10,N,Nk); zetaLondono=zeros(NZend-10,N,Nk);
```

```
Nzeta=5;
for i=1:N
   for k=1:Nk
      for j=Nzeta+1:NZend-Nzeta
%Piecewise linear interpretation;
zetaEFF(j,i,k) =(logEnvX(LMzf(j-Nzeta,i,k),i,k)-logEnvX(LMzf(j+Nzeta,i,k),i,k))...
    /(2*pi*InstFreq(j,i,k)*(T(LMzf(j+Nzeta,i,k),1)-(T(LMzf(j-Nzeta,i,k),1))))  ;
%Londono's method (2015);
zetaLondono(j,i,k) =(logEnvX(LMzf(1,i,k),i,k)-logEnvX(LMzf(j,i,k),i,k))...
    /(2*pi*InstFreq(j,i,k)*(T(LMzf(j,i,k),1)-(T(LMzf(1,i,k),1))))  ;
      end
   end
end

%% Create Arrays to obtain k3 and c2 through Curve Fitting Toolbox
M2=21300; % Nonlinear inertial coeff from analytical model (Meff=m1+1/2*m2*X^2)
NDcf=30;  % NDcf = number of data points for curve fitting
NJcf=4;   % NJcf = number of vibrations for curve fitting

%INITIALIZE ARRAYS FOR CURVE FITTING SESSION
CFK=zeros(NDcf*NJcf,N); CFX=CFK;  CFZ=CFK; Meff=CFK;
ck1=zeros(NDcf*NJcf,1); ck2=ck1; ck3=ck1; ck4=ck1; ck5=ck1; ck6=ck1; %effective
    stiffness
cx1=zeros(NDcf*NJcf,1); cx2=cx1; cx3=cx1; cx4=cx1; cx5=ck1; cx6=ck1; %amplitude
    values
cz1=zeros(NDcf*NJcf,1); cz2=cz1; cz3=cz1; cz4=cz1; cz5=cz1; cz6=cz1; %effective
    damping
OmegaSqr=zeros(N); OmegaSqr=(2*pi*Fvect).^2;
  for i=1:N
    for j=1:NJcf
% Effective Mass
Meff(1+(j-1)*NDcf:NDcf+(j-1)*NDcf,i)=1+M2*0.5*(CL/1000/15*EnvX(LMzf(5:5+NDcf-1,i,j)
    ,i,j)).^2;
% Keff=omega(X)^2*Meff
CFK(1+(j-1)*NDcf:NDcf+(j-1)*NDcf,i)=(2*pi.*InstFreq(5:5+NDcf-1,i,j)).^2;
% Amplitude values
CFX(1+(j-1)*NDcf:NDcf+(j-1)*NDcf,i)=CL/1000*EnvX(LMzf(5:5+NDcf-1,i,j),i,j);
% Construction of arrays to obtain zeta2:
% zetaEFF=zeta1+const*omega_n(X)*zeta2*X  --> (zetaEFF-zeta1)/omega_n(X)=constants*
    zeta2*X
CFZ(1+(j-1)*NDcf:NDcf+(j-1)*NDcf,i)=(zetaEFF(5:5+NDcf-1,i,j)-ZetaLin(i))./(2*pi.*
    InstFreq(5:5+NDcf-1,i,j));
    end
CFK(:,i)=CFK(:,i).*Meff(:,i)-OmegaSqr(i);
  end
ck1(:,1)=CFK(:,1); ck2(:,1)=CFK(:,2); ck3(:,1)=CFK(:,3); ck4(:,1)=CFK(:,4); ck5
    (:,1)=CFK(:,5); ck6(:,1)=CFK(:,6);
cx1(:,1)=CFX(:,1); cx2(:,1)=CFX(:,2); cx3(:,1)=CFX(:,3); cx4(:,1)=CFX(:,4); cx5
    (:,1)=CFX(:,5); cx6(:,1)=CFX(:,6);
cz1(:,1)=CFZ(:,1); cz2(:,1)=CFZ(:,2); cz3(:,1)=CFZ(:,3); cz4(:,1)=CFZ(:,4); cz5
```

```
    (:,1)=CFZ(:,5); cz6(:,1)=CFZ(:,6);
end

%% Plot the damping skeletons
figure(51)
for j=1:3
    for i=2:5
hold on
plot(100*zetaEFF(8:80,i,j),EnvX(LMzf(8:80,i,j),i,j),'color',C{i},'marker','o','
    linestyle','none');
    end
end
for i=2:5
    hold on
    line([ZetaLin(i)*100 100*ZetaLin(i)],[0 0.15],'Color',C{i}','LineStyle','--','
    linewidth',2);
end
xlim([0.1 1.2])
ylim([0 0.12])
legend('Fatigue: N=35000','Fatigue: N=70000','Fatigue: N=105000','Fatigue: N=140000
    ','Location','NorthWest')
xlabel('Effective Damping Ratio, \zeta_{eff} (%)')
ylabel('Amplitude (X/L)')
title('Damping Skeletons - Beam B')
%%
figure(511)
for j=1:3
    for i=1:N
hold on
plot(100*zetaEFF(8:100,i,j),EnvX(LMzf(8:100,i,j),i,j),'color',C{i},'marker','o','
    linestyle','none');
    end
end
xlim([0.1 1.2])
ylim([0 0.12])
legend('Pristine','Fatigue: N=70000','Fatigue: N=175000','Location','NorthWest')
xlabel('Effective Damping Ratio, \zeta_{eff} (%)')
ylabel('Amplitude (X/L)')
title('Damping Skeletons - Beam B - All')
%% Damp skeleton Example Visualization (Pristine case)
figure(52)
for j=1:Nk
hold on
plot(100*zetaEFF(8:100,1,j),CL*EnvX(LMzf(8:100,1,j),1,j),'color',C{j},'marker','o',
    'linestyle','none');
end
xlabel('Effective Damping Ratio, \zeta_{eff} (%)')
ylabel('Tip Amplitude (mm)')
title('Beam B - Pristine Case - Damping Skeletons')
```

APPENDIX C

Repeatability of the Backbone Curves

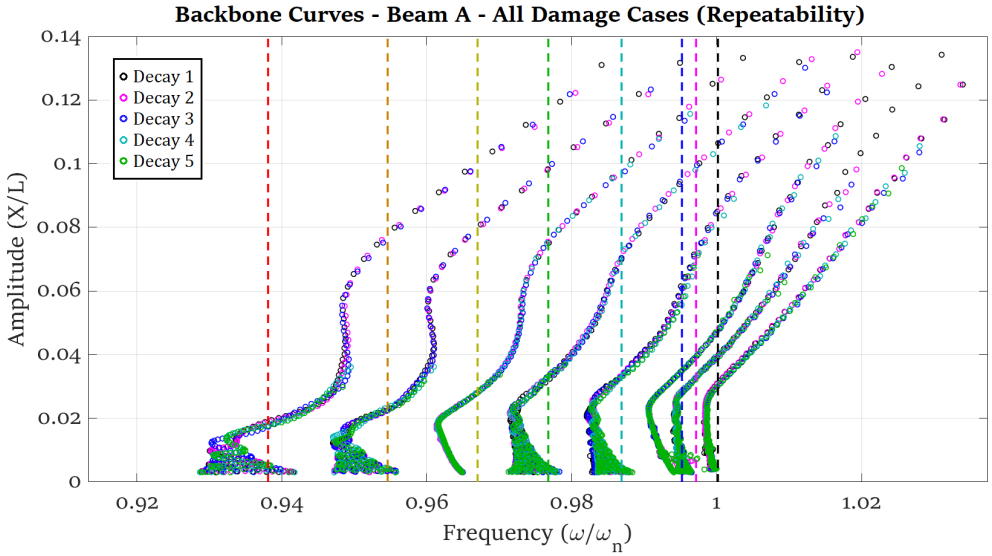

Figure C.1: Backbone curves for Beam A

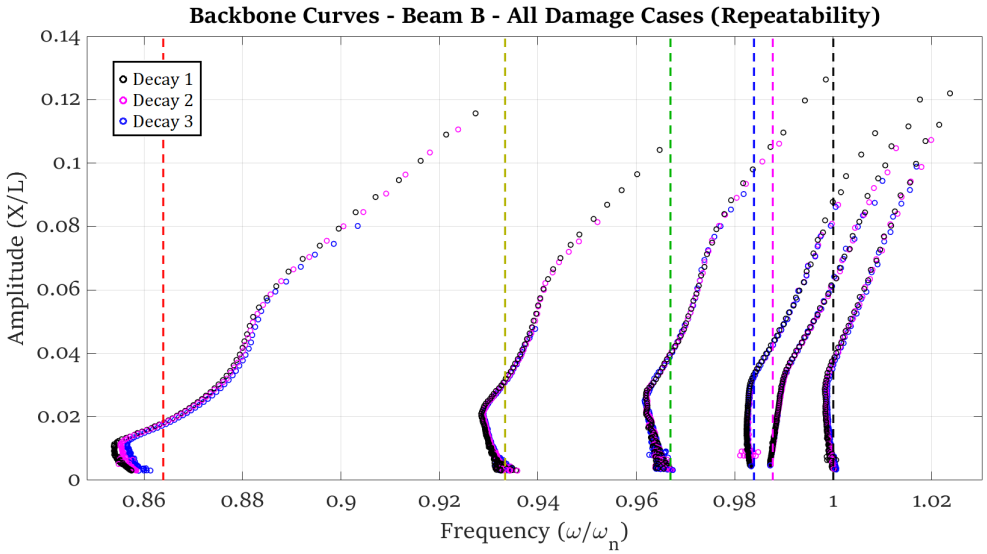

Figure C.2: Backbone curves for Beam B

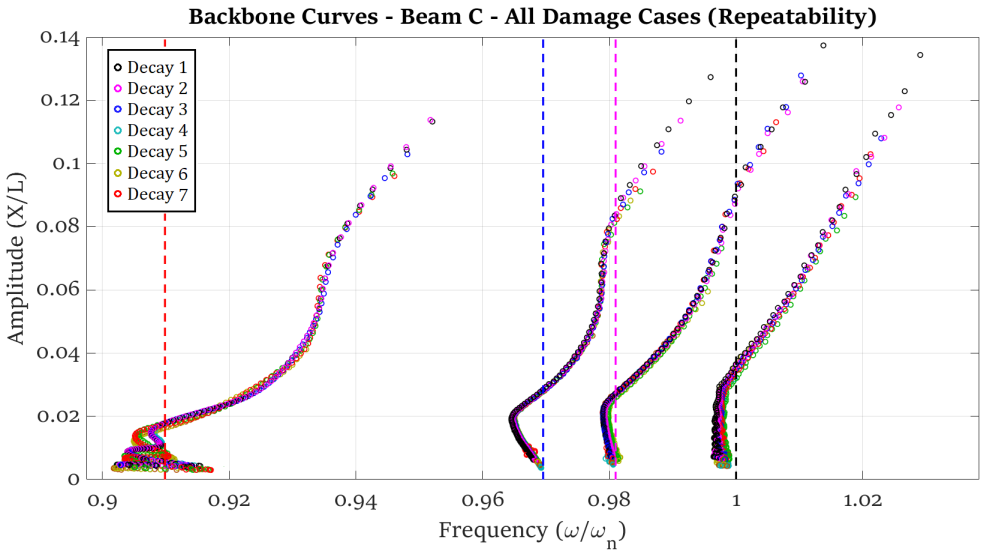

Figure C.3: Backbone curves for Beam C

APPENDIX D

Supplementary Information

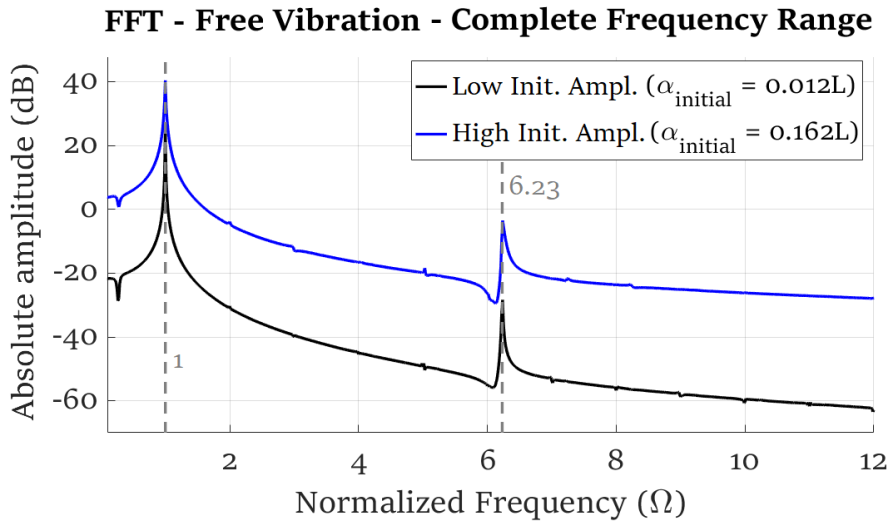

Figure D.1: FFT for the whole range of frequencies (Pristine case). Both FFTs were taken for the full decay duration. Primary peak present at the first bending mode and seconday peak present at the second bending mode.

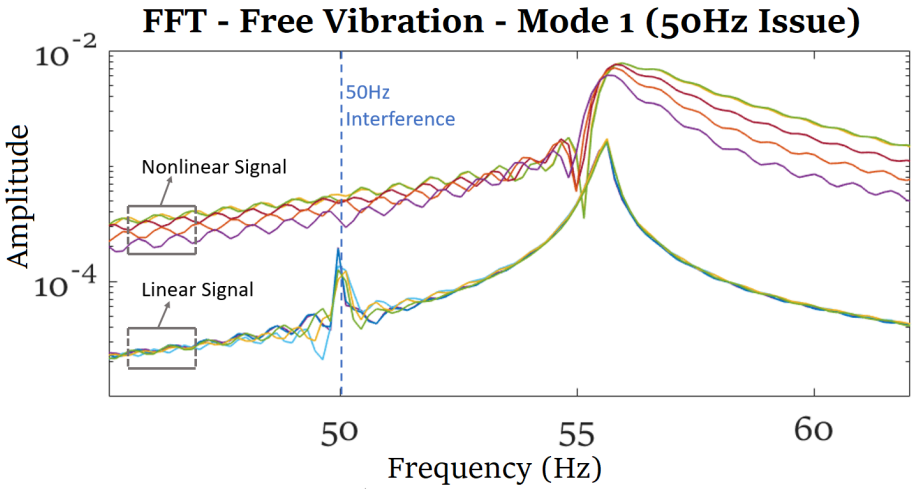

Figure D.2: FFT zoomed into Mode 1 showing the interference coming from the amplifier. This was not an issue for the nonlinear signal. The issue was only present in certain cases where the amplifier was switched on. This specific result is for free decays of Beam A fatigued at 105000 cycles.

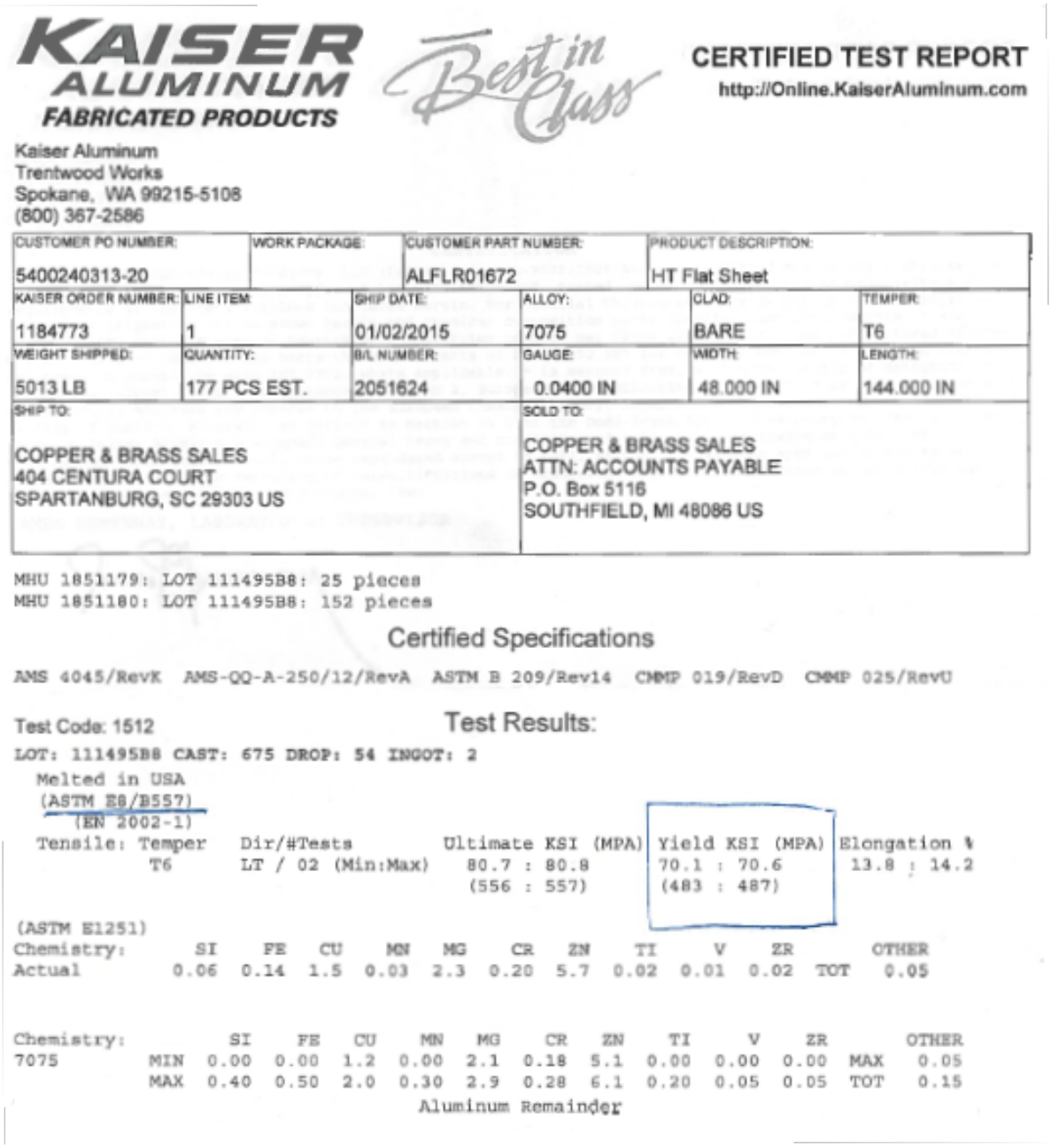

KAISER ALUMINUM
FABRICATED PRODUCTS

Best in Class

CERTIFIED TEST REPORT
http://Online.KaiserAluminum.com

Kaiser Aluminum
Trentwood Works
Spokane, WA 99215-5108
(800) 367-2586

CUSTOMER PO NUMBER:	WORK PACKAGE:	CUSTOMER PART NUMBER:	PRODUCT DESCRIPTION:		
5400240313-20		ALFLR01672	HT Flat Sheet		
KAISER ORDER NUMBER:	LINE ITEM:	SHIP DATE:	ALLOY:	CLAD:	TEMPER:
1184773	1	01/02/2015	7075	BARE	T6
WEIGHT SHIPPED:	QUANTITY:	B/L NUMBER:	GAUGE:	WIDTH:	LENGTH:
5013 LB	177 PCS EST.	2051624	0.0400 IN	48.000 IN	144.000 IN

SHIP TO:
COPPER & BRASS SALES
404 CENTURA COURT
SPARTANBURG, SC 29303 US

SOLD TO:
COPPER & BRASS SALES
ATTN: ACCOUNTS PAYABLE
P.O. Box 5116
SOUTHFIELD, MI 48086 US

MHU 1851179: LOT 111495B8: 25 pieces
MHU 1851180: LOT 111495B8: 152 pieces

Certified Specifications

AMS 4045/RevK AMS-QQ-A-250/12/RevA ASTM B 209/Rev14 CMMP 019/RevD CMMP 025/RevU

Test Code: 1512

Test Results:

LOT: 111495B8 CAST: 675 DROP: 54 INGOT: 2

Melted in USA
(ASTM E8/B557)
(EN 2002-1)

Tensile:	Temper	Dir/#Tests	Ultimate KSI (MPA)	Yield KSI (MPA)	Elongation %
	T6	LT / 02 (Min:Max)	80.7 : 80.8 (556 : 557)	70.1 : 70.6 (483 : 487)	13.8 : 14.2

(ASTM E1251)

Chemistry:	SI	FE	CU	MN	MG	CR	ZN	TI	V	ZR		OTHER
Actual	0.06	0.14	1.5	0.03	2.3	0.20	5.7	0.02	0.01	0.02	TOT	0.05

Chemistry:		SI	FE	CU	MN	MG	CR	ZN	TI	V	ZR		OTHER
7075	MIN	0.00	0.00	1.2	0.00	2.1	0.18	5.1	0.00	0.00	0.00	MAX	0.05
	MAX	0.40	0.50	2.0	0.30	2.9	0.28	6.1	0.20	0.05	0.05	TOT	0.15

Aluminum Remainder

Figure D.3: Material specifications from manufacturer